Imperial College London
Department of Earth Science and Engineering

Pore-scale Modelling of Multiphase Flow: The Impact of Geometry and Wettability

Luke M. Giudici

Supervisors: Dr. Branko Bijeljic and Prof. Martin J. Blunt

Submitted in fulfilment of the requirements
for the degree of Doctor of Philosophy at
Imperial College London, September 2023

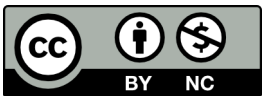

I hereby declare that this thesis and the work reported herein was composed by and originated entirely from me. Information derived from the published and unpublished work of others has been acknowledged in the text and references are given in the list of sources.

Luke M. Giudici (2023)

Abstract

Traditionally, wettability has been considered key in predicting the nature of two-phase flow through porous media. In this thesis, the local geometry is shown to also have a significant impact, and the interaction between geometry and wettability is studied using a variety of modelling approaches.

First, quasi 2D approximations of interfacial curvature, present in current pore-network models, are extended to three dimensions. The new expressions for threshold capillary pressure are calibrated using high-resolution direct numerical simulations. The effects of pore-space expansion and sagittal interface curvature on displacement are quantified and shown to be a key step in improving network model accuracy. The extended network model predictions for relative permeability and capillary pressure agree well with experiments for a water-wet Bentheimer sandstone, demonstrating that the inclusion of 3D interfacial curvature leads to more accurate predictions.

Next, the extended network model predictions are compared to lattice-Boltzmann simulations for two synthetic geometries with varying wettabilities. Macroscopic capillary pressures between the two models, and with experiments, agree at intermediate saturations but differ at the end-points. Direct methods at readily accessible resolutions fail to capture layer flow, leading to abnormally large initial wetting and residual non-wetting saturations. Pore-by-pore analysis indicates that the absence of layer flow limits displacement to invasion-percolation in mixed-wet systems. Network models, which can easily capture layer effects, provide predictions closer to experimental observations. However, discrepancies persist for mixed-wet systems due to a limited understanding of mixed-wet displacement.

Finally, the stability and displacement of interfaces in mixed-wet media is addressed. Theoretical and numerical considerations reveal that interface stability depends on both the local geometry and wettability. An explanation is provided for the observed low capillary pressure displacement in mixed-wet systems, along with an empirical expression predicting threshold displacement pressure in a 3D geometry with realistic pore-space expansion.

Acknowledgements

First, I must express my deepest gratitude to Dr. Branko Bijeljic and Prof. Martin Blunt for their unwavering support, insights, and advice. A PhD student could not wish for better supervisors. It has been a pleasure and a privilege to be a part of their research group for the last four years, and I will carry the knowledge they have imparted to me throughout my career.

I would also like to extend my appreciation to the Engineering and Physical Sciences Research Council for providing funding throughout the project, and to Prof. Peter King and Prof. Vahid Niasar for agreeing to be my PhD examiners.

Next, a special thank you must be given to Dr. Ali Raeini. I will be forever grateful for your extraordinary patience and kindness throughout the PhD. This work would not have been possible without the technical and personal skills you shared with me, along with your scientific mentorship. Beyond academic discussions, our funny political chats were a highlight of my first three years, and I feel honoured to have you as a friend.

Another friend and colleague who cannot go unmentioned is Dr. Sajjad Foroughi. It is a great regret that we could not interact until the second half of my PhD. I always looked forward to chatting at your desk, and I hope we can continue our friendship into the future.

The Digital Rocks Physics team at TotalEnergies, specifically Dr. Mohamed Regaieg and Dr. Richard Rivenq, deserve thanks for their support and advice.

No acknowledgements section would be complete without thanking the incredible group of friends who have kept me sane throughout the PhD. Particular thanks go to Dr. Geraldine Regnier, whose lunch chats provided grounding in difficult times.

Thank you, Rita, for your unwavering support and for being by my side through everything.

Last, but certainly not least, I come to my family. Words cannot express the credit that my family, and particularly my mother, deserve for any success that I may achieve.

List of Publications

Chapter 3: Giudici, L.M., Raeini, A.Q., Blunt, M.J., Bijeljic, B. (2023). Representation of fully three-dimensional interfacial curvature in pore-network models, *Water Resour. Res.*, 59, e2022WR033983.

Chapter 4: Giudici, L.M., Raeini, A.Q., Akai, T., Blunt, M.J., Bijeljic, B. (2023). Pore-scale modeling of two-phase flow: A comparison of the generalized network model to direct numerical simulation, *Phys. Rev. E.*, 107(3), 03517, DOI: 10.1103/PhysRevE.107.035107.

Chapter 5: Giudici, L.M., Foroughi, S., Blunt, M.J., Bijeljic, B. (2023). Interface Stability and Displacement in Mixed-Wet Media, *Phys. Rev. Lett.*, (in prep)

Additional Publications

Raeini, A.Q., **Giudici, L.M.**, Blunt, M.J., Bijeljic, B. (2022). Generalized network modelling of two-phase flow in a water-wet and mixed-wet reservoir sandstone: uncertainty and validation with experimental data, *Adv. Water Res.*, 164, 104194, DOI: j.advwatres.2022.104194.

CONTENTS

LIST OF TABLES

LIST OF FIGURES

NOMENCLATURE

Planar Definitions

Axial Plane The plane parallel to the throat surface and normal to the flow direction

Coronal Planes The planes defining the boundaries of each corner in the generalized network model

Sagittal Planes The planes bisecting each corner

Symbols

α	Angle from a reference origin of a point on the three-phase contact loop
β	Expansion angle of the solid surface relative to the throat centre to pore centre line
γ	Corner half angle
κ	Total curvature
κ_a	Curvature in the axial plane
κ_s	Curvature in the sagittal plane
μ	Dynamic viscosity
θ	Contact angle
a	The first coefficient of pore-space expansion
b	The second coefficient of pore-space expansion
c	The coefficient of layer sagittal curvature in a throat
C_a	Capillary number
d	The coefficient of layer sagittal curvature in a pore
e_n	Coefficients used in the empirical prediction of displacement capillary pressure in a mixed-wet system
k_r	Relative permeability
L	Three-phase contact length
m_n	Coefficients used in the empirical prediction of displacement capillary pressure in a mixed-wet system
r	Radius of curvature or inscribed radius
S	Entropy, saturation

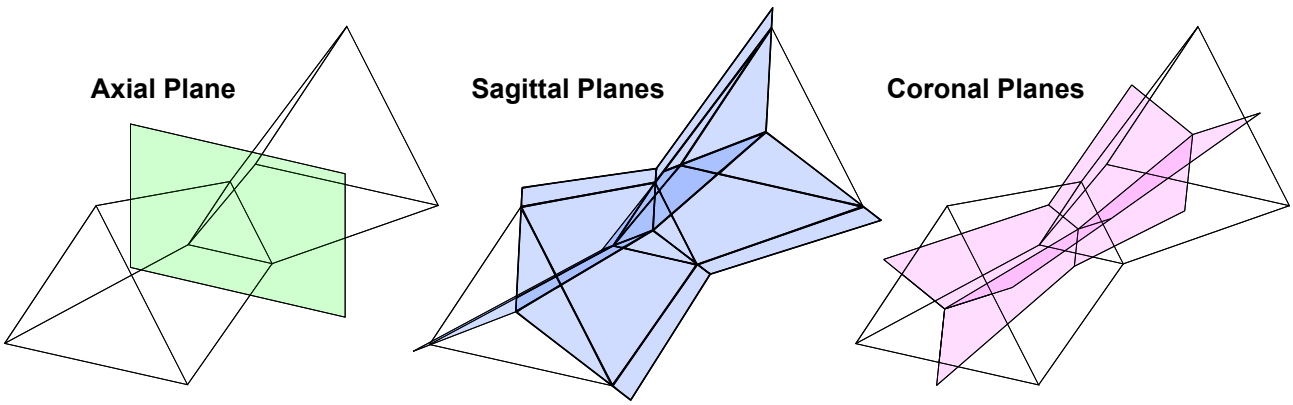

CHAPTER 1

INTRODUCTION, THEORETICAL BACKGROUND AND LITERATURE REVIEW

1.1 Overview

Multiple fluid phases flowing simultaneously through a permeable medium is at the heart of many important applications. For example, safely storing CO_2 in the Earth's subsurface requires a comprehensive assessment of reservoir fluid behaviour (e.g, *Boot-Handford et al.*, 2014; *Krevor et al.*, 2015; *Alhosani et al.*, 2020a). The performance of polymer-electrolyte membrane fuel cells depends, in part, on the ease with which reactant gases and water byproduct can simultaneously flow through the permeable layers within the cell (e.g, *Mukherjee et al.*, 2011; *Zhang et al.*, 2021; *Okonkwo and Otor*, 2021). Even the spread of a contagion within a human population can be linked — a surgical mask is simply a permeable medium allowing one to breathe whilst limiting exposure to airborne pathogens (*Mittal et al.*, 2020).

A natural objective for modelling such phenomena is to achieve predictive capability. Given a porous medium, it is valuable to know exactly how the fluids will displace and arrange within it, and the implications that this has for the application of interest. For instance, if significant effort is spent to inject CO_2 beneath the surface, will it actually stay there? Or, for media which can be engineered, how can a medium be designed for optimal performance? Answering these questions is a complex task which attracts substantial industrial and academic interest. In general, a description of the displacement of fluids in a medium will depend on scale – in the example of geologic media, capillary forces will control the movement of fluids at the micron-scale, while the geological structure as a whole will determine preferential flow paths at the kilometre scale. This thesis will address the former micron-scale, commonly referred to as the pore-scale, as it is this scale which is ubiquitous across all applications.

Conventionally, laboratory experiments were performed to gain an understanding of pore-scale flow (*Keelan*, 1972). These experiments are costly, time-consuming and, until recently, did not provide a clear picture of pore-scale processes; only macroscopic (core-scale) property measurements were obtained. Recent decades have seen the rapid development of digital rock physics (DRP) (*Blunt et al.*, 2013; *Wildenschild and Sheppard*, 2013), which uses micro-CT scanners, intricate experiments and high-quality image processing to visualise displacements within the pore space. This has revolutionised understanding of pore-scale flow as it is now possible to visually observe, down to a time resolution of seconds (*Berg et al.*, 2013), exactly what is happening in the pore space. However, despite improvements, the experiments themselves are still arduous and do not provide complete understanding of the most important parameters.

Another approach, which does allow a full exploration of the parameter space, is to numerically model fluid flow in the pore space. Many methods have been developed for this purpose, but common to all approaches is that they rely on an accurate characterisation of the pore-space geometry and the wettability – the affinity of a solid surface to be in contact with a particular fluid phase. Here lies the true benefit of DRP: pore-scale imaging can provide unprecedented characterisation of the pore space to be used in a physically-based numerical model. In return, the model will provide deeper understanding of pore-scale flow, the ability to rapidly predict a wide range of systems and inspiration for future experimental work. This symbiotic relationship is fast becoming an established and fruitful workflow (e.g, *Regaieg et al.*, 2023), but there is still a wealth of opportunity to improve the physical accuracy of pore-scale numerical models and understanding of fluid-fluid displacement in complex wetting states.

Given that high quality model inputs exist, the next task is to produce a model which adequately uses these inputs. One approach would simply be to simulate flow directly on the experimentally acquired images. This is indeed possible, but even with modern resources it is enormously demanding. Another approach is to pose a model which includes only the minimum necessary detail needed to be predictive. This approach is known as pore-network modelling (*Fatt*, 1956). Fast, simple and highly scalable, pore-network modelling offers an attractive alternative to more computationally intensive approaches. However, despite

recent advances in pore-scale imaging, network models have remained largely unchanged since showing early promise near the turn of the century (*Øren et al.*, 1998; *Valvatne and Blunt*, 2004). Additionally, their simplified nature raises uncertainty as to what exactly is the minimum detail needed. As this thesis will show, current network models do not adequately use the enhanced characterisation of geometry and wettability revealed by new experimental procedures.

In this thesis, an existing state-of-the-art network model (*Raeini et al.*, 2017, 2018) will be further developed to explicitly account for geometry and wettability, with an emphasis on extending two-dimensional conceptualisations to three dimensions and quantifying the subsequent improvements in predictive capability. A variety of direct numerical approaches are used to ensure that these developments are accurate and to provide enhanced physical understanding of wettability and geometry-dependent phenomena. The overall outcome of the thesis is a network model which has an unprecedented representation of interfacial curvature, fundamental improvements to the current understanding of pore-scale displacement by considering both wettability and pore-space geometry, and clear directions for future research. In the remainder of this chapter, the essential theory needed to achieve these objectives will be presented, in addition to a review of relevant previous studies and the central research opportunities.

1.2 Theoretical Background

This thesis considers two fluids, which, unless stated otherwise, are termed phases 1 and 2. Phase 1 represents the denser phase, typically water. In this section, the pore-scale physics of immiscible two-phase flow necessary to create a self-contained thesis are presented.

1.2.1 Fundamental Pore-scale Physics

Interfacial Curvature

Before introducing fluid interfaces, the concept of surface curvature must be established. Consider a differentiable surface in a three-dimensional space, as illustrated in Fig. 1.1. At

an arbitrary point on the surface, it is possible to define a unit normal vector, $\hat{\mathbf{n}}$, and a corresponding normal plane which contains the normal vector and a unit tangent vector, $\hat{\mathbf{t}}$, to the surface. The intersection of the normal plane with the surface is a smooth curve; the normal curvature is defined as the inverse of the radius of the circle which fits the curve at the chosen point. Different normal curvatures may arise if the orientation of the normal plane is changed. The maximum and minimum normal curvatures among all possible normal planes are termed the principal curvatures, with radii denoted by r_1 and r_2, and their principal directions, $\hat{\mathbf{t}}_1$ and $\hat{\mathbf{t}}_2$, are always orthogonal.

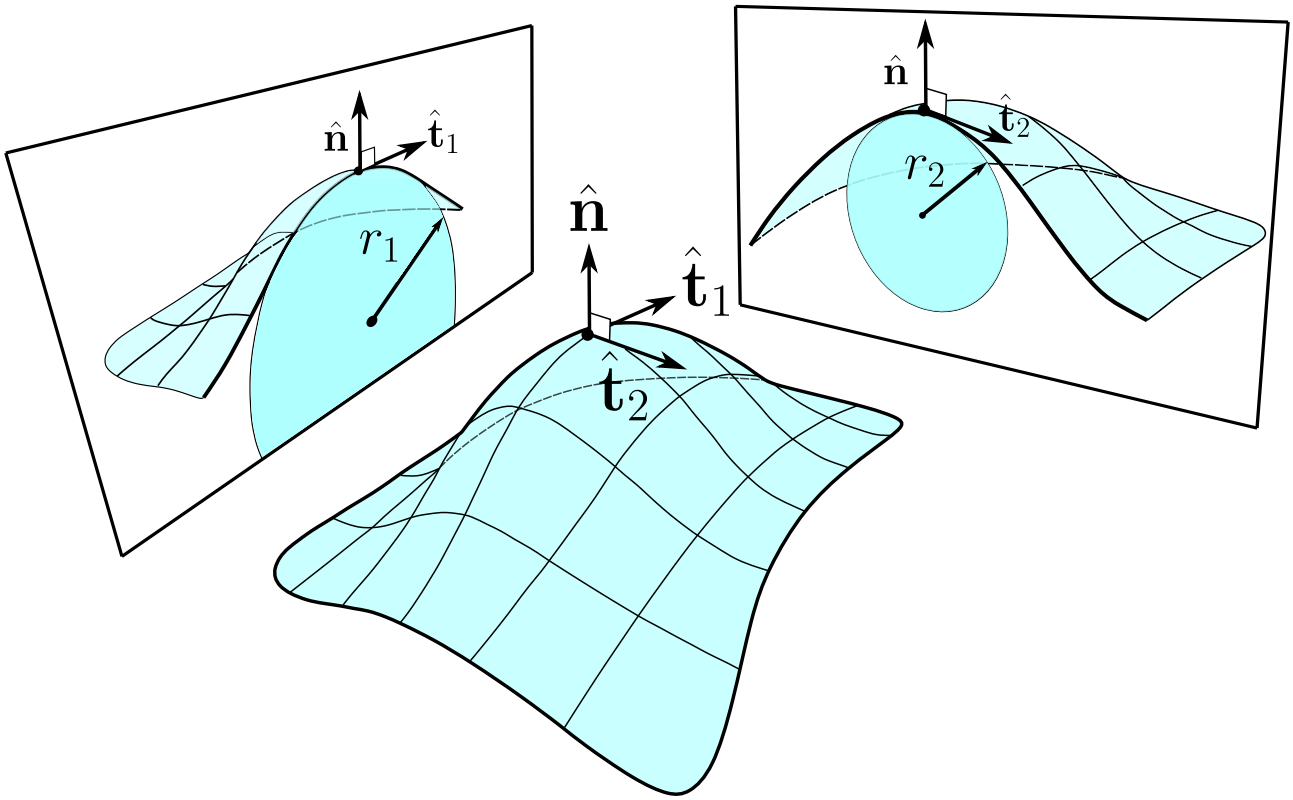

Figure 1.1: An illustration of surface curvature. In the centre, an arbitrary point on a surface is shown with an associated unit normal vector, $\hat{\mathbf{n}}$. The planes containing $\hat{\mathbf{n}}$ and an arbitrarily directed unit tangent to the surface, $\hat{\mathbf{t}}$, are termed normal planes. The intersection of a normal plane with the surface is a smooth curve: the normal curvature is the inverse of the radius of the circle which fits the curve at the distinguished point. Two orthogonal unit tangent vectors, $\hat{\mathbf{t}}_1$ and $\hat{\mathbf{t}}_2$, may be defined, whose normal planes contain the minimum and maximum normal curvature, shown by the left and right projections in the figure, respectively. These directions are termed the principal directions and contain the principal radii of curvature, r_1 and r_2. Adapted from *Crane et al.* (2013).

Now consider two immiscible phases in free space, neglecting perturbative effects of gravity. Intuitively, one phase will form a sphere – common analogues are rain droplets in air or

oil droplets in water. Qualitatively, this phenomena can be explained by recognising that interfaces between phases are energetically unfavourable. A measure of the energy associated with the creation of an interface is the interfacial tension, σ, which represents the energy per unit area required to break the intermolecular bonds within a single phase and create an interface. Spheres, which exhibit the smallest surface area per unit volume, represent the least energy configuration. The curvature of a spherical interface is clear – both principal radii of curvature are equal to the radius of the sphere itself. However, the radius of the sphere – or equivalently the radii of curvature – is determined by the fluid pressures: the sphere will contract until the pressure inside the sphere balances the reduction in radius. A quantitative relation between the fluid pressures and the interfacial curvature can be achieved by considering the thermodynamics of the system (*de Gennes et al.*, 2004).

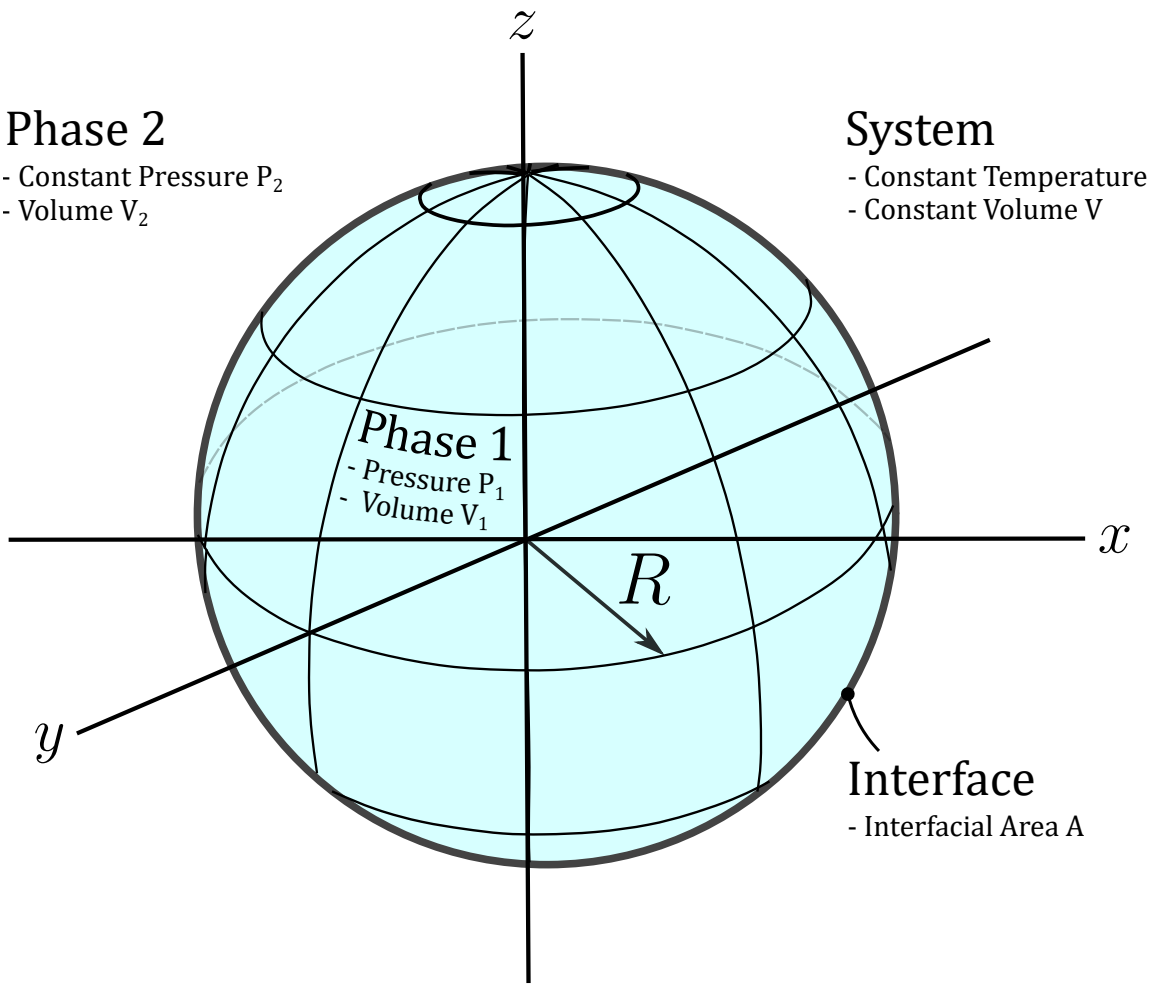

Figure 1.2: An illustration of two immiscible fluids forming a spherical fluid-fluid interface with radius R and area A. By considering the total volume and temperature of the system fixed, and the pressure of phase 2 to be constant, a variational approach can be used to minimise the Helmholtz free energy of the system. The result is the Young-Laplace equation, which relates the difference in fluid phase pressures to the mean curvature of the fluid-fluid interface.

In Fig. 1.2, the total volume (V) and temperature (T) of the two-fluid system is constant, and the pressure of phase 2 is fixed. The objective is to find the shape of the interface in its least energy configuration, and for simplicity an axisymmetric surface is assumed. The Helmholtz free energy of a system is given by,

$$F = U - TS + \sum_i \sigma_i A_i \tag{1.1}$$

where U is the internal energy of the system and S is the entropy. The surface energy of interfaces is given by $\sigma_i A_i$, where the summation is over all interfaces present. The internal energy can further be expressed in terms of the Gibbs free energy, G, which is constant for the

system in Fig. 1.2 as there will be no change in chemical potential:

$$U = G + TS - PV. \tag{1.2}$$

Substituting Eq. 1.2 into Eq. 1.1 and noting that the system has a single interface, F can be expressed as:

$$F = \sigma A - PV + G. \tag{1.3}$$

Recalling that the total volume and the pressure of phase 2 are constant, F can be further simplified:

$$\begin{aligned} F &= \sigma A - P_1 V_1 - P_2 V_2 + G \\ F &= \sigma A - P_1 V_1 - P_2 (V - V_1) + G \\ F &= \sigma A + V_1 (P_2 - P_1) - \underbrace{P_2 V + G}_{\text{constants}} \\ F &= \sigma A + \Delta P V_1 + C, \end{aligned} \tag{1.4}$$

where C represents all constant terms and $\Delta P = P_2 - P_1$ is the pressure difference between the phases.

Evaluating Eq. 1.4 for the spherical two-fluid system in Fig. 1.2, the Helmholtz free energy is finally given by

$$F = 4\pi\sigma \int_0^R x \left(1 + z_x^2\right)^{\frac{1}{2}} dx + 4\pi\Delta P \int_0^R xz \, dx + C, \tag{1.5}$$

where the first integral represents the energy associated with the area of the interface between the fluids and the second integral is the energy associated with the volume of phase 1.

To find the least energy configuration, F can be expressed as a functional

$$F = \int_0^R f(x, z, z_x) \, dx, \tag{1.6}$$

and the necessary condition to minimise F can be obtained through the Euler-Lagrange equation,

$$\frac{\partial f}{\partial z} - \frac{d}{dx}\left(\frac{\partial f}{\partial z_x}\right) = 0, \tag{1.7}$$

where $f(x, z, z_x) = \sigma x \left(1 + z_x^2\right)^{\frac{1}{2}} + \Delta P x z$. Substituting f into Eq. 1.7 and simplifying, one obtains:

$$\Delta P = \sigma \left(\frac{z_x}{x \left(1 + z_x^2\right)^{\frac{1}{2}}} + \frac{z_{xx}}{\left(1 + z_x^2\right)^{\frac{3}{2}}} \right). \tag{1.8}$$

This is known as the Young-Laplace equation (*Young*, 1805; *Laplace*, 1805), written in differential form. On the left hand side, the difference in fluid pressures is commonly known as the capillary pressure and denoted by P_c. On the right, the terms in brackets represent the two principal curvatures of the interface (Fig. 1.1). In short, for any fluid interface in equilibrium, the sum of the principal curvatures is directly proportional to the capillary pressure. The traditional form of the Young-Laplace equation is therefore,

$$P_c = P_2 - P_1 = \sigma \left(\frac{1}{r_1} + \frac{1}{r_2} \right) = \sigma \kappa, \tag{1.9}$$

where κ is termed the total curvature[1]. In this thesis, the principal radii of curvature are positive if phase 2 is protruding into phase 1. Note that, in equilibrium, the principal radii of curvature may vary independently over the interface provided that their sum is equal everywhere.

Wettability

In the presence of a solid, the affinity of a fluid phase to be in contact with the solid is called the wettability, and it is defined by the angle of contact between the solid and the fluid-fluid interfaces. By convention, the contact angle is measured through the densest phase – phase 1 in this thesis. At each solid-fluid and fluid-fluid interface, there exists an associated interfacial tension, as explained previously. The conventional way to illustrate the contact angle is to consider interfacial tension as a force, and to perform a horizontal force balance at a point on the three-phase contact loop (*Blunt*, 2017).

[1] In differential geometry literature, the total curvature refers to the sum of the Gaussian curvature – which is the product of the principal curvatures – over the surface.

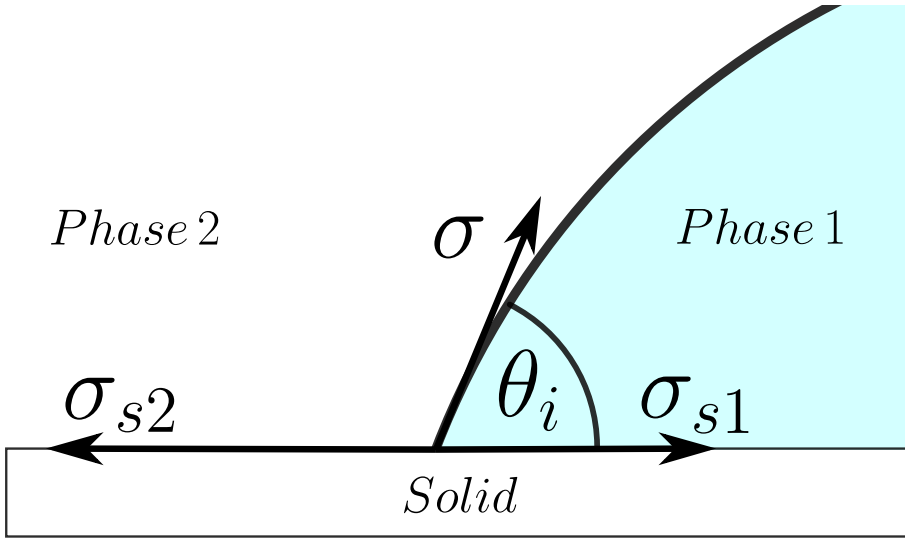

Figure 1.3: Two immiscible fluid phases in contact with a solid surface. A horizontal force balance at the three phase contact point relates the interfacial tensions of the interfaces, σ, to the intrinsic contact angle, θ_i, through the Young equation.

Figure 1.3 shows two phases in contact with a solid, and the associated interfacial tensions acting at the three-phase contact point. The Young equation relates the tensions via the intrinsic contact angle:

$$\sigma_{s1} = \sigma_{s2} + \sigma cos\theta_i. \tag{1.10}$$

From Fig. 1.3, it is obvious that changing the contact angle will change the equilibrium shape, and hence the interfacial curvature, of the spherical droplet. For any given capillary pressure, the interfacial curvature of fluid interfaces in the presence of a solid is controlled by the local wettability and the solid geometry. However, the wettability and geometry are both scale-dependent properties.

The intrinsic contact angle present in the Young equation represents the contact angle if it were measured on a smooth surface. In reality, surfaces are not smooth at any scale. At the pore scale, an effective contact angle is observed, which represents the equivalent angle on a smooth surface required to produce the same interfacial curvature (*Blunt*, 2017). Additionally, surface roughness and chemical heterogeneity cause pinning of the contact loop – there can be a wide range of effective contact angles, termed hinging angles, at which the interface has no apparent movement at the pore scale. Displacement only occurs when a critical angle is

reached; these critical angles are known as the advancing or receding contact angles (*Morrow*, 1975). This phenomena, along with the directional dependency of the effective angle, is termed contact angle hysteresis (Fig. 1.4).

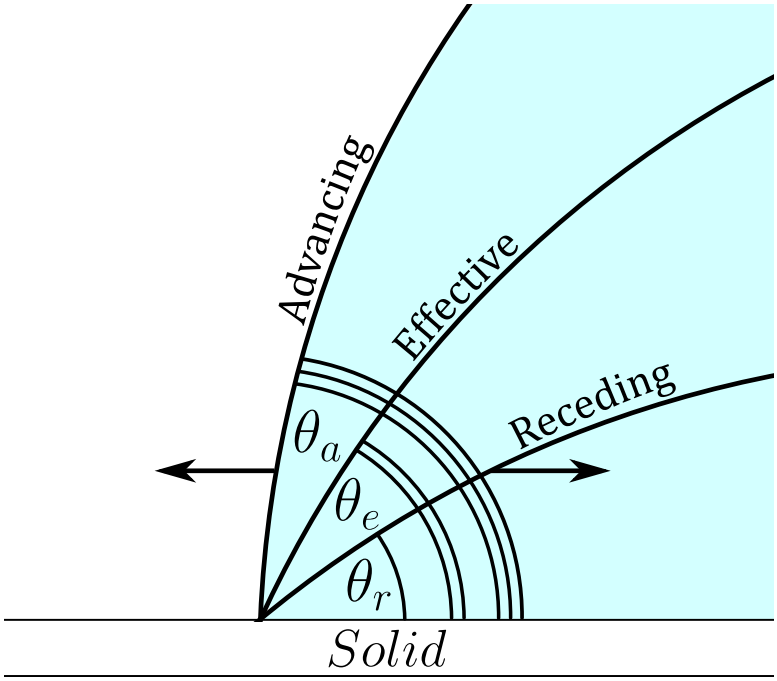

Figure 1.4: An illustration of contact angle hysteresis. At equilibrium, pore-scale observations reveal an effective contact angle θ_e. Surface heterogeneities, both physical and chemical, can cause the interface to remain pinned within a range of effective contact angles, spanning the advancing and receding contact angles. The interface displaces at these critical advancing and receding angles.

From the perspective of an invading phase, if the advancing contact angle is less than $90°$ the invading fluid is deemed the wetting phase, while if it is greater than $90°$ the invading fluid is considered non-wetting. Exactly at $90°$, there is no preference for either fluid to contact the solid and the system is termed neutrally wet. It is possible, and indeed common, to have a wide range of contact angles present in a porous medium (e.g, *AlRatrout et al.*, 2017; *Alhammadi et al.*, 2017). Media with contact angles both above and below $90°$ are termed mixed-wet, and will be the topic of Chapter 5.

1.2.2 Displacement at the Pore Scale

At rest, fluids will contact a solid at their equilibrium contact angle and the fluid-fluid interface will adopt a corresponding curvature described by Eq. 1.9. Displacements, however, occur out

of equilibrium.

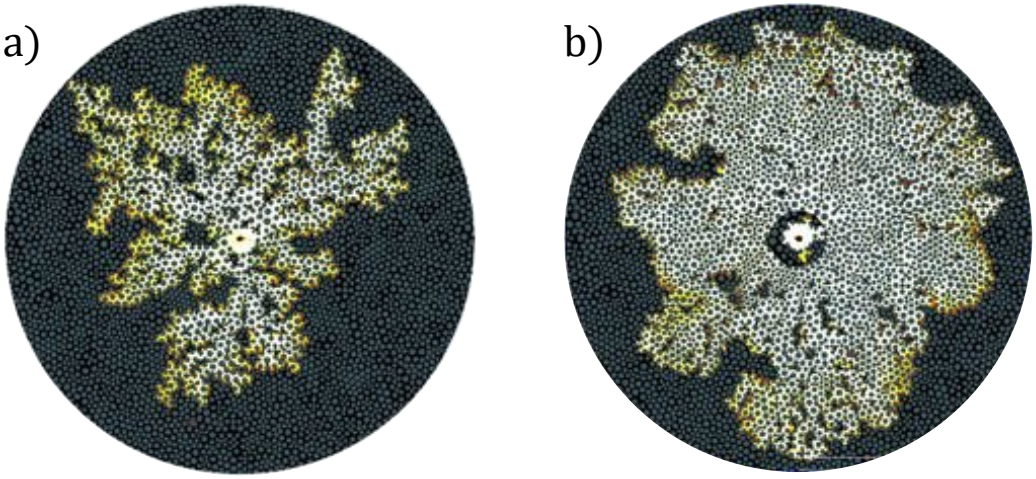

Figure 1.5: Micromodel experiments showing the characteristic invasion pattern during drainage (a) and imbibition (b). Drainage tends to create narrow finger-like growths as the invading fluid rapidly displaces into the largest pathways. Imbibition engenders a flatter invasion front due to cooperative pore-body filling. Figure adapted from *Zhao et al.* (2019).

A change in capillary pressure will elicit a change in interfacial curvature until the advancing or receding contact angle is achieved. At this point, the interface will displace to a new position of equilibrium. The exact nature of the displacement is dependent upon the wettability of the system and will be briefly discussed below.

Drainage

Displacement of a wetting phase by a non-wetting phase is termed drainage. Natural analogues are hydrocarbons seeping from a source rock into a reservoir or CO_2 injection into a saline aquifer. If a cylindrical pore space is assumed, the Young-Laplace equation becomes $P_c = 2\sigma \cos\theta_R / r$, where r is the inscribed radius of the cylinder and θ_r is the receding contact angle of the defending phase. From this, it is clear that the invading fluid pressure will increase with decreasing r – during drainage, the smallest regions of the pore space offer most resistance to flow. Once the threshold capillary pressure required to displace through a narrow region has been achieved, the invading fluid can move rapidly into the subsequent wider regions in a phenomenon know as a Haines jump (*Haines*, 1930). Drainage tends to displace into the pore space in a finger-like fashion (Fig. 1.5a).

Mathematically, displacement during drainage is described by an invasion percolation process

(*Lenormand and Bories*, 1980; *Wilkinson and Willemsen*, 1983): filling proceeds in decreasing order of size and the leading fluid menisci are always directly connected to the injection side of the medium. This is distinct from imbibition, in which displacement can occur even when no apparent connectivity with the inlet is visible.

Imbibition

Displacement of the non-wetting phase by a wetting phase is known as imbibition. Common examples are water soaking into soil or paper absorbing a spilled liquid. Here, the most difficult step is filling the largest regions of the pore space which require the smallest capillary pressure (*Blunt*, 2017).

The widest regions of the pore space – the pores – tend to be connected to many surrounding narrower restrictions, called throats. The first major difference between drainage and imbibition arises due to pores limiting displacement: the greater the number of wetting-phase occupied throats surrounding a pore, the easier it is (greater capillary pressure) to displace into that pore. This is termed cooperative pore-body filling (*Lenormand et al.*, 1983) and engenders a relatively flat invasion front (Fig. 1.5b), as opposed to finger-like growths during drainage.

The second major contrast is that, unlike drainage, it is favourable for the medium to contact the wetting phase. As a result, the wetting phase is almost always present in the corners and crevices of the pore space, forming micrometre-thick layers. These wetting layers are a central theme in chapters 4 and 5. As the wetting phase is injected, layers from adjacent corners will swell until they meet (Fig. 1.6). Further displacement is not possible without a local increase in capillary pressure, creating an instability leading to rapid local filling. This is termed snap-off (*Pickell et al.*, 1966) and it first occurs in the narrowest throats of the pore space. Snap-off blocks flow paths and can result in significant trapping of the non-wetting phase.

The critical capillary pressure at which snap-off occurs is often considered a function of only one radius of curvature (*Lenormand et al.*, 1983). Indeed, Fig. 1.6 explicitly acknowledges curvature in only one plane, but it is clear from Fig. 1.6a that wetting layers conform to the

geometry of the solid walls. Thus, axiomatically stating that only one component of curvature is non-zero is likely incorrect. While some studies have tested this assumption (e.g, *Deng et al.*, 2014; *Raeini et al.*, 2014), detailed evaluation is needed. A three-dimensional discussion of the pore space is further developed Section 1.3, and Chapter 3 will provide an analysis of snap-off curvature.

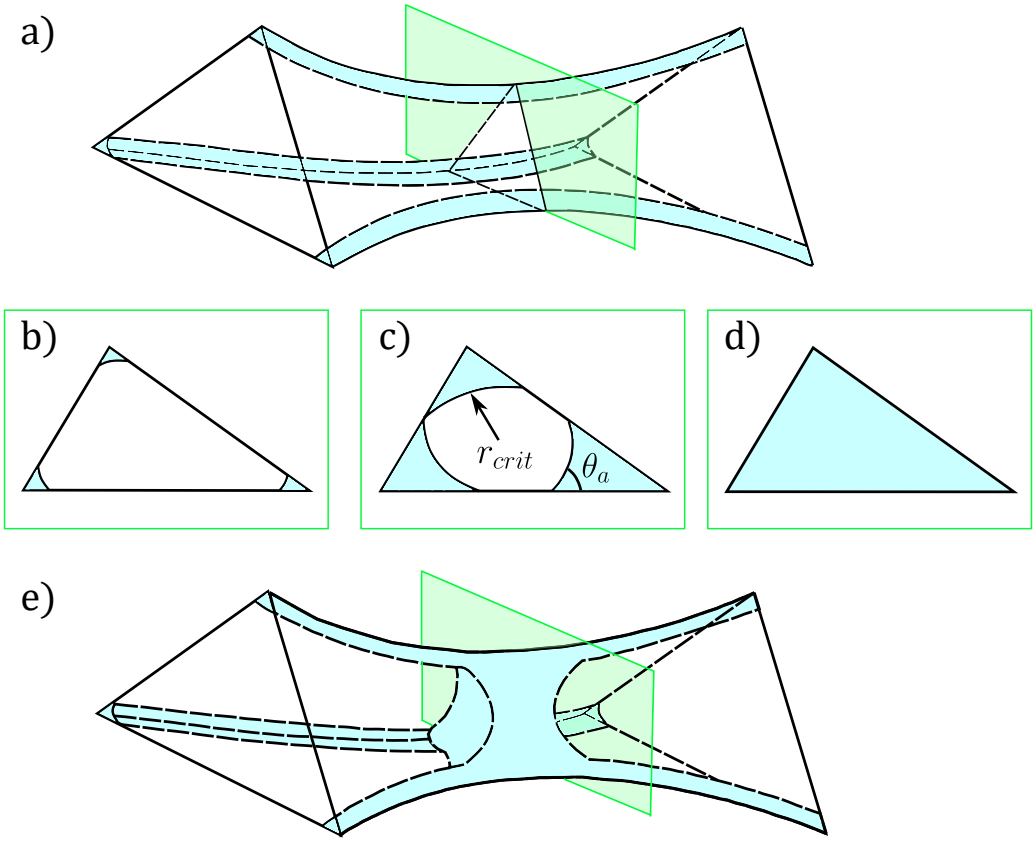

Figure 1.6: Illustrations showing the snap-off process. Wetting layers are almost always present in the corners of the pore space, shown in (a). An axial cross-section through the narrowest region – the throat centre – is highlighted in green and shown in (b)-(d). Initially, the wetting layers reside near the corner vertices (b). An increase in wetting phase pressure causes the layers to swell until an advancing contact angle (θ_a) is reached. Further pressure increase moves the layers toward the centre of the throat until a critical curvature, $1/r_{crit}$, at which the layers of two neighbouring corners meet (c). This configuration is unstable, resulting in the rapid filling of the throat (d). Snap-off blocks flow paths and causes significant trapping in wetting media (e). Adapted from *Blunt* (2017).

Mathematically, the snap-off process results in imbibition being described by ordinary percolation: filling is in increasing order of size but does not need to be directly connected through the centre of the pore space.

1.2.3 Relative Permeability

The wettability of the medium controls the local displacements processes, which in turn control the configuration of the fluids at the pore scale. The pore-scale configuration, however, determines how easily fluids will move through the pore space. Together with the average pore-scale capillary pressure, relative permeability comprises a macroscopic description of flow in permeable media and is of utmost importance. For example, in designing the optimal diffusion layer for a fuel cell, it is crucial to know how easily water by-product can exit and reactant hydrogen can enter the cell.

The multiphase Darcy Law (*Muskat and Meres*, 1936) relates the Darcy velocity $\mathbf{q}$ [ms^{-1}] of a phase α to its relative permeability k_r:

$$\mathbf{q}_\alpha = \frac{-Kk_{r\alpha}}{\mu_\alpha}\left(\nabla P - \rho_\alpha \mathbf{g}\right), \tag{1.11}$$

where K [m^2] is a tensor representing the intrinsic permeability of the medium, ∇P [Pa m^{-1}] is the pressure gradient across a representative volume of the sample, and μ [Pa s] and ρ [kg m^{-3}] are the phase viscosity and density, respectively. The relative permeability is a coefficient, $0 \leq k_{r\alpha} \leq 1$, which accounts for the higher pressure drops observed during multiphase flow compared to single-phase flow for the same flow rate (*Blunt*, 2017), and is a function of the phase saturation (S_α). Generally, the sum of the relative permeabilities is less than one – multiple phases impede each other.

1.3 Previous Studies

In this section, a review of previous pore-scale modelling and wettability research will be provided. The concept of direct simulation of multiphase flow will be introduced and some of its advantages and limitations briefly discussed. Subsequently, pore-network modelling is given a detailed treatment and the current shortcomings are identified. While this thesis focuses on the development of pore-network models and physical understanding, frequent use of direct methods will be employed to inform and evaluate these advancements. Finally, the topic of mixed wettability is given a thorough treatment with the key research questions

highlighted.

1.3.1 Direct Numerical Simulation of Multiphase Flow

Direct approaches simulate flow directly on the pore space of a reconstructed 3D sample or micro-CT scan of a porous medium. The methods either solve the Navier-Stokes equations using Eulerian grid-based methods (finite-element, finite-volume and finite-difference) (*Huang et al.*, 2005; *Raeini et al.*, 2012) or consider fluid motion as the propagation and collision of fictitious particles, for example lattice Boltzmann (LBM) (*Pan et al.*, 2004; *Porter et al.*, 2009; *Akai et al.*, 2020a) or smoothed particle hydrodynamics (SPH) (*Tartakovsky and Meakin*, 2006) methods. Whilst both approaches are widely used to simulate flow through tens to hundreds of pores (e.g, *Pan et al.*, 2004; *McClure et al.*, 2021; *Maes and Menke*, 2021), direct simulations are often hindered by their computational demands; the time dependency and non-linearity of the task poses an extreme challenge and even small-scale simulations require require CPU (*Pan et al.*, 2004) or GPU (*An et al.*, 2017) parallelisation. The development of a computationally efficient model which accurately captures pore-scale behaviour through representative elementary volumes for complex systems remains a crucial step towards achieving predictive capability for multiphase flow. Ultimately all direct methods are computationally expensive, especially for capillary dominated flow, making them of limited use for predicting macroscopic properties and displacement sequences through large samples. The limitations of direct methods lead to a network modelling approach, and the predictions from the two methods are compared in chapter 4.

1.3.2 Pore-Network Modelling of Multiphase Flow

An alternative to direct simulation is to represent the pore space as a network of nodes (pores) and connecting bonds (throats). Pioneered by *Fatt* (1956), pore-network models offer a more feasible means to simulate flow through large samples efficiently. The initial networks considered were regular lattices, in which the coordination number and network element properties were varied (e.g, *Chatzis and Dullien*, 1977; *Jerauld and Salter*, 1990; *Koplik*, 1982; *Dixit et al.*, 1999). However, regular lattices are not representative of reality. Subsequent

efforts focused on disordered topology through the use of Voronoi diagrams (*Blunt and King*, 1990) and Delauney tessellations derived from numerically simulated diagenesis (*Bryant and Blunt*, 1992; *Bryant et al.*, 1993a,b). Disordered representations improved predictions, which led to further efforts in creating networks statistically equivalent to two-dimensional thin sections of geologic media. It is now possible, owing to the development of DRP, to extract a network directly from a three-dimensional micro-CT image of a real sample (e.g *Dong and Blunt*, 2009) (Fig. 1.7). This latter approach is the most accurate representation of the original medium, and will be the method of choice in this thesis.

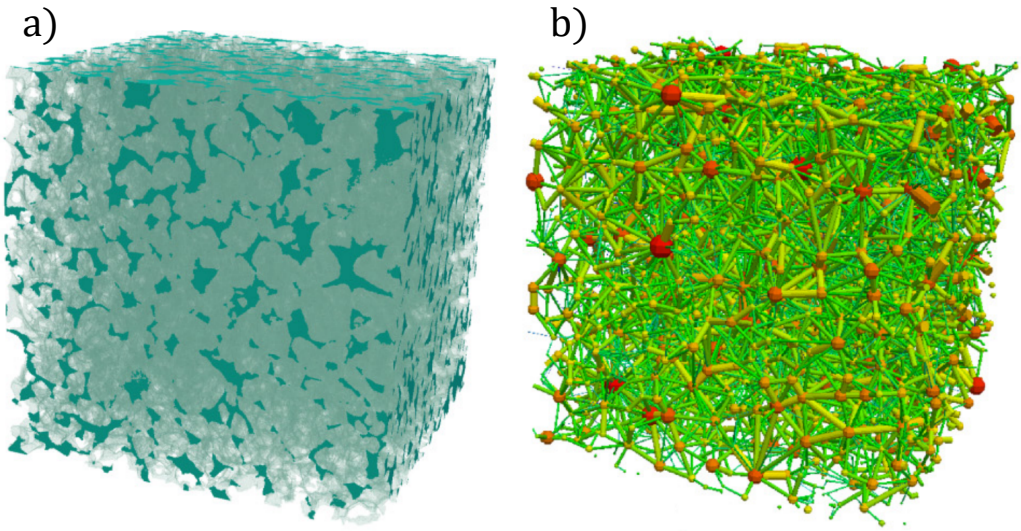

Figure 1.7: A three-dimensional rendering of an X-ray imaged Benthemier sandstone (a) next to a pore network extracted from the same image (b). Adapted from *Raeini et al.* (2017).

The connectivity of the extracted network preserves the pore-space topology of the real medium (Fig. 1.7), while the pores and throats can be represented by simple one, or two, dimensional geometric shapes, greatly reducing the complexity of a real image. Fluid displacement through the ideal network is simulated semi-analytically, requiring far less computational resources and time than direct methods. However, a key limitation to network modelling is the loss of physical detail caused by conceptualising the pore space into idealised one, or two, dimensional shapes (Fig. 1.8).

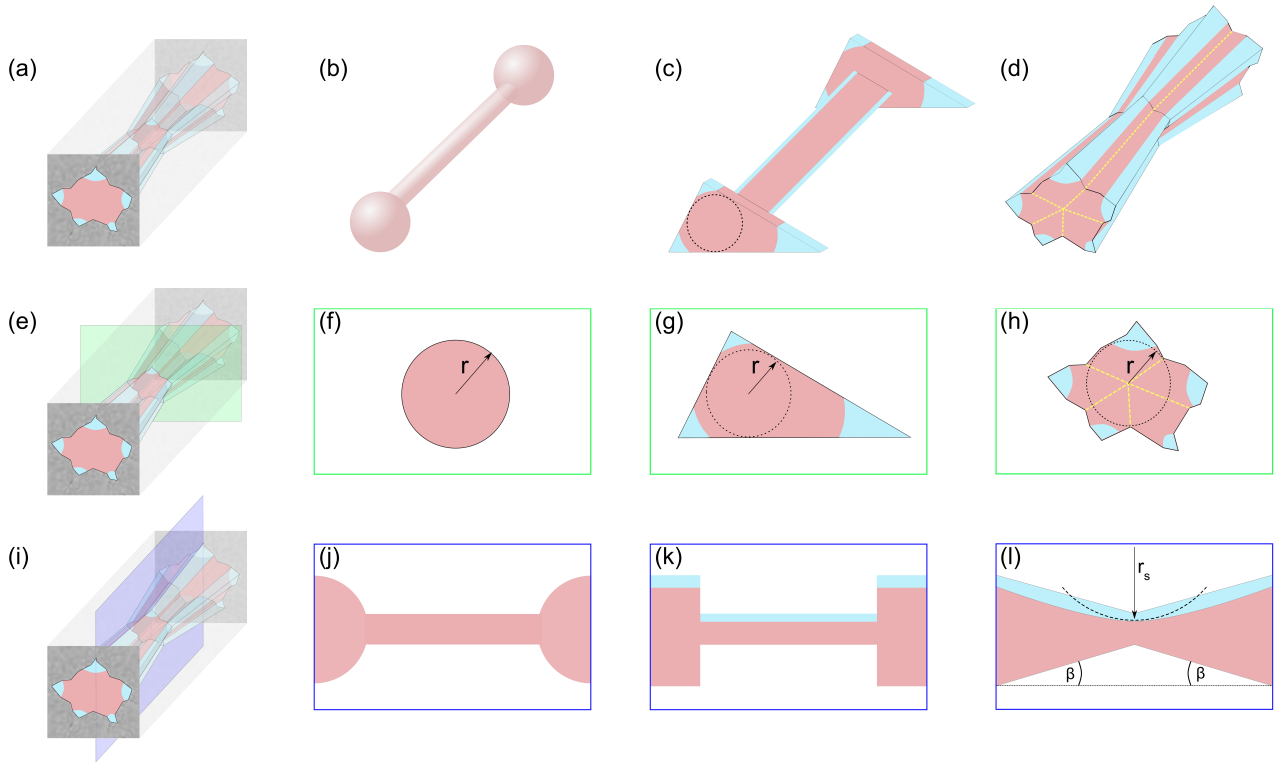

Figure 1.8: A schematic of a porous medium (a) and its axial (e) and sagittal (i) planes. The network representation of the medium using a variety of network extraction approaches is shown in (b-d). Early network models represented the pore space using circular elements (b), which preserve the inscribed radius of the pores and throats, r, and topology of the medium. However, circular elements do not preserve the corners of pore space in the axial plane (f), nor the geometry of the medium in the sagittal plane (j), and so the medium is modelled as a quasi one-dimensional system. The development of classical methods idealises the pore space as simple shapes, such as triangles or squares (c). Simple shapes preserve corners in the axial plane (g) allowing wetting layers to be modelled, but neglect the geometry of the medium in the sagittal plane (k) — the network is merely a two-dimensional representation of the real, three-dimensional medium. The generalised network model (GNM) discretises the medium using the corners of the pore space, shown by the dashed yellow lines in (d), which form the elements of the network. In the axial plane, the GNM preserves the number of corners present in the real medium (h). This work provides new formulations for the three-dimensional features preserved in the sagittal plane (l), namely the pore-space expansion (β) and the sagittal curvature (r_s) of layer interfaces. From *Giudici et al.* (2023a).

Early PNMs represented the larger regions in the pore space, termed pores, and the connecting narrower restrictions, termed throats, by circular or cylindrical network elements (Fig. 1.8b). Discretising the pore space as a network of circular elements preserves the topology of a permeable medium and provides simple, semi-analytic expressions for fluid-fluid displacement (*Chatzis and Dullien*, 1977; *Diaz et al.*, 1987), but renders it impossible to model flow through wetting layers present in the corners of the pore space (Fig. 1.8a). Additionally, semi-analytic approximations are derived from a quasi one-dimensional system; the inscribed radius, r, is

preserved, but all other detail in the axial (Figs. 1.8e and f) and sagittal (Figs. 1.8i and j) planes is lost.

To address these shortcomings, the advent of classical network models (CNM) saw the use of simple geometric shapes, such as triangles and squares (*Blunt*, 1997; *Bakke and Øren*, 1997), to represent the pores and throats of a medium with wetting layers present in its corners (Fig. 1.8c). The classical approach maintains the efficiency and topology inherent to all network models, and has been used to reproduce upscaled flow properties in simple cases successfully (e.g, *Øren et al.*, 1998; *Lerdahl et al.*, 2000; *Valvatne and Blunt*, 2004). Despite improvements, classical approaches idealise the pore space as a quasi two-dimensional system — the axial plane (Fig. 1.8g) solely provides the geometric detail used to derive semi-analytic approximations, whilst the geometry of the solid and the fluid-fluid interfaces in the sagittal plane are ignored (Fig. 1.8k). This is a poor representation of multiphase flow through nearly all media, and direct numerical studies on synthetic media have shown that three-dimensional features present in the sagittal plane have a large impact on pore-scale flow (e.g, *Deng et al.*, 2014; *Rabbani et al.*, 2018). Furthermore, *Bondino et al.* (2013) showed that the classical elements themselves are non-unique and do not preserve the exact geometry of the underlying medium, leading to unreliable predictions: for example, the percentage difference in water relative permeabilities was shown to be as large as 75% using different classical network extractions from the same image. A solution to the shortcomings of classical approaches is a network model which captures the fully three-dimensional features of a real medium, with physical approximations that consider both the axial and sagittal planes.

Figure 1.8d shows the generalised network model (GNM) (*Raeini et al.*, 2017, 2018), which was developed to better discretise the geometry and connectivity of the pore space in three dimensions and will be explained in detail in Chapter 2. In the axial plane, the GNM preserves the number of corners present in the underlying image (Fig. 1.8h). The corners of the pore space form the elements of the network, which include all void-space voxels between two neighbouring pores, shown in Fig. 1.8d. Using the corners to discretise the pore space, it naturally follows that geometric detail in the sagittal plane can also be preserved (Fig. 1.8l). To date, however, the precise formulations of pore-space expansion, β, and sagittal curvature

of fluid-fluid interfaces, r_s, in a network model have been largely unexplored. To obtain predictions truly representative of a real three-dimensional system, it is necessary to ensure that semi-analytic approximations correctly account for the effect of three-dimensional features on fluid-fluid interfaces. In Chapter 3, the GNM is further developed to consider the three-dimensional nature of a real medium, and the effect that this has on macroscopic predictions is quantified.

1.3.3 Mixed Wettability

In Chapter 3, the impact of pore-space geometry on displacement in uniformly-wet media is analysed. Later, in Chapter 6, this analysis is extended to mixed-wet media. For several decades, mixed-wet media has been recognised for its favourable impact on hydrocarbon recovery in petroleum engineering and improved fuel cell efficiency in electrochemical engineering. Early experimental observations of waterflooding in geologic media showed significantly greater hydrocarbon recovery than in water-wet media (*Salathiel*, 1973; *Tanino and Blunt*, 2013), while altering the wettability of a percentage of a gas-diffusion layer showed increased fuel cell performance (e.g, *Lim and Wang*, 2004; *Park et al.*, 2008; *Chang et al.*, 2011; *Vijay et al.*, 2011). However, the origin of these phenomena were unknown, and it was an unspoken assumption that pore-scale displacement in the wetting and non-wetting clusters would be described by the same drainage and imbibition processes previously discussed, with flat interfaces present at the transition between regions.

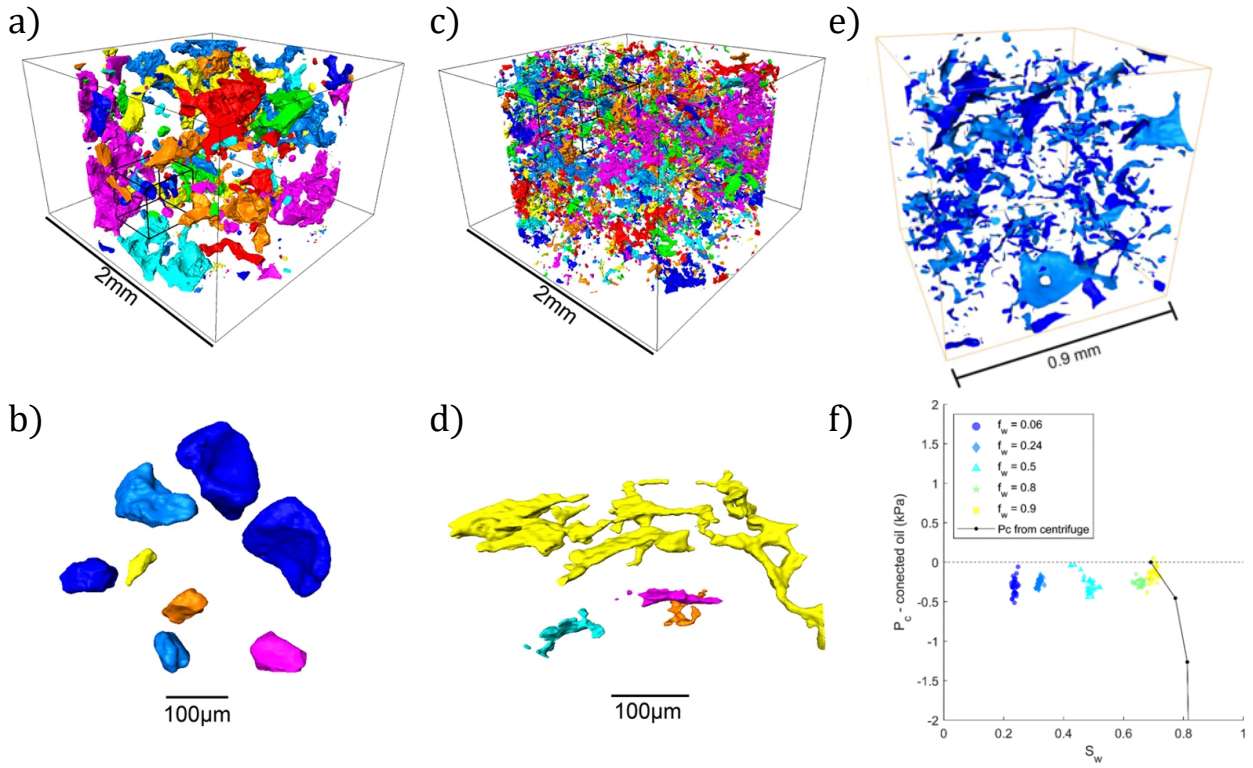

Figure 1.9: Visualisations of the fluid interfaces in water-wet (a,b) and mixed-wet (c,d,e) media, with the capillary pressure - saturation measurements for a mixed-wet medium at different fractional flows shown in (f). The fluid interfaces in the water-wet medium are approximately spherical, with similar principal curvature directions. Mixed-wet media, however, exhibit complex interfaces which span multiple pore regions and have very low mean curvature. A low mean curvature is maintained throughout the experiments, shown by the capillary pressure measurements in (e). Figures adapted from *Alhammadi et al.* (2017) and *Lin et al.* (2019).

Recently, significant progress has been made by DRP in imaging the intricacies of mixed-wet processes occurring at the pore scale, particularly concerning the shape of fluid-fluid interfaces. Pore-scale experiments conducted by *Alhammadi et al.* (2017) also displayed enhanced hydrocarbon recovery in a mixed-wet sample, but further revealed that the nature of the fluid interfaces is distinct from those observed in uniformly-wet media (Fig. 1.9a,b and c,d,e). The interfaces spanned multiple pore regions, maintaining two-phase connectivity throughout the medium, and exhibited a mean curvature an order of magnitude lower than expected. *Lin et al.* (2019) performed similar pore-scale experiments and established that displacement occurs at a remarkably low capillary pressure (Fig. 1.9f), with both fluids flowing concurrently throughout the duration of the experiments. The authors further noted that the fluid interfaces in mixed-wet media are approximately minimal surfaces. Minimal surfaces

have a zero mean curvature everywhere but are not necessarily flat; across the interface, the principal radii of curvature (Eq. 1.9) are equal in magnitude but opposite in direction (Fig. 1.10). Minimal surfaces were subsequently imaged in the fibrous gas-diffusion layer of a polymer-electrolyte membrane fuel cell (*Shojaei et al.*, 2022) and in quasi-two dimensional micromodel experiments (*Irannezhad et al.*, 2023), extending the pioneering body of research already conducted on these media (e.g, *Lenormand et al.*, 1988; *Oren et al.*, 1992; *Jordan et al.*, 2000; *Benziger et al.*, 2005; *Gostick et al.*, 2009; *Zhao et al.*, 2016).

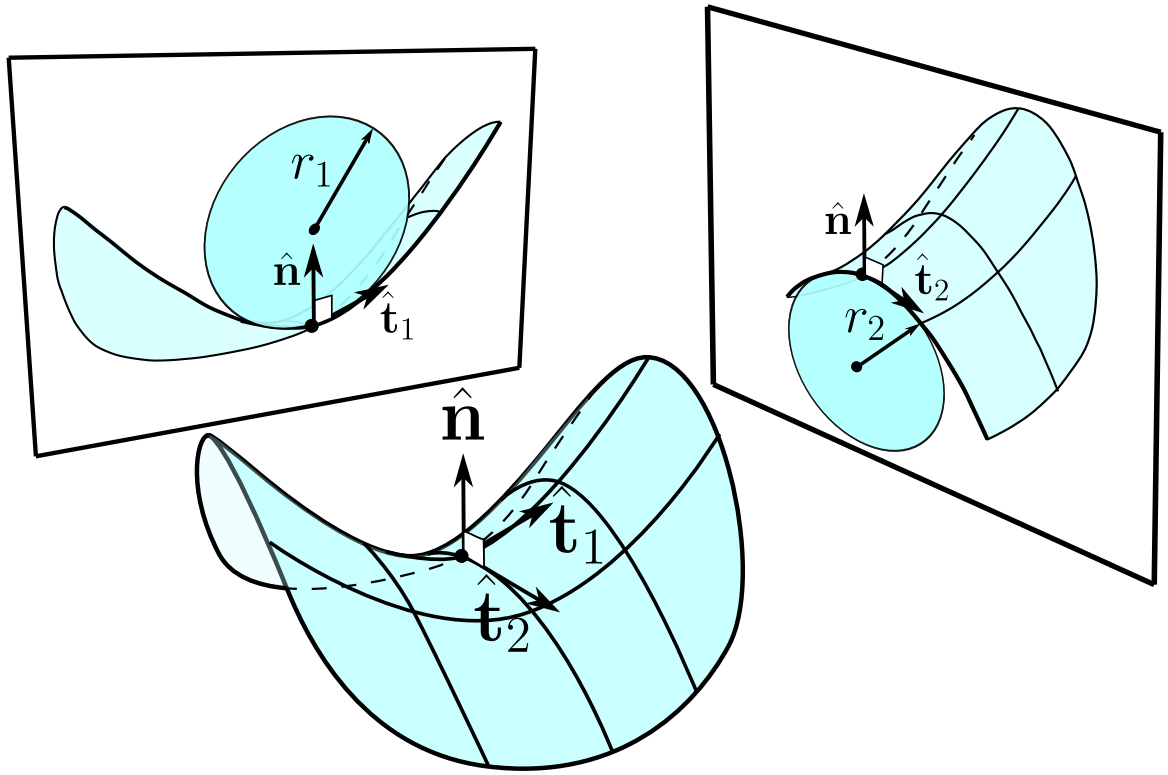

Figure 1.10: An illustration of the principal curvatures of a saddle-shaped minimal surface. At the chosen point on the centre surface, the principal curvatures are opposite in direction but equal in magnitude, shown by the projections to the left and the right. Adapted from *Crane et al.* (2013)

Minimal surfaces are thought to be responsible for the desirable nature of displacement observed in mixed-wet media; the Gauss-Bonnet theorem – which relates the topology of a surface to its curvature – implies high fluid connectivity for negative Gaussian curvature (minimal) surfaces (*Armstrong et al.*, 2019). However, the specific conditions at which minimal surfaces will form in porous media, and how their displacement proceeds at such a low capillary pressure, remains poorly understood. The stability and displacement of minimal surfaces are thus important research questions and are addressed in Chapter 5.

1.4 Novel Contributions

To summarise, two main research themes were outlined in the previous section: the impact of a three-dimensional consideration of the pore space on two-phase flow predictions, and the nature of displacement in mixed-wet media. The research contained in this thesis contributes the following advancements to the field:

- An extension to the physical approximations in current network models, which explicitly acknowledges the third spatial dimension and allows for a more accurate representation of the complex interfacial curvature present in real porous media.
- A detailed demonstration of the positive impact that a three-dimensional representation of interfacial curvature has on macroscopic predictions.
- A comparison between pore-network modelling and direct simulations for a variety of wetting states, revealing which method offers higher predictive accuracy at the macroscopic scale.
- A thorough assessment of the conditions at which fluid interfaces are stable in three-dimensional media, for any wettability.
- A physically-based explanation of low capillary pressure displacement in mixed-wet media and an empirical relation which predicts the threshold displacement pressure.
- A newfound recognition of the importance that pore-space geometry has in pore-scale displacement across all wetting states.

1.5 Thesis Outline

This thesis investigates the impact of wettability and geometry on pore-scale displacement using a variety of approaches and incorporates the findings into a framework suitable for network modelling. The thesis is organised as follows:

Chapter 2 describes the **generalized network model** (GNM) which is further developed and used extensively in this thesis.

Chapter 3 presents a **representation of fully three-dimensional interfacial curvature in pore-network models**, and shows the enhanced predictive capability for water-wet media using the GNM.

Chapter 4 presents a **comparison of the GNM to lattice-Boltzmann simulation**, evaluating their respective abilities to capture wettability-dependent pore-scale processes.

Chapter 5 investigates **interface stability and displacement in mixed-wet media**. The wetting and geometric conditions necessary for minimal surface formation are presented, and a finite-element approach is used to understand the stability and displacement of these surfaces. An empirical relation is found which accurately predicts the threshold displacement pressure of a mixed-wet interface.

Chapter 6 summarises the main **conclusions**, **achievements** and opportunities for **future work** provided by this thesis.

CHAPTER 2

THE GENERALIZED NETWORK MODEL

2.1 Overview

In this chapter, the generalized network model for quasi-static multiphase flow is described. First, the method of extracting a generalized network from a three-dimensional micro-CT image is explained. Next, the simulation of two-phase flow through the extracted network is presented. Finally, the chapter concludes with an assessment of the advantages that the generalized method has over classical approaches, and the opportunities for further development that will be explored in subsequent chapters.

2.2 Generalized Network Extraction

The initial stages of generalized network extraction (GNE) are similar to the medial surface and maximal ball methods explained elsewhere (e.g, *Sheppard et al.*, 2005; *Dong and Blunt*, 2009). Here, the extraction process is divided into two for clarity: first, the extraction of the topology and the pore regions of the pore space are explained. Next, the additional steps taken to discretise the pore space into corners (Fig. 1.8D) and to describe corner geometry are introduced. It is the latter, corner-related approach which separates the GNM from classical treatments. Note that the aim here is to provide a conceptual understanding of GNE – for a more thorough treatment, the reader is referred to *Raeini et al.* (2017).

2.2.1 Topology Preserving Extraction and Identification of Pore Regions

The topology of any n-dimensional geometry is described by its medial axis, which can be thought of as the geometry's skeleton. Typically, for a permeable pore space in three-dimensions, the set of points belonging to the medial axis will form a two-dimensional surface: the topology of the pore space is uniquely preserved by its medial surface.

To find the medial surface of a pore space from a three-dimensional image, the distance map must first be determined. The distance map is a scalar field: each void-space voxel in the image is assigned a value corresponding to the Euclidean distance between the given voxel and its nearest solid voxel (Fig. 2.1a). The distance map can be visualised as a collection of spheres, where each voxel's centre is the centre of a sphere and the sphere's radius is the distance map value of the voxel (Fig. 2.1b). These spheres are called inscribed spheres.

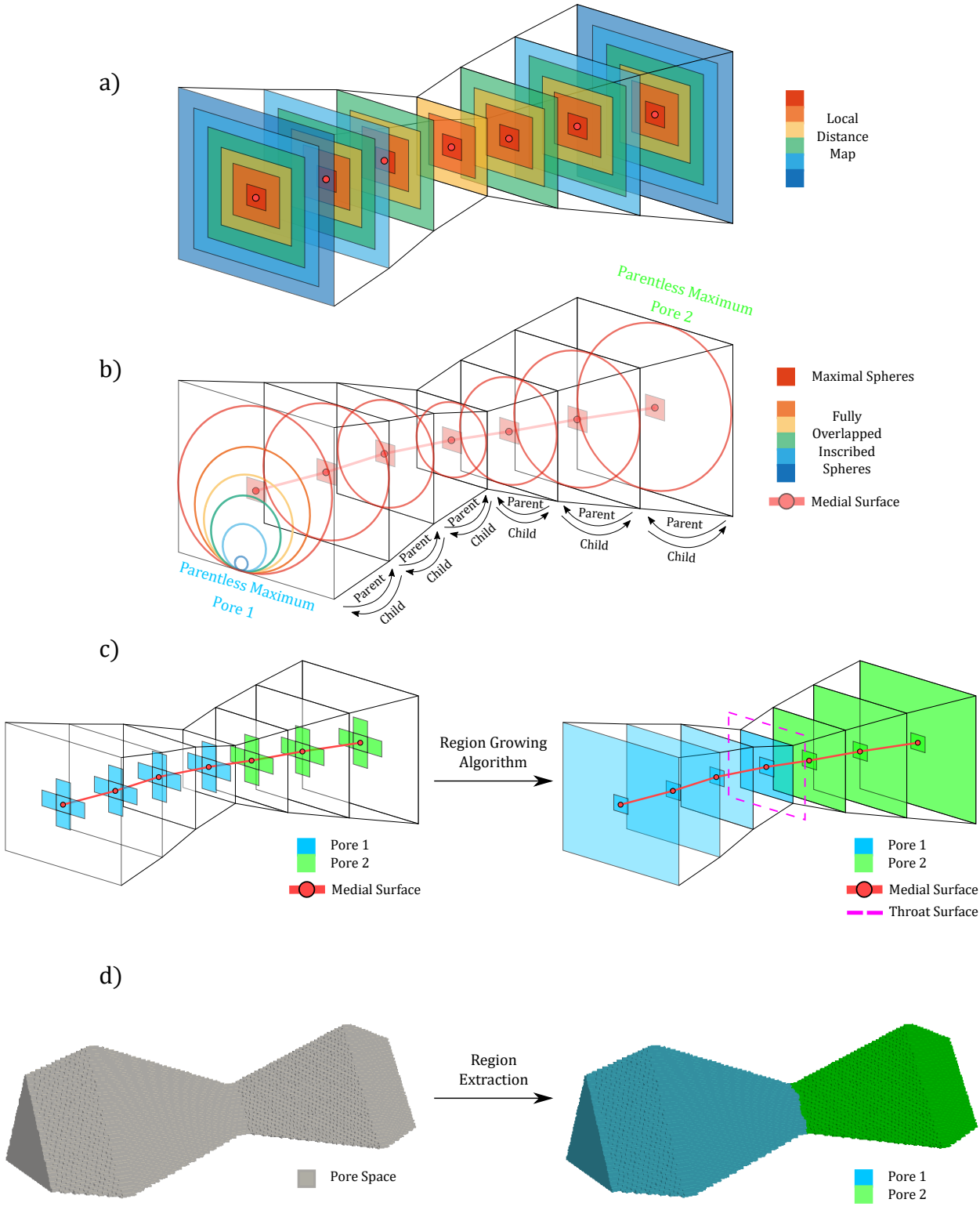

Figure 2.1: An illustration of the first stage of generalized network extraction. In (a), the distance map of the pore space is shown by the various colours. The distance map can be visualised as a collection of spheres, shown in cross section in (b). The surface joining the centres of the local maximal spheres defines the medial surface. The maximal spheres are subject to a parent-child hierarchy, with parentless spheres defining pore centres. In (c), the children of the parentless-maximal spheres are assigned the same pore label and given to a region growing algorithm, which segments all of the voxels in the original three-dimensional image into pore regions. The surface between regions is the throat surface, outlined by the pink dashed line in (c). In (d), the region extraction process is shown for a synthetic pore geometry which is used Chapter 3 of this study.

Intuitively, some inscribed spheres will be completely overlapped by larger, neighbouring spheres, while others – the maximal spheres – will be only partially overlapped. The surface connecting the centres of all maximal spheres is the medial surface of the pore space (Fig. 2.1b). While still a computationally demanding task, many efficient algorithms have been proposed for extracting the medial surface from an image, and the extraction can be run in parallel, meaning that images in excess of 2000^3 can be processed on standard workstations.

The maximal spheres defining the medial surface are then subject to a parent-child hierarchy, as in *Dong and Blunt* (2009). For each pair of partially overlapping maximal spheres, the larger sphere is considered as the parent. A maximal sphere with no parent is, locally, the largest sphere, whose radius and centre represent a pore radius and centre, respectively (Fig. 2.1b). The parentless sphere is given a pore label, and all of its children inherit the same pore label: the parent-child hierarchy is used to determine the pore radii, the pore centres and to group the voxels on the medial surface into pore regions.

The remaining void-space voxels of the image are assigned a pore label via a region-growing algorithm (Fig. 2.1c). The algorithm begins with the medial surface voxels already assigned to a pore region, and iteratively assigns the same pore label to neighbouring voxels (Fig. 2.1c). The result is analogous to a watershed segmentation of the pore space. Each set of voxel faces between two different pore-labels corresponds to a throat surface (Fig. 2.1c). The radius of the throat is calculated as the average of the maximal spheres adjacent to the throat surface. The overall outcome of the pore-region extraction stage applied to a synthetic voxel image, which is used in Chapter 3 of this thesis, is shown in Fig. 2.1d.

2.2.2 Corner Extraction and Description

In the generalised network model, pores do not comprise the essential elements of the network. Instead, the pore regions identified in the previous section are further divided into corners (Fig. 1.8D).

The medial axis of a two-dimensional shape is a set of points defining a one-dimensional medial curve. To generate corners, the throat surfaces identified in section 2.2.1 have their medial curves extracted in a similar fashion to the medial surface of the pore space: on each

throat surface, the distance map is used to generate a collection of non-overlapping maximal spheres (Fig. 2.2a). The curve which joins the centres of these spheres defines the medial axis of the throat surface. Each branch of this medial axis is given a corner label, and defines the sagittal plane (Fig. 1.8I) of that corner.

Subsequently, the corner labels are given to another region-growing algorithm: beginning with the voxels defining a throat surface's medial axis curves, the corner labels are iteratively assigned – in all directions – to neighbouring unassigned voxels in the original image. The overall result is that each void-space voxel in the image belongs to a unique corner (Fig. 2.1b). All corners sharing the same throat surface form a complete throat, which includes all voxels between two neighbouring pores. The overall outcome of the corner-extraction stage applied to a synthetic voxel image, which is used in Chapter 3 of this thesis, is shown in Fig. 2.2c.

The geometry of each corner at the throat surface and at the adjacent pore centres, in the axial plane (Fig. 1.8e), is described by its half angle, γ, its perimeter, H, and the radius of the throat (R_t) or pore (R_p) maximal sphere. The cross-sectional areas in the axial planes are obtained directly from the underlying image. In the sagittal plane, edge vectors ($\mathbf{e}$) are defined, which connect the corner vertices at the throat surface to the corner vertices at the adjacent pores. These edge vectors preserve a three-dimensional description of the expansion and contraction of the pore space in the sagittal plane, as explained in Chapter 1 and in Fig. 1.8l. A sagittal description of the pore space is novel among pore-network models, and will be exploited in Chapter 3 to improve the calculation of interfacial curvature.

In summary, the base elements of the GNM are the corners. The corners combine to form complete throats, each accounting for all void-space voxels between two neighbouring pores. The corners preserve a thorough description of the pore space in both the axial and sagittal planes. In the next section, displacement through this network of corners is described.

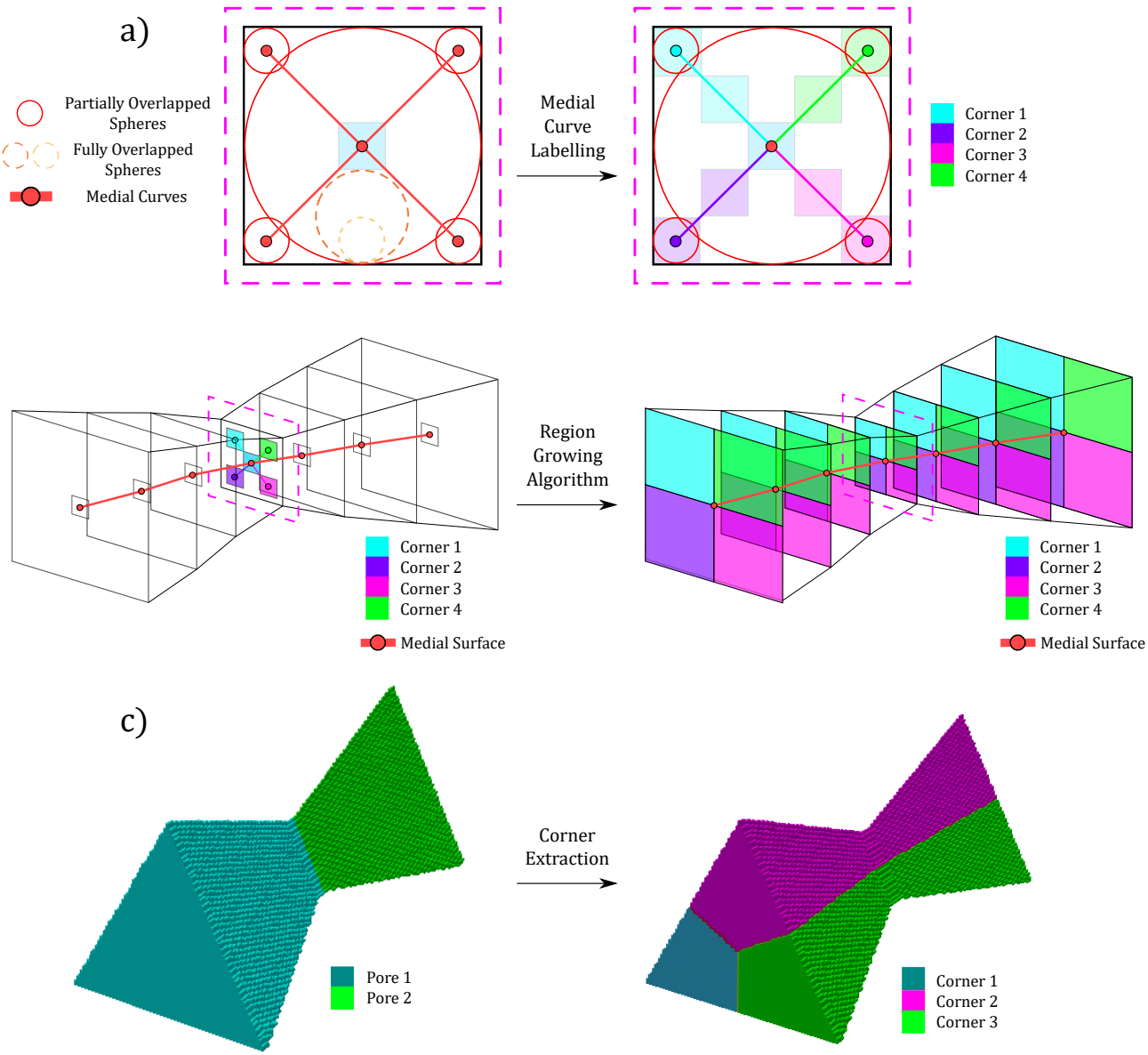

Figure 2.2: An illustration of the second stage of generalized network extraction. The throat surface from Fig. 2.1c is shown in (a). The distance map of the throat surface can be visualised as a collection of spheres – the line connecting the centres of partially overlapping spheres defines the medial curve of the throat surface. Each unique branch of the medial curve is assigned a corner label. In (b), the corner labels are given to a region growing algorithm, which segments all voxels in the underlying three-dimensional image into corners. In (c), the corner extraction process is shown for the synthetic pore geometry shown in Fig. 2.1d, which is used in Chapter 3 of this study.

2.3 Generalized Network Quasi-Static Two-Phase Flow Simulation

Fundamentally, simulating flow through the GNM is no different to any other quasi-static network model: the capillary pressure is incremented and interfaces are moved to new positions of equilibrium, with each phase's permeability determined from its configuration at equilibrium. Here, the description of flow simulation is separated into three parts. First, the description of interfaces at equilibrium is presented. Second, displacement of these interfaces is explained. Finally, the calculation of permeability is described.

2.3.1 Equilibrium Configurations

Every corner in the network has a local coordinate system (x, y). The x-coordinate represents the distance, in the sagittal plane, along the pore-space medial axis between the throat centre and the pore centre. The y-coordinate is the distance, in the axial plane, between the pore-space medial axis and the corner's vertex. At an imposed capillary pressure, the corner's geometric properties (volume, area, perimeter, radius and half angle) and the coordinate system allow a complete description of piston-like and layer interfaces.

Piston-like Interfaces

Raeini et al. (2018) proposed the following description of piston-like interfaces in the GNM. Here, a complete derivation is presented, as in *Giudici et al.* (2023a).

Figure 2.3 shows a schematic of a square capillary tube which contracts into the page at an angle β. In the axial plane, shown by Fig. 2.3a, the generalised network extraction discretises the square into four corners, shown by the magenta lines defining the coronal planes (Fig. 2.3b) of the pore space. In addition, every corner has a sagittal plane (Fig. 2.3c), shown by the diagonal blue lines (the medial curves) in Fig. 2.3a. As a whole, the axial, coronal and sagittal planes retain a three-dimensional description of the pore space used to derive a general equation for piston-like curvature.

Consider the axial plane shown in Fig. 2.3a. Wetting layers are present in each corner, with

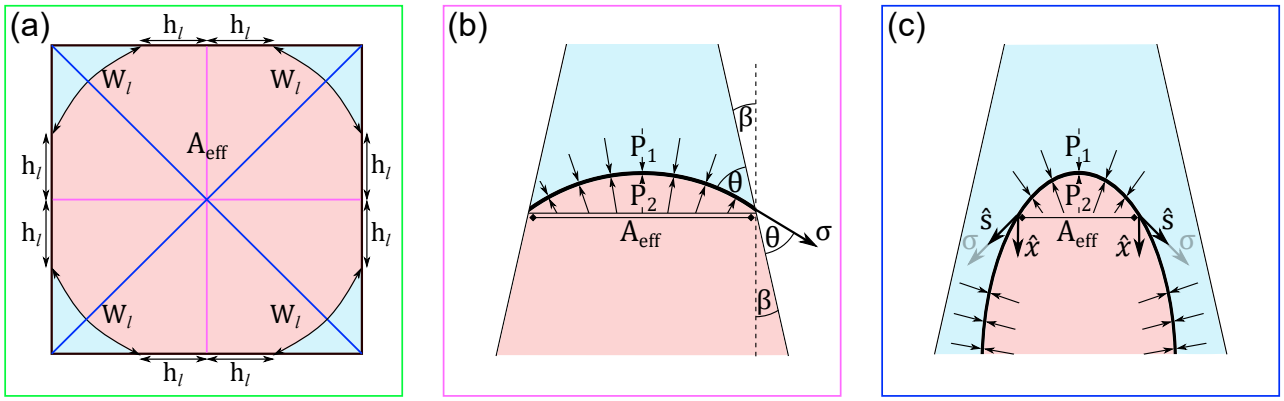

Figure 2.3: A schematic showing a piston-like interface in a square capillary — which contracts into the page — in the axial (a, green), coronal (b, magenta) and sagittal (c, blue) planes. The piston-like curvature can be derived using a force balance on the interface, where P_1 and P_2 are the receding and invading phase fluid pressures, respectively, β is the expansion angle, θ the contact angle through phase 1, and σ the interfacial tension. The length of the layer interface and invading phase-solid contact length, in each corner, is denoted by W_l and h_l, respectively, while A_{eff} is the effective area of the fluid-fluid interface after it is projected onto the axial plane. In the sagittal plane, an interface tangent vector $\hat{\mathbf{s}}$, is used to determine the component of interfacial tension acting in the vertical direction, given by the vector $\hat{\mathbf{x}}$.

a layer interfacial length denoted by W_l. The red, invading phase occupies an effective area of the square, A_{eff}, which contacts the solid perimeter of the square at a length $2h_l$ in every corner.

The fluid-fluid interface is subject to a pressure from the invading and receding phases, shown in the coronal and sagittal planes (Figs 2.3b and c) by P_2 and P_1, which acts everywhere normal to the interface. The resulting vertical force from P_1 and P_2 is obtained by projecting the total area of the interface onto the axial plane (A_{eff} in Fig. 2.3a) and multiplying by the difference in pressure. Additionally, the fluid interface experiences a force from the interfacial tension, σ, acting per unit length along its perimeter and tangent to the interface. Where the invading phase contacts the solid, the interfacial tension acts at an angle $\theta + \beta$ to the vertical (Fig. 2.3b), with θ representing the contact angle. At the layer interfaces, the vector $\hat{\mathbf{s}}$ is tangent to the interface and represents the direction of σ, while $\hat{\mathbf{x}}$ is the direction of the vertical (Fig. 2.3c).

At equilibrium, the sum of forces must balance. Performing a vertical force balance:

$$P_2 A_{eff} = P_1 A_{eff} + \sigma 8 h_l \cos(\theta + \beta) + \sigma 4 W_l \hat{\mathbf{s}} \cdot \hat{\mathbf{x}},$$
$$P_2 - P_1 = P_c = \frac{\sigma (8 h_l \cos(\theta + \beta) + 4 W_l \hat{\mathbf{s}} \cdot \hat{\mathbf{x}})}{A_{eff}}. \tag{2.1}$$

Dividing by σ and noting that A_{eff} is given by the difference between the total square and layer area gives an expression for piston-like curvature in the square system. To generalise Eq. 2.1, a summation over every corner belonging to a network element, t, is introduced, where each corner exhibits a fluid-solid length of $2h_l$ and a layer interface length (if present) of W_l, giving:

$$\kappa_{pl} = \frac{\sum_{c \in t} (2 h_l \cos(\theta + \beta) + W_l \hat{\mathbf{s}} \cdot \hat{\mathbf{x}})}{A_{total} - A_{layer}}. \tag{2.2}$$

Equation 2.2 is explicitly determined at three fractional distances from throat centre to pore centre: $x = \{0, \frac{1}{2}, 1\}$, while the calculated curvatures are assumed to change linearly between each distance. For any imposed capillary pressure, Eq. 2.2 determines the position of equilibrium of a piston-like interface in the network. In Chapter 3, an empirical equation for determining β is provided, alongside and assessment of the impact that β on pore-scale displacement.

Layer Configurations

In the axial plane, the position of an oil or water layer, for any imposed curvature (capillary pressure), is easily obtained. Consider a corner with half angle γ, shown by the axial plane in Fig. 2.4. If the invading phase, shown in red, has a contact angle θ which satisfies $\theta + \gamma < \frac{\pi}{2}$, then a wetting layer will form after a piston-like interface has displaced through the centre. The length of the layer-solid contact in the axial plane is denoted by L_l. Using simple geometry, the following expression for the axial radius of curvature, r_a, at any L_l, can be derived (*Blunt*, 2017):

$$\frac{1}{r_a} = \frac{\cos\theta (\cot\gamma - \tan\theta)}{L_l}. \tag{2.3}$$

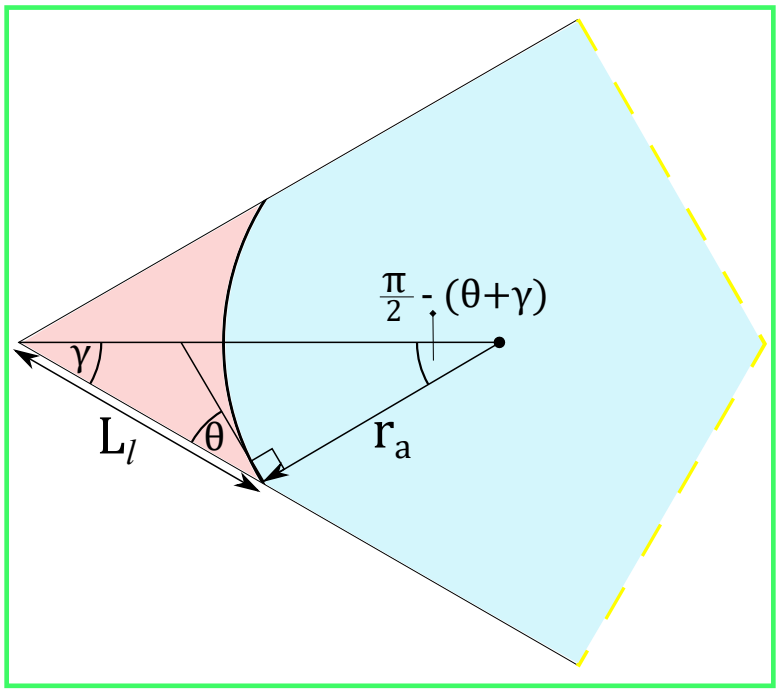

Figure 2.4: A diagram showing a geometric method to determine the radius of axial curvature, r_a, using the layer-solid and centre-solid lengths, L_l and L_c, the corner angle γ and the contact angle measured through the layer, θ.

Strictly, the imposed capillary pressure is described by the sum of two principal curvature components (Eq. 1.9). To date, few network models have considered the curvature of a layer in its sagittal plane. In Chapter 3, the geometry of the GNM will be exploited to produce a new method for including sagittal curvature in network modelling. The impact that sagittal curvature has on predictions will be quantified.

2.3.2 Fluid Displacements

Displacements are driven by incrementally increasing the invading phase pressure at the inlet. The existing interfaces are updated in accordance with capillary equilibrium: for each interface, if the new capillary pressure exceeds a threshold value, the interface will displace to a new equilibrium position. The three-phase contact loop of an interface can remain pinned, with only a change in interfacial curvature, if the new capillary pressure does not cause the interface to reach its (user defined) advancing or receding contact angle. The threshold capillary pressure necessary to elicit a displacement depends on the local fluid configuration and is different for pores and throats.

At a throat, the possible displacements are piston-like advance or snap-off. Piston-like advance occurs when the prevailing capillary pressure exceeds the threshold predicted by Eq. 2.2, while snap-off occurs when the three-phase contact point of two layers meet in the axial plane (Fig. 2.4).

At a pore, piston-like displacement or cooperative pore-body filling are possible. To recap, the elements of the generalized network model are corners, which combine to form complete throats between two adjacent pore centres. Pores are simply the region of intersection, or the union, of many throat elements. The threshold pressure to invade a pore is determined from its constituent throat elements and considers the local fluid configuration. The pore entry pressure is defined as the largest capillary pressure given by Eq. 2.2 when applied to the connecting throats which contain the invading phase in a piston-like configuration. In other words, for each throat element forming a given pore, Eq. 2.2 is applied if that throat element contains the invading phase in a piston-like configuration, and the maximum predicted pressure out of all the connecting throats is considered to be the threshold entry pressure for that pore. For pore threshold pressures, Eq. 2.2 is applied at fractional distances of $x = \{\frac{1}{2}, 1\}$: in each connecting throat considered, the displacement pressure is determined at the pore centre and halfway between the pore and throat centres.

Interestingly, the GNM is the only network model which explicitly models cooperative pore-filling through a force balance rather than empirical approximations: Eq. 2.2 directly considers the effect of adjacent occupied throats through the interface tangent vector $\hat{\mathbf{s}}$. Cooperative pore-body filling is not a focus of this thesis and the reader is referred to *Raeini et al.* (2018) for a thorough treatment, however a conceptual view is provided here for completeness.

Programmatically, each corner element within a throat retains the position in memory of its neighbouring corners belonging to different, adjacent throats. Throughout the simulations, a corner element can therefore check its neighbouring corners' fluid configurations. When determining the entry threshold capillary pressure for a given pore, Eq. 2.2 is applied to each connecting throat, and the equation itself loops over all of the corners forming the considered throat, as explained previously. At the halfway point, $x = \frac{1}{2}$, the interface tangent vector is considered to always be parallel to the edge vector, $\mathbf{e}_1$, between the throat-centre and

pore-centre of the considered corner (Fig. 2.5).

However, at the pore centres ($x = 1$), the interface tangent vector can vary. If a corner under consideration detects that its neighbour has a layer-like configuration of the invading phase, then the direction of the interface tangent vector is set to be the difference between the edge vectors of the two corners, shown in Fig. 2.5a. Alternatively, if a corner detects that its neighbour is in a piston-like configuration, as shown in Fig. 2.5b, the tangent vector is assumed equal to the throat-centre to pore-centre line, $\hat{\mathbf{x}}$. In this way, the dot product $\hat{\mathbf{s}} \cdot \hat{\mathbf{x}}$ in Eq. 2.2 directly accounts for local fluid configurations — adjacent throats which are filled with the invading phase increase the cumulative dot product, which results in larger, more favourable pore entry pressures, consistent with cooperative pore filling.

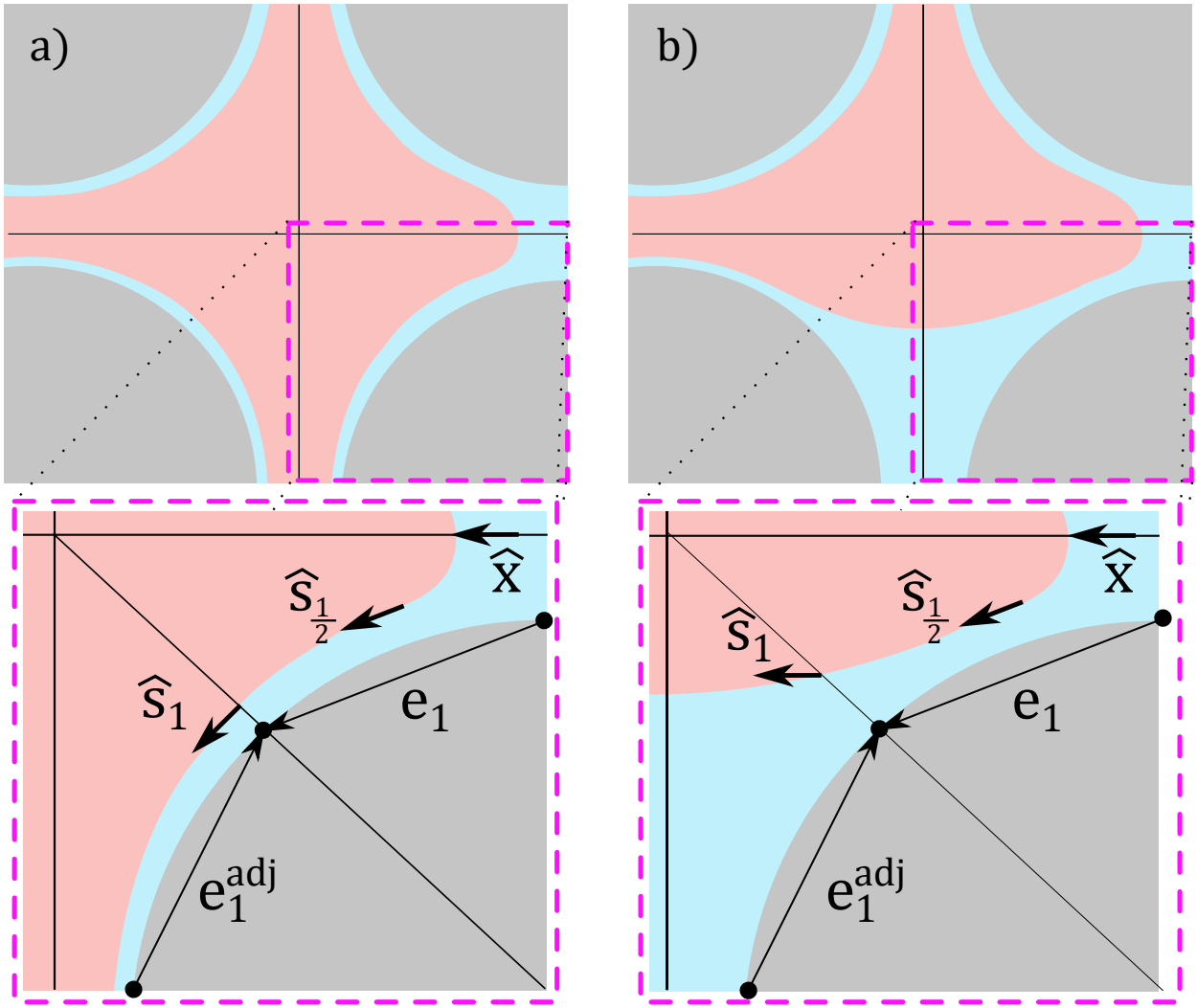

Figure 2.5: A schematic of the generalised network model's treatment of cooperative pore-body filling. The blue, invading phase is displacing into the pore from the rightmost throat. The top row shows two different local fluid configurations, while the lower row shows a zoomed in perspective of the two adjacent corners outlined in pink. In (a), the adjacent corner is in a layer-like configuration, and the interface tangent vector at the pore centre ($\hat{s}_1$) is assumed to have a direction equal to the difference in the edge vectors: $\hat{s}_1 = \frac{e_1 - e_1^{adj}}{|e_1 - e_1^{adj}|}$. However, if the adjacent corner has a piston-like configuration of the invading phase, shown in (b), the interface tangent vector is assumed equal to the unit vector between the throat and pore centre ($\hat{x}$). At the halfway point, the tangent vector always has a direction equal to the corner's edge vector, given by $\hat{s}_{\frac{1}{2}} = \hat{e}_1$.

2.3.3 Relative Permeability Calculation

After each pressure increment, the new interface positions are used to update the saturation of each phase. After a user-defined change in network saturation, the conductivity of the corners comprising each throat are calculated and averaged to provide the conductivity of that throat. Subsequently, mass balance on each pore, p, is invoked to calculate the flow rate:

$$\sum_{t \in p} q_t^\alpha = \sum_{t \in p} g_t^\alpha \left(\Phi_p - \Phi_{nei}\right) = 0 \tag{2.4}$$

where q_t^α is the total flow rate of a phase (α) passing through a throat (t), g_t^α is the throat conductivity and $\Phi_p - \Phi_{nei}$ is the viscous pressure drop between neighbouring pores. The summation is over all throats connected to a given pore. Equation 2.4 leads to a sparse system of linear equations, which can be solved numerically after a dimensionless pressure of 1 and 0 are set at the inlet and outlet, respectively. The total flow rate into (or out of) the network is the sum of the flow rates entering (or exiting) the inlet or outlet side of the domain. Finally, the relative permeability of each phase is obtained by dividing its total flow rate by the single-phase flow rate, which is calculated before flow simulations begin.

2.4 Advantages over Classical Approaches

A key advantage that the GNM has over classical approaches is the absence of many ambiguous parameters. In classical methods, pores and throats are separate entities, each with their own volume and length (*Valvatne and Blunt*, 2004). These volumes and lengths are then used to calculate the single, two-phase and electrical permeability. In reality, however, there is no physical boundary between a pore and a throat; assigning geometric properties to these fictitious conceptualisations of the pore space becomes arbitrary.

In the GNM, the network elements are conceptually corners, which combine to form throats: a generalized throat includes all of the voxels between two neighbouring pore centres, as explained in Section 2.2.2. A pore is simply the combination of many half throats. The geometric description of generalized throats is obtained directly from the underlying image, eliminating the need for decision-making.

The cross-sectional shape of the generalized elements in the axial and sagittal planes (Fig. 1.8) – the latter of which is a central part of this thesis – further benefit from the generalized discretisation. As explained in Fig. 1.8k, classical methods do not consider the sagittal plane, which has been shown to impact two-phase flow, while the axial plane is described by a simplified shape with a non-unique equivalent shape factor. Changing the shape of the pore space will clearly affect the number of corners, the formation of layers in the corners, and the connectivity throughout the medium. These features have substantial impact on the displacement capillary pressure and the conductivity of the network elements. The GNM effectively removes these inaccuracies.

While the generalized extraction provides a more accurate characterisation of the pore space in three dimensions, little research has focused on the impact that the third spatial – or sagittal – dimension has on displacement. Additionally, within the context of network modelling, few attempts have been made to incorporate any three-dimensional effects into a network-modelling framework. In the next chapter, a comprehensive assessment of the impact that the sagittal plane has on piston-like and layer displacement is presented, and the generalized network model is further developed to accurately predict the observed behaviour.

CHAPTER 3

REPRESENTATION OF FULLY THREE-DIMENSIONAL INTERFACIAL CURVATURE IN PORE-NETWORK MODELS

The contents of this chapter have been published in Giudici et al. (2023a).

3.1 Overview

In this chapter, the detailed geometry of the GNM is exploited to formulate the inclusion of pore-space expansion, β, and the sagittal curvature, κ_s, of a fluid-fluid meniscus. To do this accurately, high resolution direct simulations of two-phase flow through a variety of synthetic geometries and wettabilities, performed with a volume-of-fluid method, are used to calibrate GNM developments. The effect of pore-space expansion and sagittal curvature on threshold pressures for displacement events are quantified from the volume-of-fluid simulations and compared to both generalised, and classical, network model predictions. A pressure dependence of sagittal curvature is revealed, with direct simulations used to further develop and calibrate pore-by-pore inclusion of three-dimensional effects into the generalised network model. Finally, the impact of physically accurate fluid interfaces on macroscopic two-phase flow parameters is demonstrated through a comparison with experimental results. Overall, this chapter produces a pore-network model that accurately captures the full three-dimensional nature of fluid displacement, validated by direct pore-scale numerical simulation.

3.2 Network Model Developments

In this section, the developments to the generalised network model are explained. First, the inclusion of pore-space expansion is presented, followed by a new method for incorporating

the sagittal curvature of a layer interface.

3.2.1 Curvature for Piston-like Advance

Traditionally, the curvature of a piston-like (terminal) meniscus has been determined by considering an energy balance on the layer interfaces, termed arc-menisci, present in the corners of the pore space (Fig. 1.8g). This is a two-dimensional calculation which ignores curvature in the sagittal plane. With complex geometry the energy balance is algebraically elaborate to simplify, but the key result is that the total curvature is related to the ratio of the effective perimeter (P_{eff}) and area (A_{eff}) occupied by the invading phase, given by $\kappa = \frac{P_{eff}}{A_{eff}} \cos\theta$, where θ is the advancing or receding contact angle (*Mason and Morrow*, 1991). For classical networks — which use a shape factor, $G = \frac{A}{P^2}$, to represent the ratio of the total area (A) to the total perimeter (P) — the curvature of a piston like interface, κ_{pl}, is given by:

$$\kappa_{pl} = \frac{\cos\theta\left(1 + 2\sqrt{\pi G}\right)}{r} F_d\left(\theta, G, \gamma\right), \tag{3.1}$$

where F_d is a dimensionless correction factor accounting for the wetting layers retained in the corners, r is the inscribed radius of the element and γ represents the corner half-angles (*Blunt*, 2017).

While Eq. 3.1 accounts for the effect of wetting layers on terminal meniscus curvature, and ensures capillary equilibrium between layer and piston-like interfaces, it does not include the three-dimensional effect that an expanding or contracting pore space has on the total curvature — Eq. 3.1 is obtained purely from the axial plane shown in Fig. 1.8g. Pore-space expansion has been shown to have considerable influence on entry pressures, particularly at neutral wettabilities with contact angles close to $90°$ (*Rabbani et al.*, 2018). Therefore, if network models are to be truly predictive, they must include the expansion angle β, shown in Fig. 1.8l. As discussed in the previous section, the GNM does include β in its approximation of piston-like curvature (Eq. 2.2). Below, a new method for determining β is presented.

Consider Fig. 3.1, which shows a pore and two possible connectivity scenarios, with a piston-like interface present in the left-most throat. As the pressure of the red, invading phase

increases, the fluid-fluid interface will displace into the pore centre with a curvature given by Eq. 2.2. However, the angle β is not necessarily constant — it can vary depending on the exact geometry and topology of the local pore space. Two vectors are defined, $\mathbf{p}$ and $\mathbf{t}$, which point from the occupied throat centre to the pore centre and the adjacent throat centre, respectively. The vectors $\mathbf{p}$ and $\mathbf{t}$ are used to produce an empirical expression to approximate β, in every corner, at three locations: $x_{pl} = \{0, \frac{1}{2}, 1\}$, where x_{pl} is the fractional distance from throat centre to pore centre. The empirical expression approximates the solid wall as sinusoidal and accounts for connected throats:

$$\beta = \tan^{-1}\left(\frac{a\sin\left(\pi x_{pl}\right)\left(r_p - r_t\right)}{D}\right) + b\sin\left(\frac{\pi}{2}x_{pl}\right)\cos^{-1}\left(\frac{\mathbf{t}\cdot\mathbf{p}}{\|\mathbf{t}\|\,\|\mathbf{p}\|}\right), \tag{3.2}$$

where r_p and r_t are the pore and throat radii, respectively, and D is the distance between pore centre and throat centre. The coefficients a and b are sensitivity parameters and are set to 0.3 and 1.1 in this work, respectively: the reader is referred to Fig. A.1 for further details on how these values are determined. If a corner's neighbouring throat is situated exactly opposite the current throat, shown schematically by Fig. 3.1a and in cross-section by Fig. 3.1c, the dot product of $\mathbf{p}$ and $\mathbf{t}$ is zero and Eq. 3.2 reduces to the first term — a simple trigonometric expression modulated by the sine function. However, if other adjacent throats are present (Fig. 3.1b), the second term in Eq. 3.2 accounts for additional expansion shown in Fig. 3.1d, where the expansion angle β is greatest at the pore-centre.

In section 3.5.1 of this chapter, the performance of Eq. 3.2 is evaluated against volume-of-fluid simulations of piston-like advance through a wide range of wettabilities. The volume of fluid simulations will be explained further in Section 3.4.1.

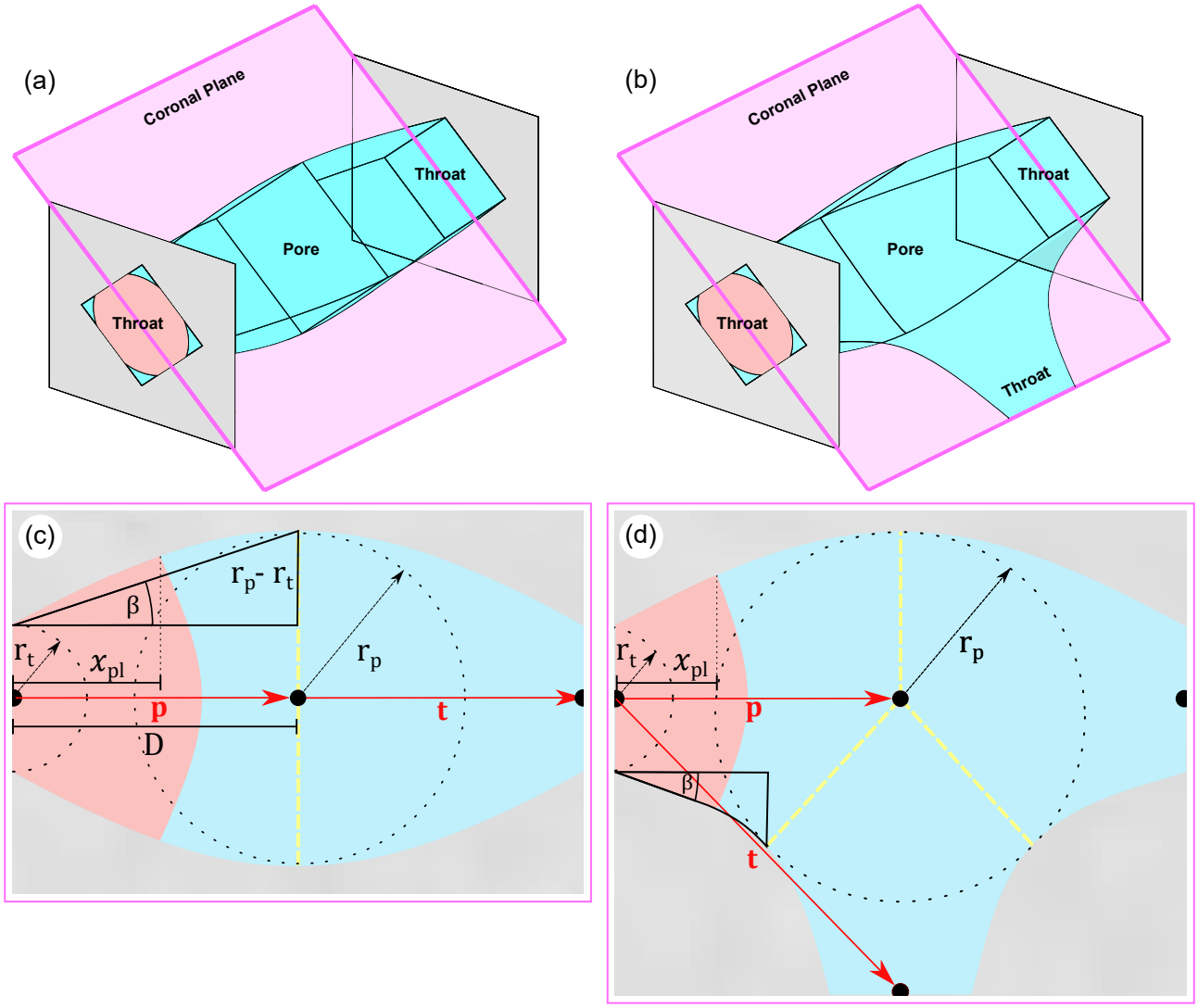

Figure 3.1: A schematic showing the parameters used to determine the expansion angle, β, at which the solid is inclined to the line connecting throat and pore centre. In a pore-throat arrangement where the throats are exactly opposite one another, as shown in (a), β is determined using the difference in pore (r_p) and throat (r_t) radii, as well as the pore-throat distance, D, which are shown in the coronal-plane cross-section in (c). However, if the throats connecting to a pore are not opposite each other — shown schematically in (b) — it is assumed that β will take a maximum value at the pore-centre and an additional correction must be included. The correction uses the dot product of the vectors connecting the throat to the pore centre (p) and to the adjacent throat centre (t), shown in the coronal-plane cross-section in (d). In both cases, the solid wall is modelled as sinusoidal, and estimates are taken at a distance $x_{pl} = \{0, \frac{1}{2}, 1\}$, where x_{pl} is the fractional distance from pore to throat.

3.2.2 Layer Sagittal Curvature

The total fluid-fluid curvature present in Eq. 1.9 represents the sum of the principal components of curvature, κ_a and κ_s, of the interface:

$$\kappa = \kappa_a + \kappa_s. \tag{3.3}$$

For piston-like interfaces, κ can be determined from a force balance on the interface, as previously shown in Eq. 2.2. For layer configurations, however, a force balance becomes more complex. Therefore, it is typical in network modelling to assume that the second principal component of curvature — termed here as the sagittal curvature (κ_s) — is negligible, and so the total curvature is equal to the curvature in the axial plane, $\kappa = \kappa_a$. Strictly speaking, this assumption is only valid for a system which can be approximated as infinitely long and radially invariant, such as a capillary tube of constant radius (*Lenormand et al.*, 1983). As discussed previously, many studies have noted that, in truly three-dimensional geometries, curvature in the sagittal plane affects capillary pressure predictions (e.g, *Deng et al.*, 2014; *Raeini et al.*, 2014). To date, however, only one network model has attempted to include sagittal curvature (*Raeini et al.*, 2018) in a truly three-dimensional context. Below, a new approach for incorporating sagittal curvature into a network model on a pore-by-pore basis is provided.

Consider Fig. 3.2, which schematically shows the sagittal plane (Fig. 1.8i) of a throat (a) and a pore (b). It is evident from Fig. 3.2 that the curvature of the wetting layers in the sagittal plane is not zero. To approximate it, the corner vertices at every throat centre are assumed to be a local origin, O. Then, a set of vectors are defined dependent upon whether the sagittal curvature at a throat or pore is to be calculated. At a throat centre, two edge vectors between the throat corner vertices and the neighbouring pore corner vertices, $\mathbf{e_1}$ and $\mathbf{e_2}$, are defined (Fig. 3.2a). Provided that O, $\mathbf{e_1}$ and $\mathbf{e_2}$ are non-colinear, these three points are sufficient to define a unique circle with radius r_{st} in the sagittal plane. The centre of this circle, $\mathbf{C_{st}}$, is determined from the intersection of the vectors normal to $\mathbf{e_1}$ and $\mathbf{e_2}$. Subsequently, the sagittal curvature at the throat, κ_{st}, is assumed to be inversely proportional to r_{st} — which is

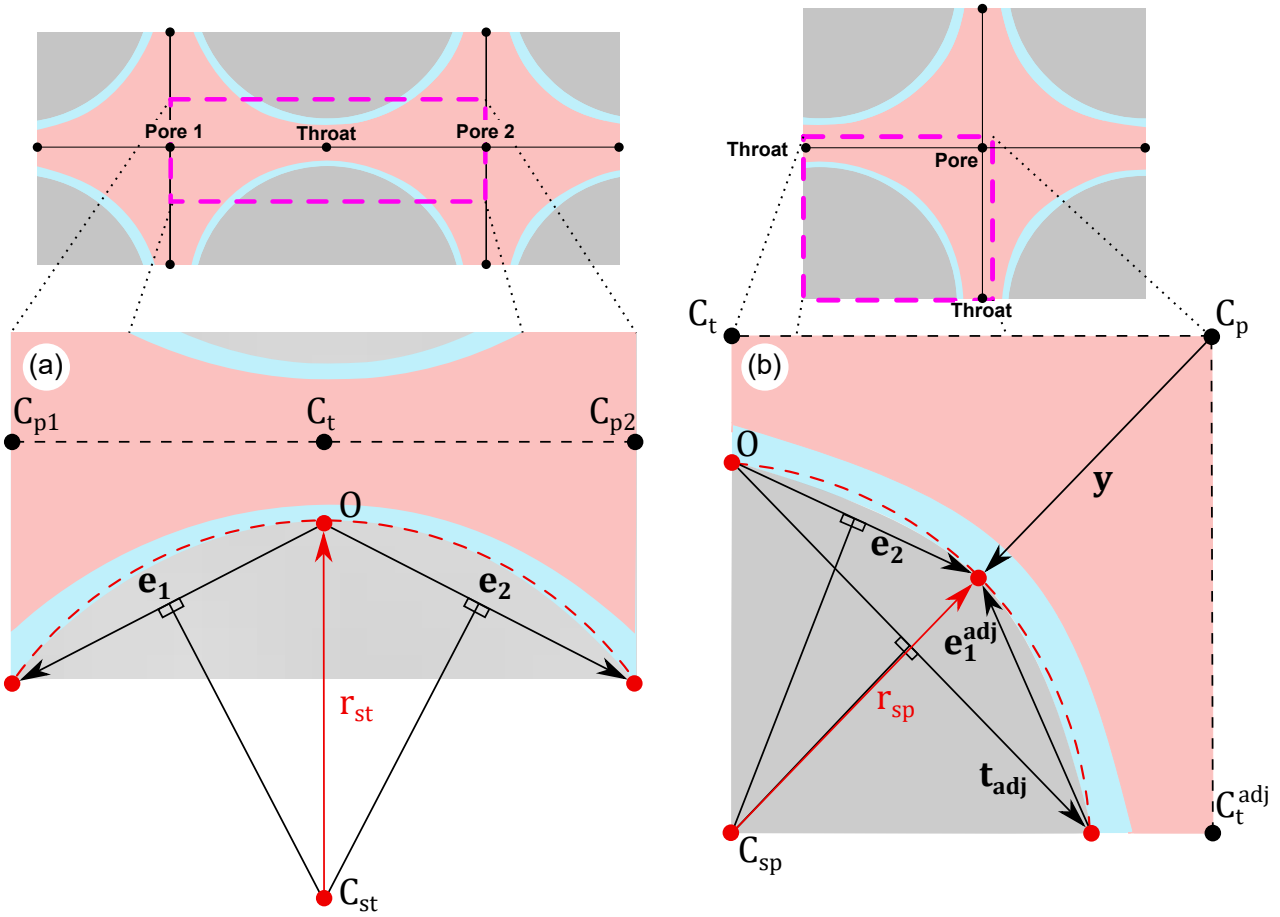

Figure 3.2: A schematic showing the method used to determine the radius of sagittal curvature, r_s, of a layer at a throat (a) and at a pore (b). In (a), the radius of sagittal curvature at the throat (r_{st}) is defined using the circle formed by the throat corner, O, and the two edge vectors $\mathbf{e_1}$ and $\mathbf{e_2}$, which are the position vectors of the neighbouring throat corners relative to O. In (b), the radius of sagittal curvature at the pore (r_{sp}) is obtained from the circle defined by O, $\mathbf{e_2}$ and the position vector of the neighbouring throat corner, $\mathbf{t_{adj}}$, relative to O. In addition, the sign of r_{sp} is determined by the dot product of the sum of the adjacent throat's edge vector, $\mathbf{e_1^{adj}}$, and $\mathbf{e_2}$ with the pore-centre to pore-corner axis, $\mathbf{y}$.

calculated as the distance between the throat corner vertex and $\mathbf{C_{st}}$ — and is always negative:

$$\kappa_{st} = -\frac{c}{r_{st}} = -\frac{c}{|\mathbf{C_{st}}|}. \tag{3.4}$$

For pore centres, the edge vector $\mathbf{e_2}$ and the vector between adjacent throat corner vertices, $\mathbf{t_{adj}}$, establish the three points needed to determine the circle defining the pore sagittal curvature, which has a radius r_{sp} and centre $\mathbf{C_{sp}}$ (Fig. 3.2b). Additionally, the adjacent throat's edge vector, $\mathbf{e_1^{adj}}$, and the pore-centre to pore-corner axis, $\mathbf{y}$, are needed to determine the sign of the pore sagittal curvature:

$$\kappa_{sp} = \begin{cases} \frac{d}{r_{sp}} = \frac{d}{|\mathbf{C_{sp}}|}, & \text{if } \left(\hat{\mathbf{e}}_\mathbf{2} + \hat{\mathbf{e}}_\mathbf{1}^\mathbf{adj}\right) \cdot \hat{\mathbf{y}} > \mathbf{0} \\ -\frac{d}{r_{sp}} = -\frac{d}{|\mathbf{C_{sp}}|}, & \text{otherwise.} \end{cases} \tag{3.5}$$

The generalised network represents a coarse-scale discretisation of the porous medium, from which only a finite set of vertices may be used to calculate sagittal curvature. In reality, curvature is mathematically defined at an infinitesimal portion of a fluid interface (*Blunt*, 2017). The coefficients c and d in Eqs. 3.4 and 3.5 therefore represent calibration factors which account for the coarse discretisation in the GNM, and are used to optimise the approximation of sagittal curvature.

Equations 3.4 and 3.5 are used to define the sagittal curvature at every pore and throat centre of each corner in the network, prior to initiating fluid injection. In the following section, the direct numerical simulation method used to assess and calibrate Eqs. 3.2, 3.4 and 3.5 is explained.

3.3 Volume of Fluid Method

The essential details of the direct method used to calibrate the network model developments are outlined here — for a complete treatment the reader is referred to *Raeini et al.* (2012) and *Shams et al.* (2018). All differential equations that follow are solved using the OpenFOAM finite volume library (*Jasak et al.*, 2007).

The flow of two isothermal, incompressible and immiscible Newtonian fluids is described by the set of Navier-Stokes equations:

$$\nabla \cdot \mathbf{u} = 0 \tag{3.6}$$

$$\frac{D}{Dt}(\rho \mathbf{u}) - \nabla \cdot \mathbb{T} = -\nabla p + \mathbf{F} + \mathbf{f}_c. \tag{3.7}$$

The velocity field, $\mathbf{u}$, is updated based upon the pressure gradient, ∇p, the body forces acting on the fluid, $\mathbf{F}$, and the capillary force, $\mathbf{f}_c$, which is determined through the contour-level surface force model (*Shams et al.*, 2018). The viscous stress tensor is denoted as $\mathbb{T} = \mu\left(\nabla \mathbf{u} + (\nabla \mathbf{u})^T\right)$, where μ is the dynamic viscosity.

The two fluids are treated as a single fluid-continuum system, with an indicator function, α defined throughout the flow domain representing the volume fraction of the phases in each grid cell. The indicator function is a continuous variable $\alpha = [0, 1]$, taking a value $\alpha = 1$ if the cell is completely filled with phase 1 and a value $\alpha = 0$ if the cell is filled with phase 2. Values between zero and one are present in cells containing the fluid-fluid interface, which is tracked and evolved using the advection equation:

$$\frac{\partial \alpha}{\partial t} + \nabla \cdot (\alpha \mathbf{u}) = 0. \tag{3.8}$$

The density and viscosity of the fluids is 1000 kgm^{-3} and 0.001 Pas, respectively. All simulations are capillary dominated, with a capillary number, $C_a = \frac{\mu q}{\sigma}$, of 6.67×10^{-6} for the injected phase, where q represents the Darcy velocity. The contour-level surface force model used in this work significantly enhances the accuracy of capillary pressure predictions (*Shams et al.*, 2018). The mesh discretising the flow domain is unstructured, with cubic grid blocks in the centre and grid blocks deformed to align with the solid walls at the boundaries. The resolution is $1\,\mu$m per grid block, with an extra layer of cells added near the solid walls to more accurately capture wetting layers.

The volume-of-fluid method is used to simulate piston-like advance and layer growth in synthetic geometries, with the predictions compared to those obtained with network modelling.

The following section describes the geometries, flow conditions and methods used to compare and validate the network model developments presented in section 3.2 with volume-of-fluid simulation predictions.

3.4 Synthetic Geometries, Flow Conditions and Comparison

The geometry — and related flow conditions — considered depend upon the local property being analysed. Below, the properties of interest are separated and their respective flow conditions and points of comparison are described.

3.4.1 Piston-Like Curvature Analysis

To analyse piston-like curvature, a synthetic two pore system is constructed using intersecting spheres. To save time, the symmetry of the system is exploited by a lengthways bisection. The synthetic geometry and its dimensions are shown in Fig. 3.3.

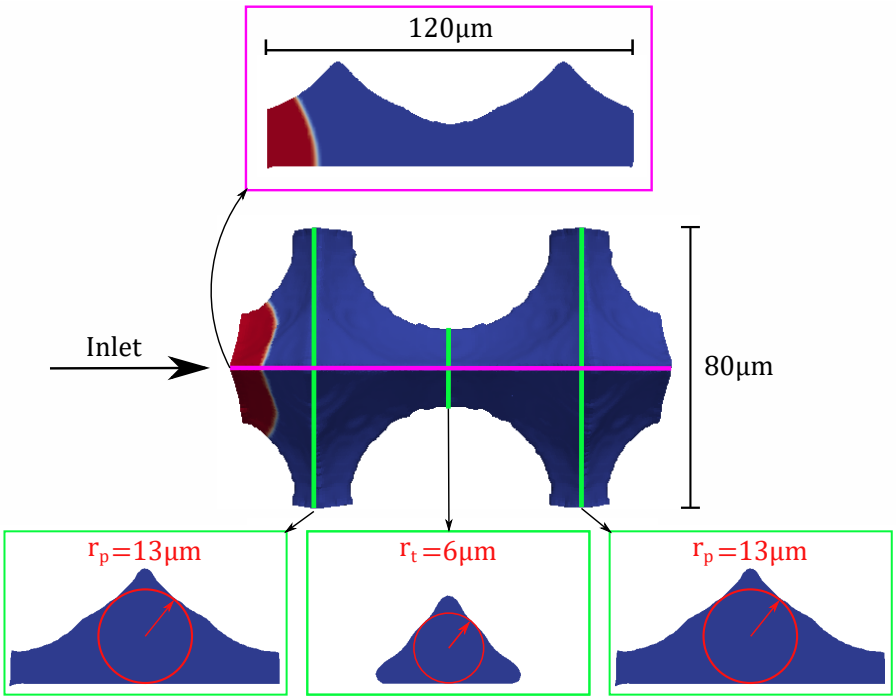

Figure 3.3: The dimensions of the synthetic two-pore geometry used in the analysis of piston-like curvature. The magenta line represents a sagittal plane of the system, shown in cross-section in the top of the figure, while the green lines show axial planes at the pore and throat centres, shown in cross-section at the bottom of the figure. The pore and throat radii are denoted by r_p and r_t, respectively. The two-pore system is initialised with a 5% saturation of invading (red) fluid before injection commences.

Using the volume-of-fluid method, a piston-like interface is initialised at the inlet side of the two-pore system, corresponding to an initial invading fluid saturation of 5%. Subsequently, the wettability is assigned and the invading phase is injected to simulate piston-like advance of the terminal meniscus. The range of contact angles, measured through the receding phase, used for the simulations of piston-like advance span from 30° to 150° in 15° increments. This wide selection of contact angles covers drainage, imbibition and neutral wettabilities.

Separately, the GNM is used to extract a network from the geometry in Fig. 3.3 and to simulate piston-like advance for the same range of contact angles as in the volume-of-fluid simulations. The maximum capillary pressure necessary to reach the outlet is compared between the two model predictions, in addition to the capillary pressure needed to occupy the centre of the throat and each neighbouring pore. The capillary pressure is defined by Eq. 1.9, where the invading phase corresponds to phase 2.

3.4.2 Analysis of Layer Sagittal Curvature

In the analysis of the three-dimensional layer configuration and its effect on capillary pressure, the property of interest is the deviation of total curvature predictions from two-dimensional analytic predictions for layer curvature, which was derived for a general corner angle in chapter 2 section 2.3.1. To measure this deviation precisely, two equilateral triangular geometries are used which expand and contract with a user-defined expansion angle, β, set to $\beta = 10^\circ$ and 20° in this work. The pore and throat radii are kept constant at 25 and 10 voxels respectively, resulting in a pore-throat contraction ratio of 2.5. The contact angle is kept at $\theta = 30^\circ$, measured through the invading phase. Figure 3.4 shows the two geometries and their dimensions.

The generalised extraction algorithm is used to discretise the corners of the samples shown in Fig. 3.4 and to obtain the generalised network geometries. In the volume-of-fluid simulations performed on the triangular geometries, layers are initialised in the corners of the pore space at an initial wetting phase saturation, S_w, of 14% and 12% for the 10° and 20° geometries, respectively. Subsequently, imbibition is simulated through the samples using the GNM and volume-of-fluid methods detailed previously, where the invading phase pressure now

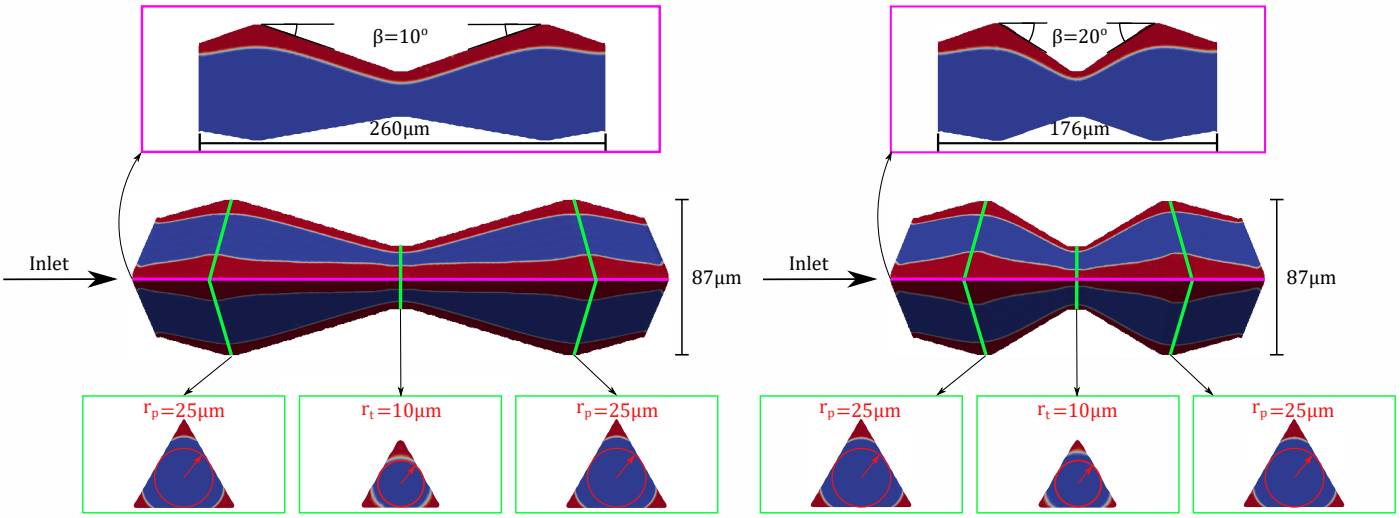

Figure 3.4: The dimensions of the equilateral triangular geometries used in the analysis of layer growth. The two geometries' axial planes at the pore and throat centres are highlighted in green, shown in cross-section at the bottom of the figure. In the axial planes, the pore and throat radii are denoted by r_p and r_t, respectively, and the geometries are axially identical. However, the sagittal planes, in magenta, are different — the left geometry has an expansion angle of $\beta = 10°$, shown in the upper left sagittal curvature cross-section, while the right geometry has $\beta = 20°$, shown in the upper right cross-section. Note that, due to the symmetry of the system, only one sagittal plane of each geometry is shown, while in reality each corner has its own sagittal plane.

corresponds to phase 1 in Eq. 1.9.

The model predictions for the threshold total curvature (capillary pressure) at which snap-off occurs, as well as the evolution of the principal components of curvature (Eq. 3.3) as a function of saturation, are compared at the throat. To obtain the principal components of curvature from the volume-of-fluid simulation, Eq. 2.3 is used to determine the curvature in the axial plane at each time step. The axial curvature is then subtracted from the predicted total curvature to provide the sagittal curvature (Eq. 3.3).

3.5 Results and Discussion

In Section 3.5.1 the local effect of implementing pore-space expansion and sagittal curvature, described in Sections 3.2.1 and 3.2.2, respectively, on threshold pressures for displacement is analysed. Subsequently, the impact of the local parameters on macroscopic relative permeabilities and capillary pressures is presented and discussed in Section 3.5.2. Finally, in Section 3.5.3, the computational cost of including a three-dimensional representation of

interfacial curvature in network models is addressed.

3.5.1 Local Parameters

Pore-space Expansion

Fundamentally, the displacement of one phase by another is a thermodynamic process (*Morrow*, 1970a): displacement will only occur if it is energetically favourable. Displacements control the local configuration of the two fluids in the pore space, which upscales to the averaged macroscopic parameters used for predictions. Therefore, if the threshold pressures for displacements are predicted well, the upscaled predictions can inherit high accuracy.

Figure 3.5 shows the predicted threshold capillary pressures needed to pass through the two-pore system (Fig. 3.3) using the volume-of-fluid method, the GNM prior to improvements, and the calibrated GNM after implementing the updated method for pore-space expansion described in Section 3.2.1.

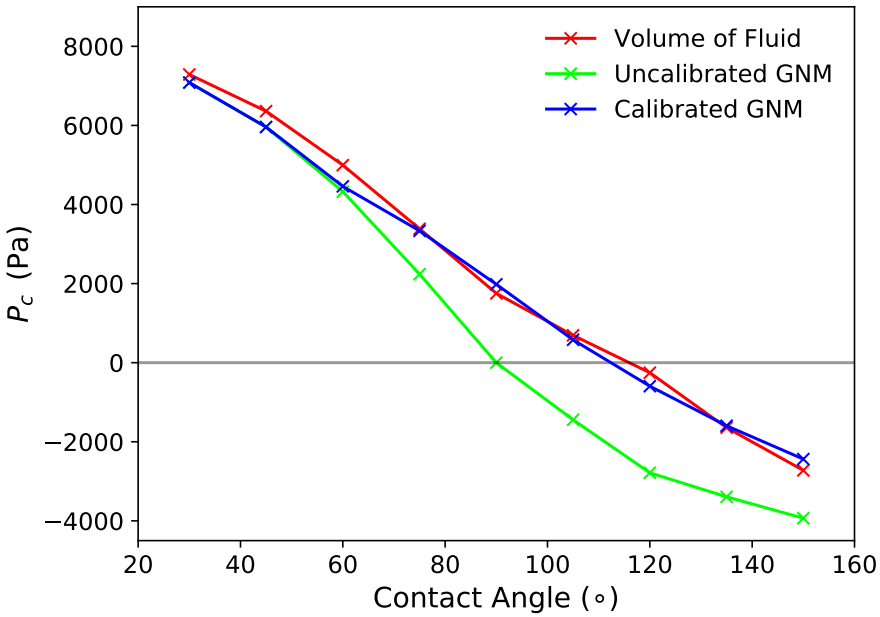

Figure 3.5: The threshold capillary pressure (P_c) needed to pass through the two-pore geometry shown in Fig. 3.3 as a function of receding phase contact angle (θ). The red line shows the volume-of-fluid predictions, while the green and blue lines show the GNM predictions before and after implementing Eq. 3.2, respectively.

The difference in threshold predictions between the volume-of-fluid method and the GNM prior to improvements is substantial. To quantify the difference, a dimensionless discrepancy, $\Delta P_c =$

$\frac{r_t}{2\sigma}|P_c^{VoF} - P_c^{GNM}|$, is defined where P_c^{VoF} and P_c^{GNM} are the capillary pressures predicted by the volume-of-fluid method and the GNM, respectively, for any given contact angle and $r_t = 6\,\mu$m is the inscribed radius of the throat in Fig. 3.3. At the smallest contact angles ($\theta < 75°$) ΔP_c is below 0.1, while at intermediate and larger angles ($\theta \geq 75°$) ΔP_c is significantly greater and exceeds 0.2. However, the apparent wettability predicted by the two models offers the most insight into the physical nature of displacement at the pore-scale: the volume-of-fluid method predicts $P_c > 0$ for all contact angles less than $120°$, indicating that the invading fluid must be forced through the sample as the non-wetting phase. In the uncalibrated GNM, all wettabilities below $\theta = 90°$ are considered non-wetting to the invading phase, while all above are considered wetting. Exactly at $90°$, the capillary pressure is zero, where displacement is driven by cooperative pore-body filling.

A zero capillary pressure at $\theta = 90°$ is an inevitable prediction from network models neglecting the expansion and contraction of the pore space in the sagittal plane, as the cosine term in Eq. 3.1 becomes zero. Indeed, using Eq. 3.1, one can erroneously infer a wetting system, with $P_c < 0$, for all $\theta > 90°$, as shown by the uncalibrated GNM in Fig. 3.5. In reality, this is often incorrect — the apparent wettability of a system depends on the expansion angle of the solid surface in addition to the contact angle (*Rabbani et al.*, 2018). The reason for this dependency becomes clear when considering the forces acting on an interface: in an inclined geometry, the balance of fluid-solid and fluid-fluid interfacial tensions acting at the three-phase contact line gives a contact angle through the Young equation (*Hassanizadeh and Gray*, 1993), however the direction of the fluid-fluid interfacial tension is further inclined from the flow direction by the angle β (Fig. 2.3B). This gives rise to a different curvature, and hence apparent wettability, of the interface as compared to a geometry in which the solid walls are assumed parallel in the sagittal plane (Fig. 1.8K). The effect of an inclined surface, in terms of the macroscopic volume-of-fluid predictions shown in Fig. 3.5, is that the fluid interface maintains a positive curvature far above $\theta = 90°$, and is apparently non-wetting even at weakly wetting contact angles. After implementing Eq. 3.2 with optimised coefficients obtained from Fig. A.1, the calibrated GNM correctly accounts for the impact β has on capillary pressure, accurately reproducing the behaviour predicted by the direct method and reducing

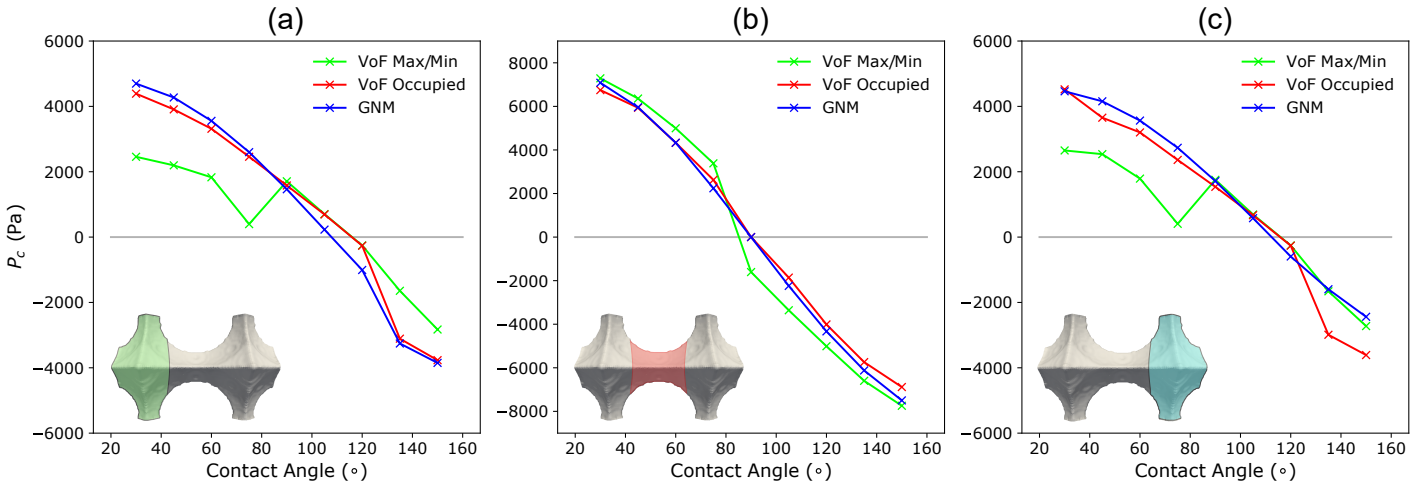

Figure 3.6: The local capillary pressure (P_c) predicted for each pore (a and c) and the adjoining throat (b) in Fig. 3.3, as a function of receding phase contact angle (θ). In the green line, the maximum capillary pressure throughout the volume-of-fluid simulations is attributed to the throat, while the minimum is attributed to the pores, for $\theta < 90°$, and vice-versa for $\theta \geq 90°$. In blue, the generalised network P_c for pore and throat centres is shown. In red, the volume-of-fluid P_c is presented at the time when the pore or throat centre is first occupied with the invading phase.

the absolute difference in predicted threshold capillary pressure by at least 1500 Pa for all $\theta > 75°$. More insights into the nature of displacement at the pore-scale can be obtained by analysing the capillary pressure of the interface as it passes through the centre of each pore and the connecting throat, rather than the threshold of the system as a whole.

Figure 3.6 shows the predicted capillary pressure of the interface as it passes through both pores and the middle throat, for the complete range of contact angles simulated. In pore-scale studies, it is common to attribute the macroscopic thresholds for displacement, shown in Fig. 3.5, to the conceptualised pores and throats of a network — during drainage the most difficult step is considered to be invading the centre of the narrowest region (the throat centre), while during imbibition it is the centre of the widest regions (the pore centres) which offer most resistance to displacement (*Blunt*, 2017). Indeed, network model threshold entry pressures are almost always determined by considering only pore and throat centres. Using this convention, the network model predictions at the throat centre (Fig. 3.6b) agree well with the volume-of-fluid thresholds, with some disagreement in the intermediate contact angle ranges (Fig. 3.6b). The pores, however, show far greater disagreement, particularly during drainage where ΔP_c exceeds 0.25 in places (Fig. 3.6a and c). The principal reason for this

difference is that, if the expansion in the sagittal plane permits, $\cos(\theta+\beta)$ in Eq. 2.2 can take a maximum or minimum value away from the pore and throat centres. This has been studied for neutral wettabilities (e.g, *Pavuluri et al.*, 2020), but here the effect is seen even for relatively low and high contact angles. Note that, while the volume-of-fluid simulations are dynamic, the average capillary number in the simulations was 6.67×10^{-6}, and the maximum capillary number measured at the throat centre did not exceed 1×10^{-4}. These values are small enough to neglect viscous effects on interface curvature and compare with quasi-static predictions.

Figure 3.7 shows the distance of the interfaces, at the threshold maxima and minima shown in Fig. 3.6, from the throat centre. At the lowest contact angles, the conventional assumption that the maximum capillary pressure is at the throat centre, while the minimum is at the pore centres, is approximately correct, with only minor deviations. However, as the contact angle increases, the location of maxima and minima changes smoothly — the minima move towards the throat centre, while the maxima move towards the pore centre. At the highest contact angles, the invading phase is wetting, and the expected behaviour of pore centres representing local maxima and throat centres local minima is again approximately correct. Interestingly, at $\theta = 105°$, the interface location of the P_c maxima reaches its greatest distance from the throat centre, before decreasing at larger contact angles. This inflexion point marks the transition to imbibition — beyond $\theta = 105°$, the contact angle has increased to such an extent that $\cos(\theta+\beta)$ is negative, and so the total curvature becomes negative (Fig. 3.5) with the defending phase protruding into the invading phase, moving the interface centre towards the throat. In summary, the assumption that local minima and maxima are exactly at the pore and throat centres is likely only true for very low or very high contact angles, where small additions will not have much effect on the cosine function, or where β is very small. The better agreement of threshold pressures in the throats in Fig. 3.6b can be attributed, in part, to a far smaller β than in the pores.

In the GNM, the threshold pressure for displacement is taken as the local maximum calculated from three, rather than two, locations: the pore centre, the throat centre, and the half-way point (Eq. 2.2). For this reason, the large pore discrepancies seen in Figs. 3.6a and c at low contact angles, and the relatively larger throat discrepancies at intermediate contact

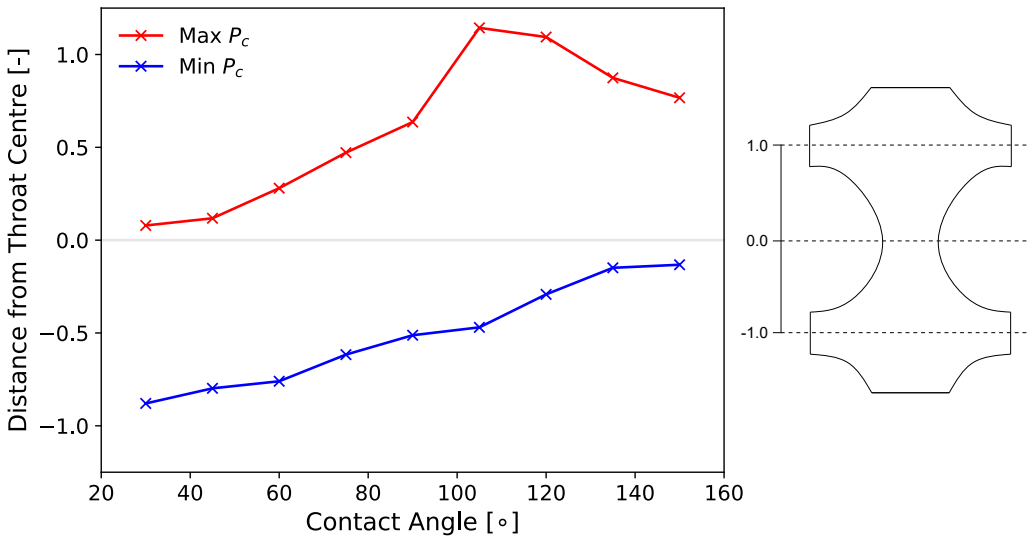

Figure 3.7: The fractional distance from throat centre to pore centre (right schematic) of the interface centre position in the volume-of-fluid simulations as a function of receding phase contact angle (θ). In blue, the interface position at minimum capillary pressure is shown, while red represents the position at maximum capillary pressure. The classical network assumption that capillary pressure extremums occur at pore and throat centres is inconsistent with the direct numerical predictions shown in the figure.

angles in Fig. 3.6b, are not reflected in the macroscopic predictions in Fig. 3.5 — the GNM correctly identifies when the throat or half-way point becomes a local maximum and selects the appropriate threshold capillary pressure for displacement. Similarly, at wetting contact angles ($\theta > 105°$), where the pore-centres control the threshold pressure for displacement and β reaches its maximum value, the calibrated GNM performs well, particularly at the macroscopic scale (Fig. 3.5).

The exact nature of pore-filling is an interesting area of future research (*Ruspini et al.*, 2017) and quickly becomes complex due to the presence of connected throats and the spontaneous formation of layers in wetting regimes, which alter the effective area of the interface (Eq. 2.1). It is possible, however, to gauge the current accuracy of GNM capillary pressure estimates at the pore-centres: Fig. 3.6 also shows the volume-of-fluid capillary pressure predictions when the pores and throats first become occupied — that is, when the centre of the maximal balls defining the pore and throat centres first become filled with the invading phase. The network model agrees well with the direct method here, further validating that the capillary pressure estimates from Eq. 2.2 and the updated β in Eq. 3.2 are accurate.

Layer Sagittal Curvature and Snap-Off

The expansion and contraction of the pore space is clearly an important factor in piston-like displacement, but in this section it is shown that the three-dimensional nature of real porous media must also be considered for layer configurations. For any porous medium with corners and crevices to its pore space, wetting layers will maintain connectivity even after the centres of the pores and throats have been invaded by a non-wetting phase. If the wetting fluid is re-injected, the layers will swell until the interfaces from two neighbouring corners meet. At this point, which first occurs in the narrowest regions of the pore space, the fluid configuration becomes unstable and the wetting phase rapidly fills the small region. This is the snap-off process, which acts to disconnect and trap the defending, non-wetting fluid, and has important implications for many two-phase flow processes. Therefore, correctly predicting the pressure and saturation at which snap-off occurs is crucial.

Figure 3.8 shows the predicted total curvature for snap-off, using a variety of approaches, for the 10° and 20° expansion geometries shown in Fig. 3.4. The curvature of a layer interface in the axial plane with an arbitrary fluid-solid contact length is easily obtained from 2.3. Classical network models rely solely on analytic solutions to Eq. 2.3 when calculating the total curvature at which the three-phase contact point of two adjacent corners in a throat will meet, and if the prevailing capillary pressure equals this critical value before a piston-like interface has reached the throat, snap-off will occur. The two-dimensional analytic prediction clearly overestimates the curvature at which snap-off occurs compared to the volume-of-fluid predictions. In addition, the classical approach predicts the same critical curvature value in both geometries, while the volume-of-fluid method predicts a decrease in the critical curvature with increasing expansion angle. The physical meaning of this is that, in classical networks, snap-off will occur at lower wetting saturations, or equivalently higher non-wetting residual saturations, than in reality. Moreover, if two pore geometries are identical in their axial planes, but vary in their sagittal planes — as in Fig. 3.4 — the predicted snap-off curvature in the two media will be the same. The sole cause of this predictive inaccuracy is the classical assumption that curvature in the sagittal plane is negligible and does not contribute to the total curvature of a layer interface. In reality, fluid layers conform to the geometry of the pore

space, which expands away from throat centres. In the sagittal plane, the geometric constraint of an expanding medium results in fluid layers protruding into the centre fluid, with a negative curvature, at the throat. This is shown schematically in Fig. 1.8l and in cross-sections from direct simulations in Fig. 3.4. From Eq. 3.3, a negative sagittal curvature reduces the total curvature, or capillary pressure, needed to achieve a given axial curvature — snap-off becomes more difficult with increasing throat sagittal curvature, as predicted by the volume-of-fluid method in Fig. 3.8.

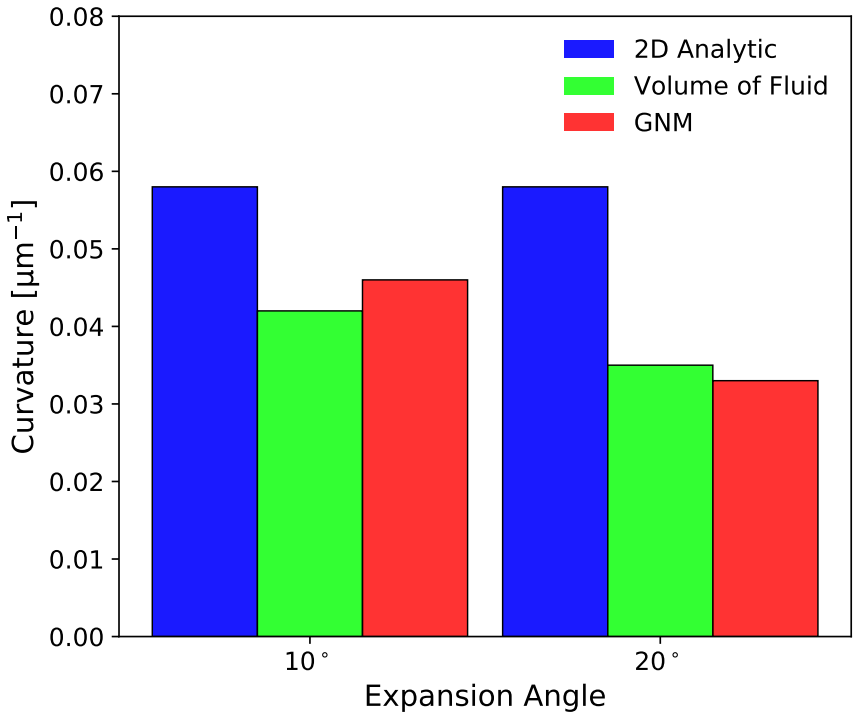

Figure 3.8: The predicted total curvature at which snap off occurs for the classical, two-dimensional approach (blue), the volume-of-fluid method (green) and the GNM after implementing sagittal curvature described in Section 3.2.2 (red).

After including throat sagittal curvature, as in Eq. 3.4 and with the optimised coefficient $c = 1.5$ (Fig. A.2a), the GNM accurately predicts both the lower critical curvatures than analytic solutions and the variation between expansion angles shown by the volume-of-fluid simulations. However, underpinning the approach used in Section 3.2.2, and indeed other approaches (*Deng et al.*, 2014; *Raeini et al.*, 2018), is the assumption that sagittal curvature is defined solely by the geometry and is not a function of pressure. For a truly predictive model it is not sufficient to only predict the threshold curvature for snap-off, based purely on pore-space geometry — the effect of sagittal curvature on saturation must also be considered,

as this is a curvature of the fluid-fluid meniscus, not the solid surface.

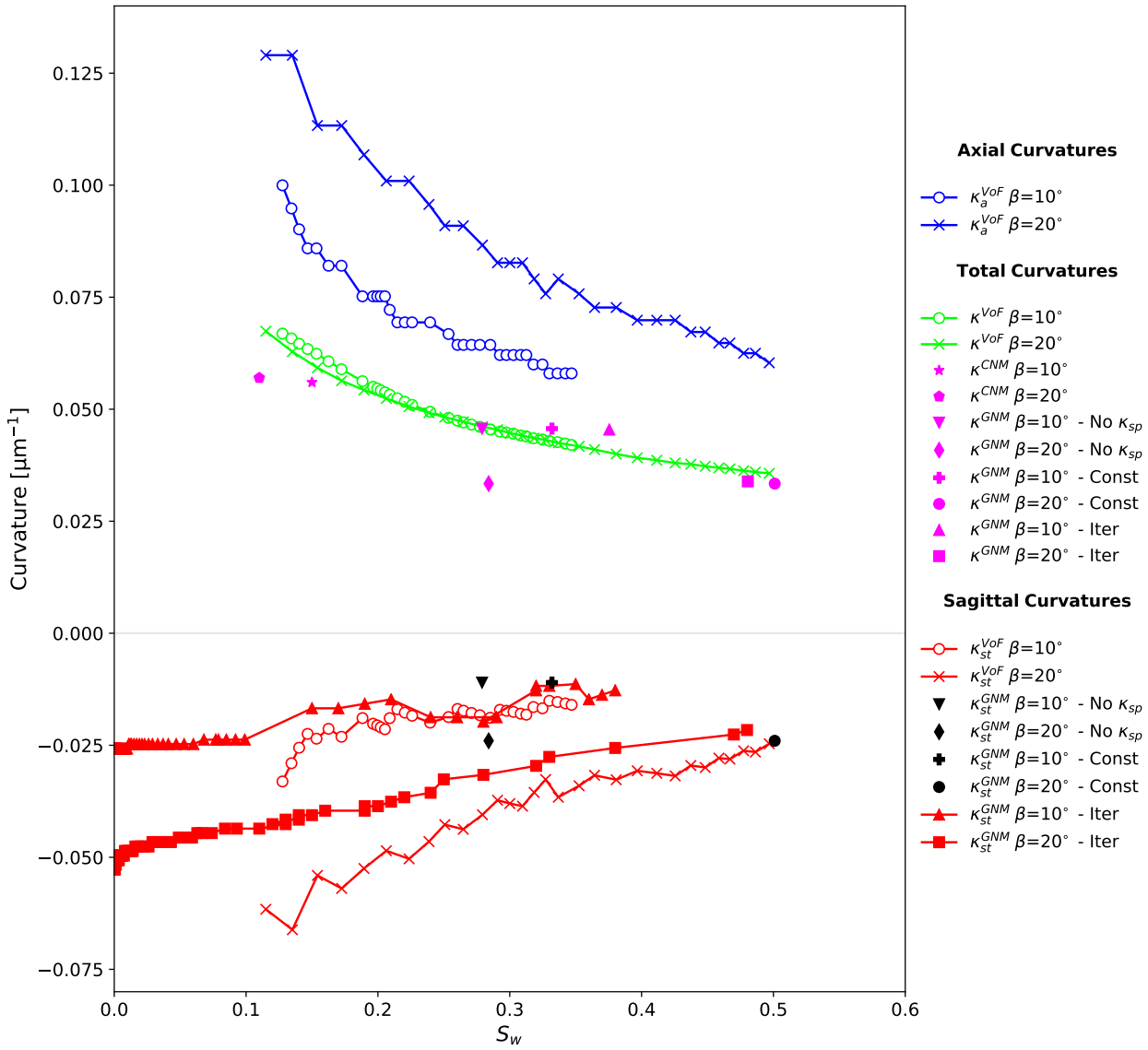

Figure 3.9: Curvature at the throat centre as a function of wetting phase saturation S_w, for the $\beta = 10°$ and $\beta = 20°$ geometries shown in Fig. 3.4, for a contact angle of $30°$ through the wetting layer. The total curvatures from the volume of fluid simulations are shown in green (κ^{VoF}), while the axial curvatures obtained using Eq. 2.3 throughout the volume-of-fluid simulations are shown in blue (κ_a^{VoF}). The difference between κ_a^{VoF} and κ^{VoF} gives the sagittal curvature, shown in red (κ_{st}^{VoF}). In each case, the end point represents the value at snap-off. The magenta symbols represent the total curvature at snap-off obtained with the GNM when: no sagittal curvature is considered, as in classical network models (κ^{CNM}); only constant throat sagittal curvature is considered (No κ_{sp} κ^{GNM}); constant pore and throat sagittal curvatures are considered (Const κ^{GNM}). The sagittal curvatures at snap-off associated with the total curvatures obtained using the GNM are shown by the black symbols. Finally, the GNM predictions for sagittal curvature after implementing the iterative method in Fig. 3.10 (Iter κ_{st}^{GNM}) are shown in red, with the associated GNM total curvature predictions for snap-off shown by magenta symbols (Iter κ^{GNM}).

Figure 3.9 shows the total, axial and sagittal curvatures at the throat, as a function of

saturation, for the volume-of-fluid method. As expected, the total curvature decreases with increasing saturation — the invading phase pressure rises causing the layers to swell toward the centre of the pore space, increasing the wetting phase saturation, and the pressure difference between phases reduces, decreasing the capillary pressure. As the capillary pressure decreases, the curvature in the axial plane also decreases. However, it is again evident that the classical assumption of total and axial curvature equivalency is incorrect; the axial curvature is considerably larger than the total curvature for any given saturation. Furthermore, while the total curvatures remain similar for the $\beta = 10^\circ$ and $\beta = 20^\circ$ geometries, the axial curvatures are markedly different, with larger axial curvatures for a given wetting saturation in the 20° sample — this arises as sagittal curvature suppresses the movement of layers in the axial plane.

A variety of generalised network modelling predictions for saturation and curvature at snap-off are also shown in Fig. 3.9. Without pore or throat sagittal curvature, the GNM threshold curvature predictions reduce to that of a classical network: there is no difference in the threshold total curvature predictions for the two expansion angles; the threshold total curvatures are higher than predicted by direct simulations; and snap-off occurs at far lower wetting saturations than in the direct simulations. If only throat sagittal curvature is included, the GNM's threshold curvature predictions improve dramatically, as shown in Fig. 3.8, but only moderate improvements in wetting saturation at snap-off are observed in Fig. 3.9. While throat sagittal curvature decreases the total curvature necessary for snap-off, allowing larger volumes of wetting-phase to occupy the pore space before snap-off occurs, it is the pores which have the largest control over saturation. If pore and throat sagittal curvature are included in the GNM, with optimised coefficients $(c, d) = (1.5, 0.75)$ (Fig. A.2A), threshold predictions agree well with the direct simulations.

The most interesting finding, however, is that the overall decrease in axial and total curvature predicted by the volume-of-fluid simulations is not linear, but decreases asymptotically until the critical axial curvature for snap-off is reached. This can only occur if the sagittal curvature is not constant. In Fig. 3.9, the sagittal curvature is quantified for both geometries and confirms all previous inferences: the sagittal curvature is negative, smaller in the 10° than

the 20° geometry, and increases with increasing saturation, or decreasing capillary pressure. The implication of the latter finding is that sagittal curvature cannot be modelled purely as a function of solid geometry — as hitherto assumed — but rather depends on the morphology of the fluid interfaces.

In Fig. 3.10, the method described in Section 3.4.2 is extended to allow the calculation of sagittal curvature from interface morphology. Initially, layers are assumed to have a sagittal curvature defined by the geometry. A capillary pressure is imposed on the network model which defines the total curvature and, together with the initial sagittal curvature estimate, gives the axial curvature. The centres of the layer interfaces in the axial plane are found and used to define new circles (Fig. 3.10a), from which Eqs. 3.4 and 3.5 provide an updated sagittal curvature. The iterative method is applied throughout the simulation (Fig. 3.10b) to find consistent radial and axial curvatures of the fluid-fluid meniscus; it is the axial curvature which will control when snap-off occurs. Per pressure increment, the method can either be implemented iteratively, or as a single readjustment if the simulation pressure increment is small. The latter approach is used here, as small changes in prevailing capillary pressure allow finer comparison with volume-of-fluid results.

Figure 3.9 further shows predictions for sagittal curvature, and the total curvature at which snap-off occurs, obtained using the GNM with the extended method of Fig. 3.10, with re-optimised coefficients $(c, d) = (3.5, 3.0)$ (Fig. A.2b) pertinent to the iterative approach. The semi-analytic approximations in Eq. 3.4 agree well with the direct solutions to Navier-Stokes and Young-Laplace equations, for both geometries. Initially, there is larger disagreement between the sagittal curvatures of the two models due to the GNM reaching lower initial wetting-phase saturations compared to the volume-of-fluid method. Furthermore, the early stages ($\sim S_w = 0.1 - 0.15$) of the direct simulations represent the user-initialised invading phase adjusting into equilibrium with the prevailing capillary pressure. Beyond $S_w = 0.15$, however, the agreement in sagittal curvature is very good, and the total curvature and saturation predictions at snap-off have only minor differences.

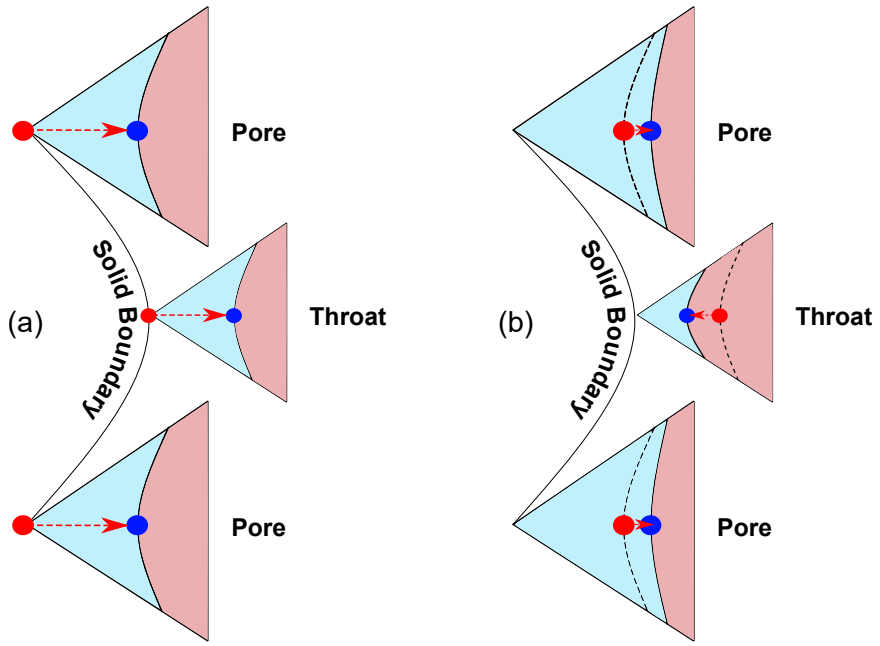

Figure 3.10: An illustration of the iterative algorithm used to update the sagittal and axial curvatures of a layer interface at the pore (top and bottom) and throat centres (middle). Prior to injection, an initial guess for sagittal curvature is taken using the method described in Section 3.4.2, with the three red points in (a) representing the points used to define the circles in Figs. 3.2a and b. Upon injection, the prevailing capillary pressure and initial guess for sagittal curvature are used to determine the axial curvature and hence the location of interface centres, shown by the blue points in (a). Subsequently, the interface centres in (a) comprise the points used to determine the updated sagittal curvature, shown by the red points in (b). In turn, this provides new interface centres, shown by the blue points (b).

3.5.2 Macroscopic Parameters

The focus of the analysis thus far has been on local parameters. While it is useful to calibrate network models on small samples, where comparison with high-resolution DNS is possible, the real strength of network models lies in their potential to model flow through large domains, with tens-to-hundreds of thousands of pores and throats. In Fig. 3.11, the effect of neglecting, having a constant, or implementing an iterative sagittal curvature in the GNM is assessed by comparing macroscopic capillary pressure and relative permeability predictions, for a network extracted from a 1000^3 Bentheimer sandstone image, to oil-water two-phase flow experimental results after waterflooding (*Gao et al.*, 2017; *Lin et al.*, 2018). The capillary numbers in the experiments by *Lin et al.* (2018) and *Gao et al.* (2017) were 6.6×10^{-7} and 3.0×10^{-7}, respectively, and macroscopic property measurements were made when the differential pressure across the cores were stable. This indicates that displacement was

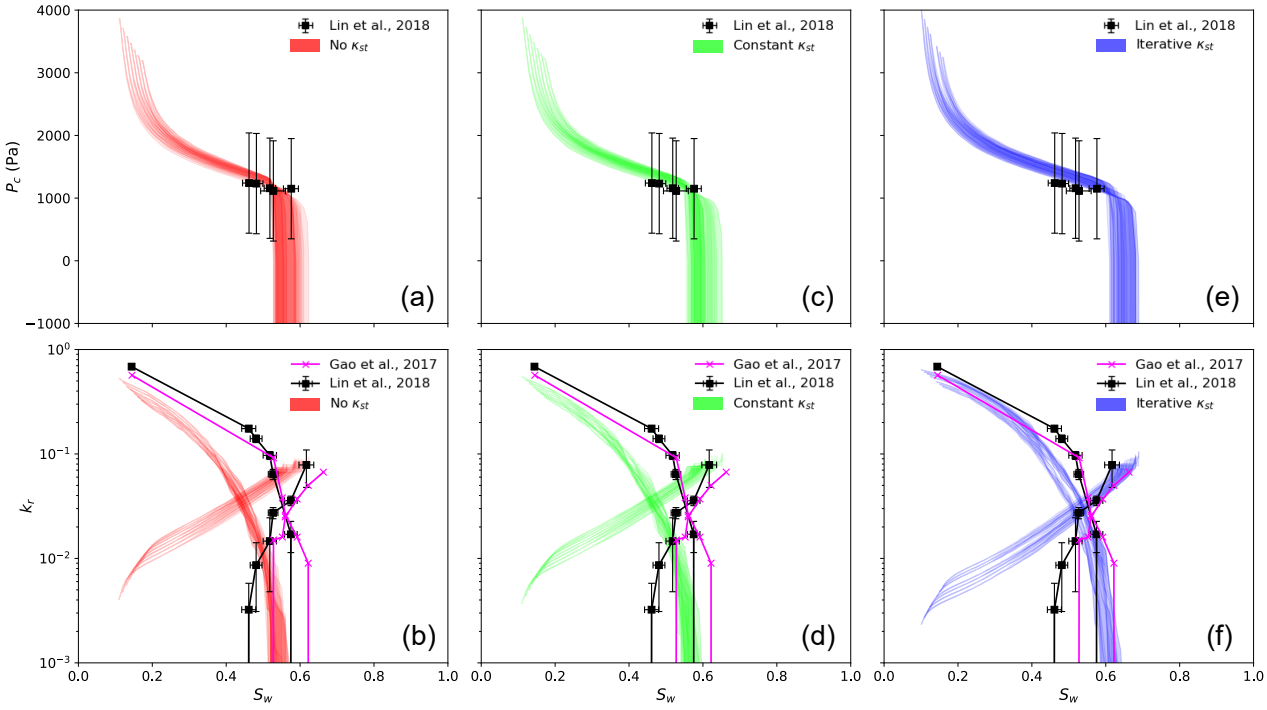

Figure 3.11: Predicted macroscopic capillary pressures (P_c, top row) and relative permeabilities (k_r, bottom row) for a water-wet Bentheimer sandstone using the GNM. Predictions obtained by neglecting sagittal curvature (red) are shown in (a) and (b), whilst (c) and (d) show a constant sagittal curvature (green). Figures (e) and (f) present GNM predictions using an iterative method (blue) to determine sagittal curvature throughout the simulation. The shaded areas represent the GNM's sensitivity to contact angle, θ, and initial water saturation, S_{wi}: in each figure, GNM simulations span the range of simulations defined by $S_{wi} = 0.14 \pm 0.03$ and $\theta = 48° \pm 5°$. The black and magenta lines are pore-scale experimental results by *Lin et al.* (2018) and *Gao et al.* (2017), respectively, and the error bars on the experimental capillary pressure and relative permeability values indicate uncertainties in the measurements (*Foroughi et al.*, 2020).

capillary dominated in both experiments, and that measurements were taken in steady-state conditions, where fluid configurations are mostly constant. As such, comparison with the quasi-static GNM is possible. The shaded areas in Fig. 3.11 represent all GNM predictions using a single value of contact angle assigned in the range $[43°, 53°]$, and an initial water saturation after primary drainage in the range $[0.11, 0.17]$. These ranges correspond to the experimental measurements and associated uncertainties of thermodynamic contact angle (*Blunt et al.*, 2019) and initial water saturation obtained with differential imaging (*Gao et al.*, 2017). The coefficients of pore and throat sagittal curvature are unchanged from Section 3.5.1 are described in detail in Appendix A. Furthermore, an assessment of the impact that an uncertainty in β would have on macroscopic predictions is presented in Appendix B.

While all three approaches produce similar capillary pressure values — which lie within the uncertainty of the experimental measurements — the predicted residual saturations are lower if sagittal curvature is included in the GNM (Figs. 3.11a, c and e). The variation in residual saturations is also evident in Figs. 3.11b, d and f, where significant differences in relative permeabilities can also be seen. If sagittal curvature is completely neglected, snap-off becomes easier and the residual non-wetting saturation increases beyond the range of the experimental measurements (Fig. 3.11b). Furthermore, the experimental measurements of capillary pressure shown in Figs. 3.11a, c and e were obtained during the intermediate water fractional flows — imbibition concluded at a wetting saturation $S_w = 0.62$ (*Lin et al.*, 2018), which is under-predicted by the neglection of sagittal curvature in Fig. 3.11a. The exclusion of sagittal curvature can, in part, explain why some studies have struggled to reproduce the capillary trapping behaviour of experiments using network models, particularly if low contact angles typical of strongly water-wet systems are assigned to the network (*Valvatne and Blunt*, 2004; *Pentland et al.*, 2010; *Bondino et al.*, 2013; *Raeini et al.*, 2015). In addition to an over-prediction of residual saturation, as the axial curvature of layer interfaces accommodates the entirety of any capillary pressure decrease, the oil and water relative permeabilities are too low and too high, respectively — for a given pressure the layers are too thick, reducing the conductivity of the phase occupying the centre (oil) while increasing the conductivity of the layers (water). The inclusion of constant sagittal curvature, calibrated to replicate volume-of-fluid total curvature predictions at snap-off (Fig. 3.8), has a noticeable improvement on residual saturations and relative permeabilities, but not to an extent to agree with the experiments (Fig. 3.11d). This is because the absolute value of sagittal curvature at a throat is higher than the value at snap-off for the majority of the experiments, as shown by the DNS results in Fig. 3.9, and so a constant sagittal curvature still overestimates the area of layers in the throat axial-plane.

Employing the iterative method, with calibrated throat and pore sagittal curvature as in Fig. 3.9, gives a good agreement between the GNM and experimental results (Fig. 3.11e and f). The throat sagittal curvatures are initially large and negative, keeping layers further towards corner vertices and resulting in low initial wetting phase permeabilities. Meanwhile,

the centre-phase occupies a larger cross-sectional area and has a greater permeability than in negligible, or constant, sagittal curvature methods. As the sagittal curvature increases throughout the simulation, the suppression of layer movement in the axial plane lessens, but still results in a far smaller residual than other methods, and overall the effect is a shift in the relative permeabilities and capillary pressures to the right, in agreement with the experiments.

It is further evident from Figs. 3.11b, d and f that, whilst the iterative method leads to substantial improvement in oil relative permeability, the water relative permeability at low saturations shows notable discrepancy with experiments across all methods. This is due to two factors: firstly, the pore-scale experiments in Fig. 3.11 were performed on long, narrow cores with an assumed uniform saturation profile. However, pressure drop estimates from narrow cores are prone to inaccuracies caused by local saturation heterogeneities, leading to erroneously low relative permeabilities (*Zhang et al.*, 2023). Secondly, pore-network models commonly rely on empirical correlations based on two-dimensional finite element predictions to compute centre and layer phase conductivity (e.g., *Øren et al.*, 1998; *Valvatne and Blunt*, 2004). While these correlations provide reasonable predictions, future work could use three-dimensional data-driven methods to obtain more accurate correlations.

3.5.3 Computational Cost

The improvements in network model predictions achieved through the inclusion of pore-space expansion (Eq. 3.2) and sagittal curvature (Eqs. 3.4 and 3.5) is evident from the results presented in Figs. 3.5, 3.6, 3.9 and 3.11. A key trait of network models, however, is their computational efficiency; any improvements in predictive ability should not sacrifice this efficiency. It is important to note that direct simulations are not required to implement the network model developments presented in this work; DNS were performed solely to measure and improve the accuracy of the approximations on small synthetic systems, while no DNS were performed to obtain the GNM results in Fig. 3.11. The computational costs of the algorithms needed to implement the methods presented in this study scale linearly with network size, which is negligible compared to the cost of determining network permeability, the order of filling and phase connectivity. Thus, the methods presented here offer enhanced

physical accuracy with minimal additional cost.

To demonstrate the retention of network model efficiency in the presence of a three-dimensional representation of curvature, the DNS performed on the synthetic geometries in Figs. 3.3 and 3.4 took approximately two weeks using 88 cores in parallel. The GNM simulations performed on the same geometries took less than five seconds using a single core on the same machine. Furthermore, Fig. 3.11 represents 63 GNM simulations performed on an image of a real medium. Each simulation, regardless of the curvature method, took approximately 30 minutes using a single core. The simulations were scheduled to run on 5 cores in parallel, for a total computational time of approximately 6.5 hours. In contrast, a single direct numerical simulation on an image of this size would take on the order of weeks and would require ten times the computational resources.

3.6 Conclusions

In this chapter, a fully three-dimensional characterisation of interfacial curvature has been implemented into a network model, which includes the sagittal plane in the computation of displacement capillary pressures. The new expressions for displacement capillary pressures were compared and validated against high resolution volume-of-fluid simulations on synthetic geometries, constructed to vary in their sagittal planes. After validation, the effect on macroscopic capillary pressure and relative permeabilities was analysed.

Direct simulations demonstrate that neglecting the expansion and contraction of the pore space in a network model gives inaccurate predictions of threshold capillary pressure for piston-like advance. After accounting for pore-space expansion, the network model results agreed well with direct methods. Additionally, the conventional view of thresholds occurring exactly at pore or throat centres, even for strongly-wetted systems, was challenged. The expansion of the pore-space necessitates the consideration of intermediate regions as threshold points for displacement in a network model, particularly for contact angles around $90°$.

Similarly, the classical assumption that the curvature of fluid interfaces in the sagittal plane is negligible proved incorrect. Direct simulations showed that snap-off predictions differ substantially for systems that are axially identical but vary in their sagittal planes, while quasi two-dimensional approximations employed in classical network models were unable to replicate such behaviour. Treating curvature in the sagittal plane as a constant property defined by the solid geometry improved the network predictions, but an iterative approach, which considered the exact location of interfaces, more accurately replicated the direct simulations for sagittal curvature.

Macroscopically, sagittal curvature has a large effect on residual saturation and relative permeabilities. Without including sagittal curvature, the network model overestimated the degree of snap-off, and hence residual saturations, and the wetting-phase relative permeability, while underestimating the non-wetting phase relative permeability, compared to experiments. This has important implications for a range of phenomena. For instance, accurate assessment of the efficacy of CO_2 storage relies on predictions of residual saturations. Without including

sagittal curvature, overestimates of trapping are inevitable. Likewise, in the construction of fuel cells, it is necessary to design optimum transfer of fluid through the gas diffusion layer and adjacent bipolar plate (e.g, *Okonkwo and Otor*, 2021; *Zhang et al.*, 2021) — without a consideration of sagittal curvature, relative permeability predictions are likely inaccurate. Similar to local property analysis, the iterative approach to modelling sagittal curvature gave good agreement with experimental results.

Importantly, macroscopic predictions of three-dimensional effects were obtained from simulations derived from a 1000^3 voxel image of a Bentheimer sandstone at a resolution of 3.58μm, which is of sufficient size to be considered representative of larger samples (*Ramstad et al.*, 2010; *Mostaghimi et al.*, 2013) used in core-scale experimental measurements of relative permeability. This indicates that the network model developments could have tangible consequences for larger Darcy-scale and field-scale simulations — relative permeabilities are known to be a sensitive input parameter for field-scale models (e.g, *Li and Horne*, 2008), and the impacts shown in Fig. 3.11 could be large enough to influence field-scale predictions.

In the next chapter, the improved GNM will be compared to lattice-Boltzmann simulations of two-phase flow across a range of wettabilities. The analysis will highlight the strengths that network modelling possesses over direct methods in capturing wettability-dependent phenomena.

CHAPTER 4

PORE-SCALE MODELING OF TWO-PHASE FLOW: A COMPARISON OF THE GENERALIZED NETWORK MODEL TO DIRECT NUMERICAL SIMULATION

The contents of this chapter have been published in Giudici et al. (2023b).

4.1 Overview

In this chapter, oil-water two-phase flow simulations from the updated generalized network model are compared to predictions from a recently developed colour-gradient lattice-Boltzmann model (*Akai et al.*, 2018, 2020b). The comparison encompasses both macroscopic (capillary pressure) and local (saturation and occupancy) properties. A quantitative, pore-by-pore analysis of the models is then presented for a Bentheimer sandstone and a synthetic beadpack, covering a full range of wetting states, in addition to comparisons with experimental data for Bentheimer sandstone. Overall, this chapter provides insights into the relative strengths and shortcomings of each approach, and seeks to understand the impact that wettability can have on displacement by analysing the difference in pore-scale behaviour between the GNM and higher fidelity approaches.

4.1.1 Direct Numerical Simulations and Samples

Two-phase flow predictions obtained with the GNM are compared to those generated in *Akai et al.* (2020b) using a recently developed lattice-Boltzmann model (LBM). Below, the method used to obtain LBM predictions is briefly described; for a complete treatment of the reader is referred to *Akai et al.* (2018).

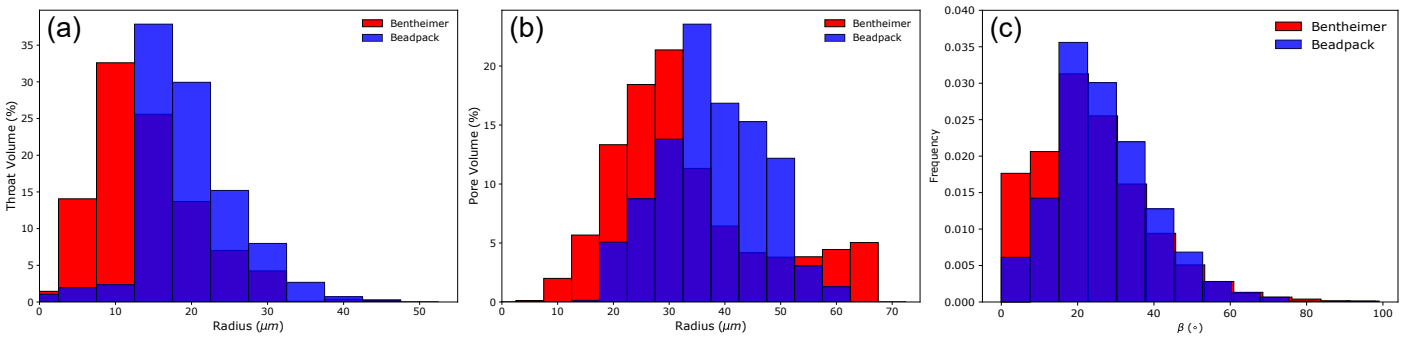

Figure 4.1: The pore-volume weighted radius distributions for throats (a) and pores (b). In (c), the frequency distribution of expansion angles (β) is shown. The red bars represent Bentheimer and the blue bars represent the synthetic beadpack.

Two-phase flow simulations on two 288^3 voxel samples — a synthetic beadpack and a micro-CT imaged Bentheimer sandstone, both with a voxel size of $3.58\,\mu$m — were performed using a colour gradient lattice-Boltzmann model by *Akai et al.* (2020b). Although small, this size is likely large enough to be considered a representative elementary volume for a Bentheimer sample (*Ramstad et al.*, 2010; *Mostaghimi et al.*, 2013) and hence also for the beadpack, as its pore space is more homogeneous than Bentheimer.

The pore-radius distribution for both samples is shown in Fig. 4.1. Initially, drainage simulations were performed with a uniform contact angle, θ, of $45°$ by increasing the oil pressure, relative to the water pressure, and applying constant pressure boundary conditions at the inlet and outlet. Following primary drainage, water injection was simulated for three wetting states in each sample: uniformly water-wet (WW, $\theta = 45°$), uniformly oil-wet (OW, $\theta = 135°$), and a mixed-wet (MW) state exhibiting a non-uniform allocation of contact angle — the contact angle assigned at the start of waterflooding was positively correlated with the oil saturation of pores after drainage, mimicking wettability alteration in realistic settings. The contact angles assigned after drainage in the MW case ranged from $45°$ to $165°$, with a volume-weighted average of $90°$. Each waterflood was initiated from the same drainage simulation. All simulations were in a capillary dominated regime, with an average capillary number $Ca < 10^{-5}$ during the displacements.

Using a no-slip boundary condition, at least three grid blocks are required at the solid-wall to capture fluid layers using DNS. Furthermore *Zhao et al.* (2020) suggested that at least 10 grid blocks across the diameter of a throat are needed for LBM P_c predictions to lie within 5% of

analytic values, and insufficient mesh resolution has an adverse effect on relative permeability predictions (*Kohanpur et al.*, 2020). The grid size used in the simulations here was $3.58\,\mu$m. Figure 4.1 shows that the volume-average pore and throat diameter (μm) is 66 and 28 for Bentheimer, and 76 and 38 for the beadpack, respectively. With a grid size equal to the voxel size of $3.58\,\mu$m these values correspond to ~ 10 grid blocks per throat and ~ 20 grid blocks per pore. Note that this is the volume-average resolution – some throats in Fig. 4.1 will have fewer grid blocks per diameter, particularly for Bentheimer. In this work, experimental capillary pressures will be presented to validate model predictions and, to avoid resolution errors, pore-by-pore analysis excludes the throats. The main implication, however, is that layer flow cannot be simulated by the LBM at this resolution.

For many media, particularly if the structure and porosity are heterogeneous, the representative size may be cubic millimetres or centimetres in volume. Achieving micrometre resolution in such volumes is extremely demanding, leading many studies to omit small-scale features in more complex media (e.g., *Ramstad et al.*, 2010; *Porter et al.*, 2009; *Leclaire et al.*, 2017; *Boek et al.*, 2017). As shown later, this omission can have significant impacts on macroscopic predictions of trapping and pore-by-pore displacement characteristics.

4.1.2 Assignment of Contact Angle

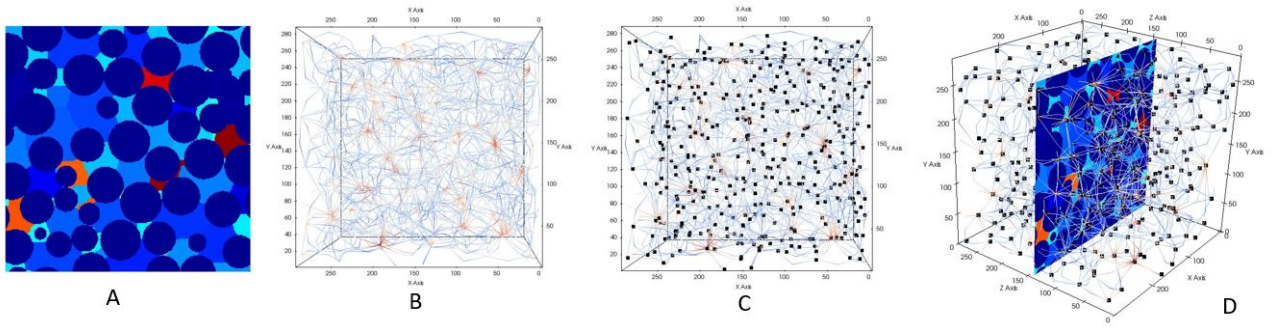

Figure 4.2: The steps implemented to obtain a spatial match in wettability between models. The pore regions identified by *Akai et al.* (2020b) are shown in A. The generalized network is shown in B, with the pore centres represented by black squares in C. Finally, each pore centre in C is mapped to a pore region in A, shown in D. After mapping, wettability assignment is easily transferred between models.

The generalized network extraction algorithm differs from the method used in the LBM study by *Akai et al.* (2020b) to identify pores. In the water-wet and oil-wet cases this is inconsequential as the wettability assignment is uniform. The mixed-wet cases, however, require a spatial match in contact angle. This is achieved by implementing the steps shown in Fig. 4.2. A generalized network is extracted from the images used in *Akai et al.* (2020b). The pore centres in the generalized network model are then overlaid onto the pore regions used in the LBM study. Finally, the contact angle associated with each pore-region in the LBM study is mapped to the pore-centre(s) of the network model. In this way, the spatial distribution of contact angle is matched as closely as possible between models — Fig. 4.3 compares the distribution of contact angles as a function of pore-volume, in the mixed-wet case, for both samples. The distributions are similar, with only a 1° and 2° difference in the volume-weighted average of contact angle for Bentheimer and the beadpack, respectively.

Network flow simulations were performed after the contact angle was assigned pore-by-pore to closely match those of the LBM study, and a series of macroscopic and pore-by-pore comparison measures were implemented on the model predictions.

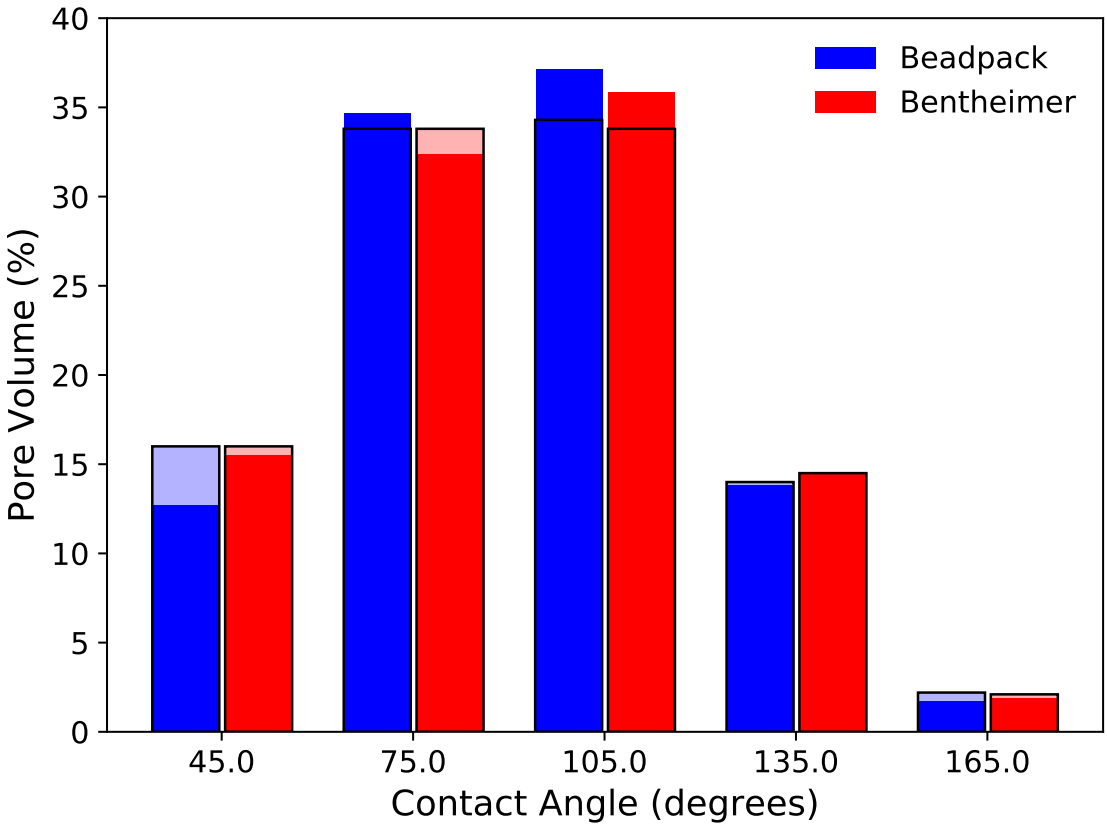

Figure 4.3: The contact angles assigned to the pore volume of the mixed-wet case, prior to waterflooding, for the GNM and the *Akai et al.* (2020b) LBM study (pale bars outlined in black). The volume-weighted average contact angle is $90°$ in the LBM study while it is $91°$ and $92°$, for the Bentheimer and beadpack respectively, in the GNM.

4.1.3 Comparison Measures

To compare the higher fidelity DNS model and the GNM, a series of qualitative and statistical measures are implemented on both a macroscopic and a pore-by-pore basis, explained below.

Macroscopic Mismatch

Capillary pressure (Eq. 1.9) is used to qualitatively determine the similarity between the two modelling approaches at a macroscopic scale. Capillary pressure is dependent on pore geometry, wettability, saturation and the invading phase history (capillary pressure hysteresis). Hence, differences in P_c provide important insights into pore-scale displacement. The capillary pressure for drainage and each waterflood, for both models, are shown for Bentheimer and the beadpack. For the Bentheimer sandstone, experimental observations for drainage, water-wet waterflooding (*Lin et al.*, 2018) and mixed-wet waterflooding (*Lin et al.*, 2019) are presented

for comparison, with an updated quantification of uncertainty by *Foroughi et al.* (2020).

Another macroscopic measure used is the Pearson correlation coefficient, r, which is a measure of the linear relationship between two datasets and is defined as:

$$r = \frac{\sum_{i=1}^{n}(\psi_i^a - \bar{\psi}^a)(\psi_i^b - \bar{\psi}^b)}{\sqrt{\sum_{i=1}^{n}(\psi_i^a - \bar{\psi}^a)^2}\sqrt{\sum_{i=1}^{n}(\psi_i^b - \bar{\psi}^b)^2}} \qquad r \in [-1, 1], \tag{4.1}$$

where ψ_i^a and ψ_i^b are the i^{th} members of two datasets, a and b, with mean values $\bar{\psi}^a$ and $\bar{\psi}^b$, and n is the sample size. The Pearson correlation coefficient between saturation and radii, and occupancy and radii, is calculated at the end of drainage and each waterflooding cycle for the LBM predictions (r_{LBM}), and compared to the correlation coefficients calculated for the network model predictions (r_{GNM}) when the mean difference in the models' pore-saturation is zero (detailed in Section 4.1.3) and the wettability is the same. This comparison determines the degree to which the models agree in terms of their invasion behaviour — similar coefficients indicate agreement in the invasion trends (i.e, are large or small pores preferentially filled) and in variance of the prediction. A value of -1 indicates perfect negative correlation and a value of 1 indicates perfect positive correlation, while 0 indicates no correlation. As wettability assignment is equal in both models, a large disparity in the Pearson correlation coefficient reflects differences in the invasion algorithm and treatment of pore-space geometry.

Finally, the residual saturation after waterflooding, S_{or}, is primarily controlled by the amount of trapping due to snap-off and the presence of flow through layers, which in turn are controlled by the wettability of the system. It has important implications for oil recovery and CO_2 trapping (*Andrew et al.*, 2014a; *Krevor et al.*, 2015). S_{or} as a function of wettability is presented as a measure of the macroscopic differences manifesting from the treatment of small-scale phenomena and model resolution.

Pore-by-Pore Mismatch in Occupancy and Saturation

LBM predictions at the end of drainage and the end of waterflooding are first mapped onto pore-network elements, in a similar fashion to contact angle (Fig. 4.2), enabling pore-by-pore comparison between models. The mean difference ($\bar{\Delta}$) and mean absolute differences ($|\bar{\Delta}|$)

between model predictions for occupancy and oil saturation (the fraction of the volume of a pore filled with oil) are then calculated, as in *Raeini et al.* (2019):

$$\bar{\Delta}\psi = \frac{\sum_{i=1}^{n} w_i(\psi_i^a - \psi_i^b)}{\sum_{i=1}^{n} w_i} \tag{4.2}$$

$$\left|\bar{\Delta}\right|\psi = \frac{\sum_{i=1}^{n} w_i\,|\psi_i^a - \psi_i^b|}{\sum_{i=1}^{n} w_i} \tag{4.3}$$

where ψ represents any flow parameter, such as saturation or occupancy, for two data sets a, b while w_i is a weighting factor — chosen here to be the pore volume. Equation 4.2 can be considered the difference in the average, upscaled flow parameter, as local differences between models can cancel, while Eq. 4.3 represents a true pore-by-pore difference — it is the normalised sum of pore-by-pore discrepancy. A difference here indicates disagreement in the models' invasion algorithms, pore-space geometry and incorporated physics — as in Eq. 4.1 — but provides a direct measure of the local disagreements. Both pore-by-pore comparison measures are determined when the mean difference in pore saturation (Eq. 4.2) between the GNM and the end of LBM drainage, or waterflooding, is zero (Fig. 4.4).

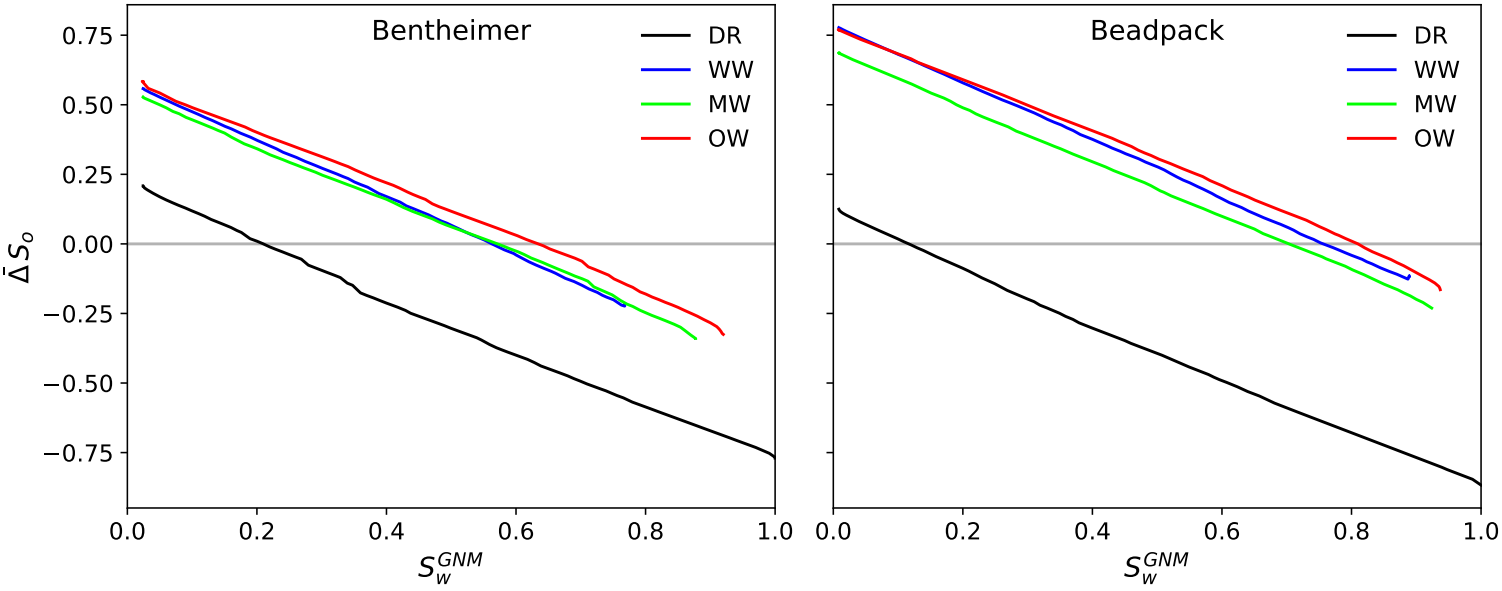

Figure 4.4: The method used to establish the comparison points between two models. Flow simulations of four regimes are compared: primary drainage (DR) and water-wet, mixed-wet and oil-wet waterflooding (WW, MW and OW, respectively). In each simulation, the total water saturation of the GNM network (S_w^{GNM}) is increased incrementally by 1%. At each saturation increment in the GNM, the mean difference in pore saturation of oil ($\bar{\Delta}S_o$) between the prevailing state of the GNM network and the end state of the LBM is calculated (Eq. 4.2). The total network saturations at which the two models are compared is given by the intersections of the lines with $\bar{\Delta}S_o = 0$ — for each wetting regime, the models are compared when their mean pore saturations are equal.

4.2 Results and Discussion

In Section 4.2.1 the GNM and LBM are quantitatively compared at the macroscopic scale, using the methods described in Section 4.1.3, to determine the average behaviour of each model. Experimental measurements of capillary pressure in Bentheimer (*Raeesi et al.*, 2014; *Lin et al.*, 2018, 2019) are also used to aid macroscopic comparison. Subsequently, in Section 4.2.2, the local differences between models are analysed using the methods described in Section 4.1.3.

4.2.1 Macroscopic Comparison

In the context of reservoir simulation, the two major upscaled flow-properties needed as an input into field-scale models are capillary pressure and relative permeability. Any modelling approach intended for practical use needs to accurately reproduce these properties. The focus here is on the former of these properties, as an analysis of relative permeability was not performed by *Akai et al.* (2020b). The wettability of the models is matched on a pore-by-pore basis; differences in P_c are due to representation of the pore-space geometry or the dynamics of the invasion. *Akai et al.* (2020b) compared their LBM results against a water-wet experiment by *Raeesi et al.* (2014), in which capillary pressure was measured using the porous-plate method. Their comparison showed good agreement with the experiment, slightly overpredicting drainage and underpredicting imbibition capillary pressure. A comparison between GNM, LBM and experimental capillary pressures – obtained with the porous plate (*Raeesi et al.*, 2014) and micro-CT image curvature measurement (*Lin et al.*, 2018, 2019) methods – is shown in Fig. 4.5.

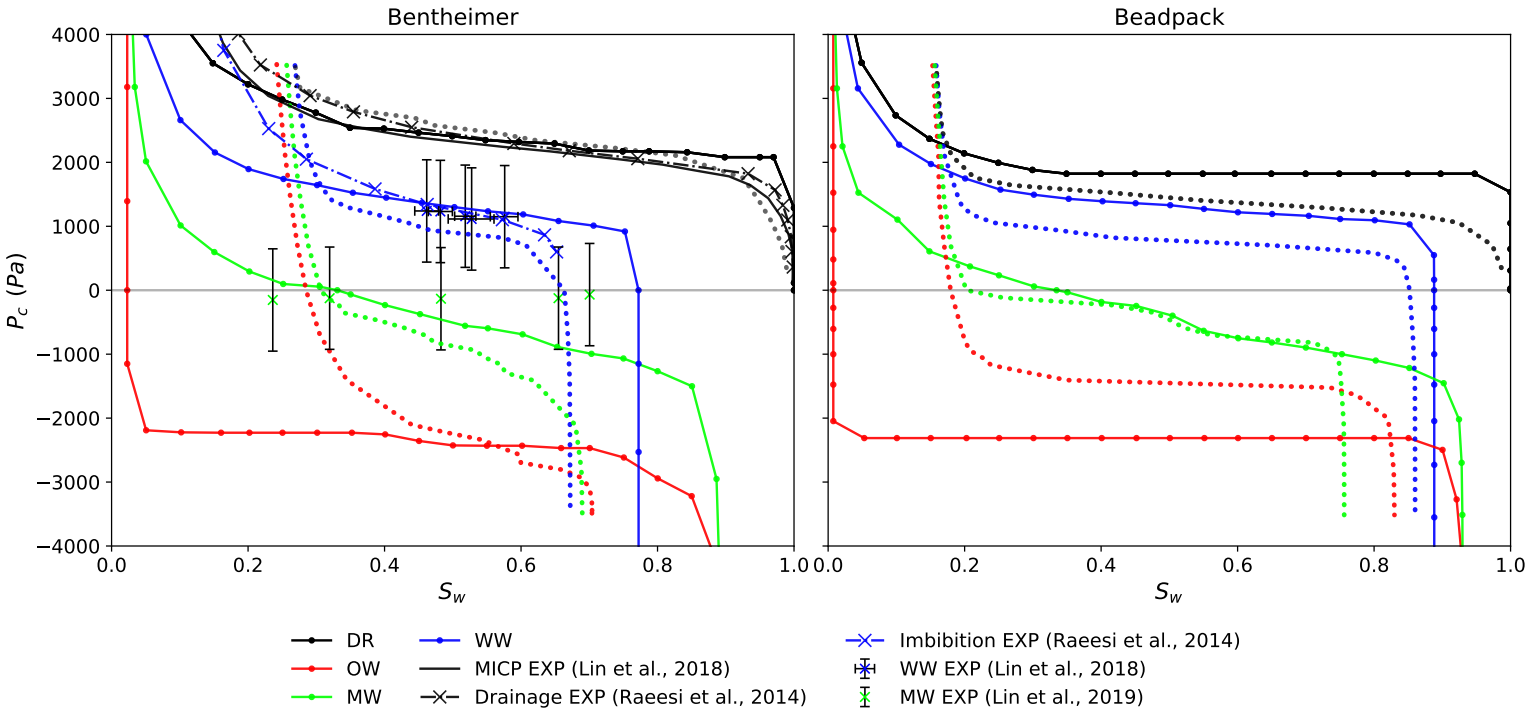

Figure 4.5: Capillary pressure (P_c) comparison between the LBM (dotted lines) and the GNM (solid with dots), for a beadpack and Bentheimer sandstone. In each plot, the colours distinguish primary drainage and water-wet, mixed-wet and oil-wet waterflooding (DR, WW, MW and OW, respectively). For the Benthiemer, experimental results (EXP) from *Raeesi et al.* (2014), *Lin et al.* (2018) and *Lin et al.* (2019) are superimposed with error bars indicating the uncertainty in the measurements (*Foroughi et al.*, 2020).

The LBM shows an initial water saturation (S_{wi}) after primary drainage of 27% and 16%, for Bentheimer and the beadpack respectively. Experimental observations, however, exhibit around $S_{wi} = 10\%$ for Bentheimer and $S_{wi} = 6 - 10\%$ for a packing of smooth beads (*Morrow*, 1970b), although the presence of surface roughness can reduce this to $S_{wi} = 1\%$ or less (*Dullien et al.*, 1989) — far lower than predicted by the LBM. In contrast, the GNM reaches lower S_{wi}'s than LBM — less than 5% in both samples — and better agrees with experimental findings. The cause of this discrepancy is the computational difficulty for LBM, and indeed all direct numerical simulations, to perform simulations at a resolution necessary to capture layer flow. Without wetting layers to sustain water-connectivity to the outlet throughout drainage, the wetting phase becomes surrounded and trapped.

The resolutions needed to capture layer flow (a minimum of three grid blocks) significantly increases simulation time, and the flow rates necessary to simulate layer flow may result in viscous-dominated behaviour. While high performance computing is extensively used in LBM

studies, providing the means to capture layers, each simulation still typically takes on the order of days to weeks to complete. For reference, each GNM drainage-waterflood cycle shown in Fig. 4.5 took 1 minute using a single core with a clockspeed of 2.30 GHz and a floating point operations per second (FLOPS) rating of 3.6 GFLOPS. In contrast, the LBM simulations — without layers — took on the order of two weeks using 128 cores with a clockspeed of 2.5 GHz and a numerical performance rating of 3.1 GFLOPS per core. This corresponds to approximately six orders of magnitude difference in computational time between the generalized network model and the LBM.

Due to these computational challenges associated with direct simulations, layer flow is often omitted from LBM studies, leading to an overestimation of trapped water saturation after primary drainage. It is important to emphasise that the remaining water is truly trapped — it is not connected to the outlet via wetting layers, as seen in experiments (*Lenormand et al.*, 1983; *Datta et al.*, 2014; *Andrew et al.*, 2015). In comparison, the generalized network model is able to simulate complete primary drainage; the wetting phase remaining in the network following drainage is rarely disconnected from the outlet as thin wetting layers maintain connectivity, even at very high capillary pressure, through the corners of the pore space. As layers are conceptually incorporated, rather than explicitly modelled, their inclusion comes at little extra computational cost and the resolution is the same as the precision of the hardware used for the simulation.

The oil-wet case in Fig. 4.5 shows large P_c discrepancy between the GNM and LBM predictions, in both the Bentheimer and beadpack, for the majority of the displacement. This is related to the inability of the LBM to reach low initial saturations at this resolution, as explained above. During drainage, oil preferentially invades the pore space in order of size, from largest to smallest, in accordance with growing capillary entry pressure (*Blunt*, 2017). The smallest regions of the pore space are the most difficult to invade — only a high capillary pressure can push the non-wetting phase into these regions. In the LBM, the wetting phase will never leave these regions. The non-wetting phase will find other, easier paths and leave the wetting phase trapped and disconnected in small crevices. Subsequently, an oil-wet wettability alteration occurs and water is injected, which has now replaced oil as the non-wetting phase. The pore

space is once again invaded in decreasing order of size. However, in the LBM, the smallest regions — those which require the highest water pressure, and hence the most negative capillary pressure — remain occupied with water. Thus the non-wetting phase (water) can span the system without displacing through narrow, high entry-pressure regions. In the GNM, this is not the case. The capillary pressure and connectivity necessary to fully drain the sample during primary drainage are achievable, resulting in the smallest regions of the pore space becoming occupied with the non-wetting phase. Subsequently, injected water must displace oil from these narrow regions if it is to span the system. The capillary pressure immediately reaches large, negative values to achieve this. The narrow range of pore-size distribution shown in Fig. 4.1 accounts for the flat capillary pressure throughout the remaining displacement — once the narrowest region is invaded, the non-wetting phase pressure is sufficient to percolate through the rest of the system.

The mixed-wet case in Fig. 4.5 reveals insights into the nature of displacement in both models. Both models show good agreement within $\sim 40-70\%$ water saturation, beyond which the impact of oil-layer flow becomes apparent, as discussed later. Indeed, for Bentheimer, both models lie within the uncertainty of experimental observations (*Lin et al.*, 2019) during intermediate saturations, with the GNM closer overall. However, the key observation highlighting the differences between the models lies in the early stages of displacement, $S_w < 40\%$. The LBM shows an almost vertical decrease to negative capillary pressure at the start of waterflooding — there is little spontaneous displacement and the invading phase must be forced into the pore space. From the contact angle distribution (Fig. 4.3) it is evident that there are water-wet regions of the pore space. Indeed, the GNM predicts significant spontaneous displacement at positive capillary pressures and spontaneous imbibition in mixed-wet samples has been experimentally observed (*Gao et al.*, 2020). The cause of this difference is again the absence of wetting layers connecting trapped water to the inlet at the end of drainage, mentioned previously.

Upon injection of water, wetting layers swell throughout the pore space until their arc menisci reach a critical radius of curvature, beyond which the narrowest, water-wet regions of the pore space are spontaneously filled. These narrow regions of the pore space can then act

as nucleation points for displacement in adjacent, less water-wet pores and throats. This is ordinary percolation invasion (*Blunt*, 2017). The LBM, however, is not able to access these water-wet regions of the pore space. Invasion must progress as invasion-percolation, in which elements are only invaded if they are connected to the inlet through the centre of the pore space. As much of the pore space in the mixed-wet case has experienced wettability alteration and displacement is invasion percolation-like, to form a connected pathway across the sample, oil-wet regions of the pore space must be invaded, causing the capillary pressure to become negative. The difference in percolation behaviour is evident from Fig. 4.6, which shows the contact angle of newly invaded regions as a function of saturation.

The contact angles in this study are known exactly and are spatially matched in both models (Fig. 4.2), allowing in-depth pore-by-pore analysis. Both models in Fig. 4.6 show general agreement in their average behaviour (solid lines), with more water-wet regions invaded before oil-wet; however the range of contact angles invaded is significantly different. For $S_w < 60\%$, the GNM predicts that displacement predominantly occurs in the more water-wet regions of the pore space, accounting for displacement at positive capillary pressure in the network model shown in Fig. 4.5. The most oil-wet regions are not invaded until the final stages, for water saturations above $\sim 60\%$.

In the LBM, however, the invading phase has no choice but to push through oil-wet regions as it cannot percolate into water-wet regions without a terminal menisci first reaching them, as shown by the immediate increase in the average contact angle invaded followed by a sharp drop shown in Fig. 4.6. This fluctuating behaviour is seen throughout the LBM simulations, and is most apparent in the Bentheimer sandstone due to its lower pore-space connectivity. In addition, the LBM exhibits a consistently higher invaded maximum contact angle until the final stages of waterlooding — the most oil-wet regions are always invaded, regardless of S_w, whereas these regions are bypassed in the GNM as favourable water-wet regions are accessible via wetting layers.

The apparent absence of ordinary percolation-like behaviour in the LBM could have important implications for future modelling of mixed-wet systems. While direct numerical simulations are undoubtedly successful for high resolution, physics-based studies of flow using massively

parallel processing, time and resource-efficient simulations with true predictive capability for mixed-wet systems — able to incorporate small-scale flow phenomena and the associated displacement phenomena on representative sample sizes — may be better suited to network modelling.

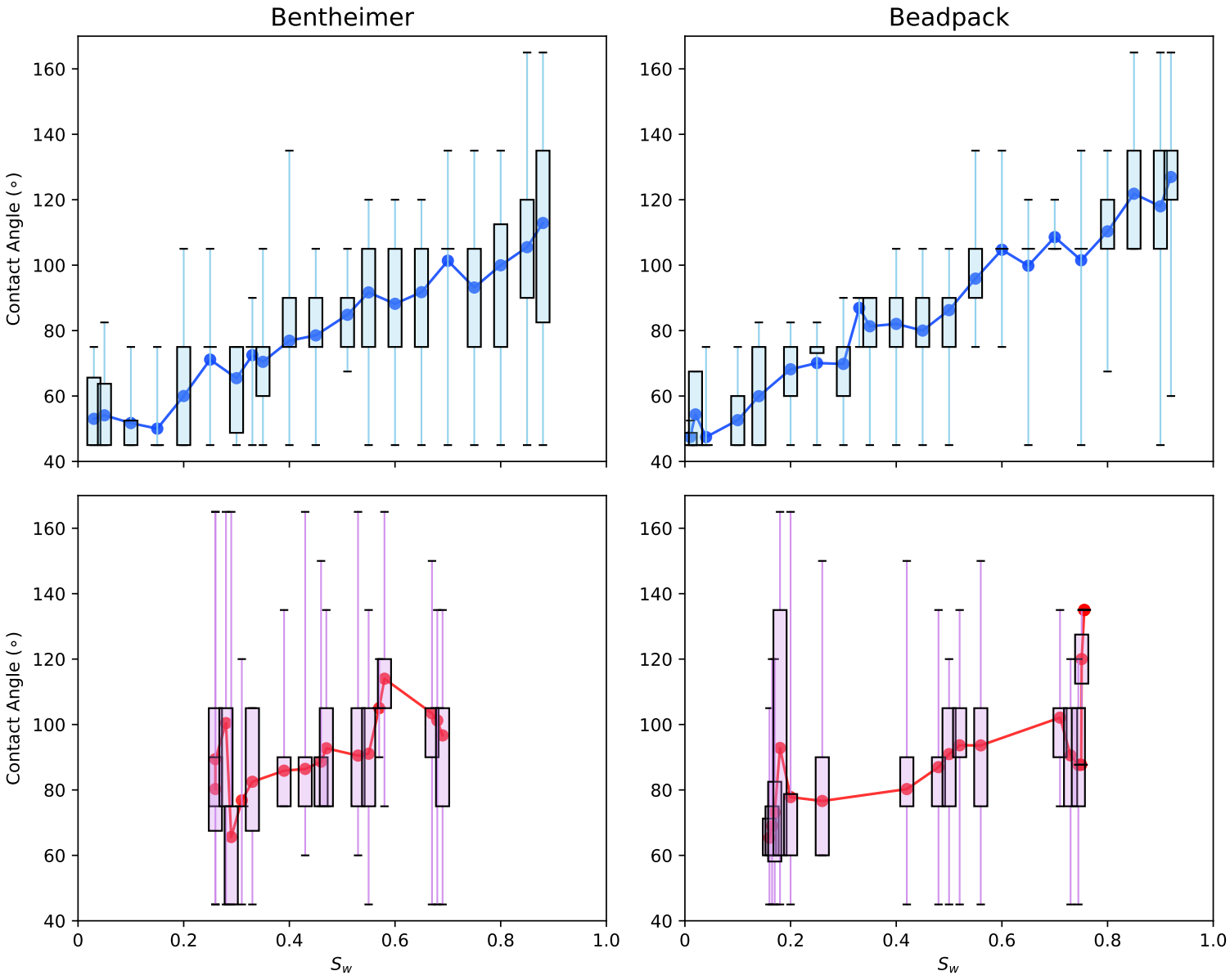

Figure 4.6: The contact angles of newly invaded elements during waterlooding in the mixed-wet case as a function of water saturation (S_w). The generalized network model is shown in blue in the top row, while the lattice-Boltzmann model is shown in red in the bottom row. In each figure, the boxes represent the interquartile range of contact angles invaded at each simulated saturation step, while the whiskers span the range of contact angles invaded. The solid lines represent the arithmetic-average of the invaded contact angles.

Thus far, the macroscopic comparison has highlighted differences caused by the absence of wetting layers in the LBM at the resolution of the simulations. However, wettability alteration can also cause the formation of oil layers in the corners of the pore space, as seen experimentally (*Singh et al.*, 2016). At the end of drainage, water is retained in the corners of the pore space and exists as wetting layers, while the solid surface bounding the centre of a pore region is contacted by oil and subject to wettability alteration (*Kovscek et al.*, 1993). During waterflooding, water (now the non-wetting phase) occupies the centre of the pore space and leaves oil as a stable layer between the water occupied corners and centre. These layers allow the oil to escape even if the centre of the pore space is blocked. The stability of oil layers is determined by the pore geometry and the initial water saturation — angular pore spaces with lower initial water saturation have thicker, stabler oil layers — but in general their existence allows altered wettability media to reach low residual oil saturations.

Figure 4.7 shows the residual saturations predicted by both models for both samples. The beadpack has a better connected pore space and shows lower residuals than Bentheimer, but the network model predicts far lower residuals than the LBM in both samples. The principal reason for this is the inclusion of oil-layer flow in the GNM. While it is true the GNM waterflooding simulations begin with a lower S_{wi}, and hence stable oil-layer flow throughout the simulation is expected, the impact of wettability alteration on residual oil is entirely missed by the LBM due to the computational constraints of modelling small-scale features with a resolution of $3.58\,\mu$m. In the beadpack, the LBM predicts minimum trapping of oil to occur for the water-wet case. Cooperative pore-body filling dominates in water-wet scenarios, leading to efficient sweep of the non-wetting phase out of the medium, and without the presence of wetting layers to facilitate snap-off there will be minimal trapping. For mixed-wet (without ordinary percolation) and oil-wet conditions, piston-like advance is dominant and the finger-like growth of the invading phase can trap large clusters of the defending phase in small regions. The manifestations of these displacement processes is not evident in the LBM Bentheimer predictions in Fig. 4.7 because the pore space is not as well connected — if a few key throats are invaded, the exit of oil will be blocked, while in the beadpack there will still be pathways to escape — and hence there is little variation in LBM Bentheimer

residuals as wettability changes from water-wet to mixed and oil-wet states. The GNM does capture the effect of oil-layer flow and the varying displacement dynamics, predicting that the residual oil saturation decreases with an increase in average contact angle, as seen experimentally (*Salathiel*, 1973; *Herring et al.*, 2016; *Alyafei and Blunt*, 2016). It is important to note that, while the LBM is a dynamic simulation, the average capillary number throughout the simulations was on the order of 10^{-5}. In addition, each capillary pressure increment was maintained until a capillary number of 10^{-6} was reached (*Akai et al.*, 2020b). These capillary numbers indicate that the majority of displacement in the LBM occurred in a capillary dominated regime, minimising the impact of viscous effects on residual saturations.

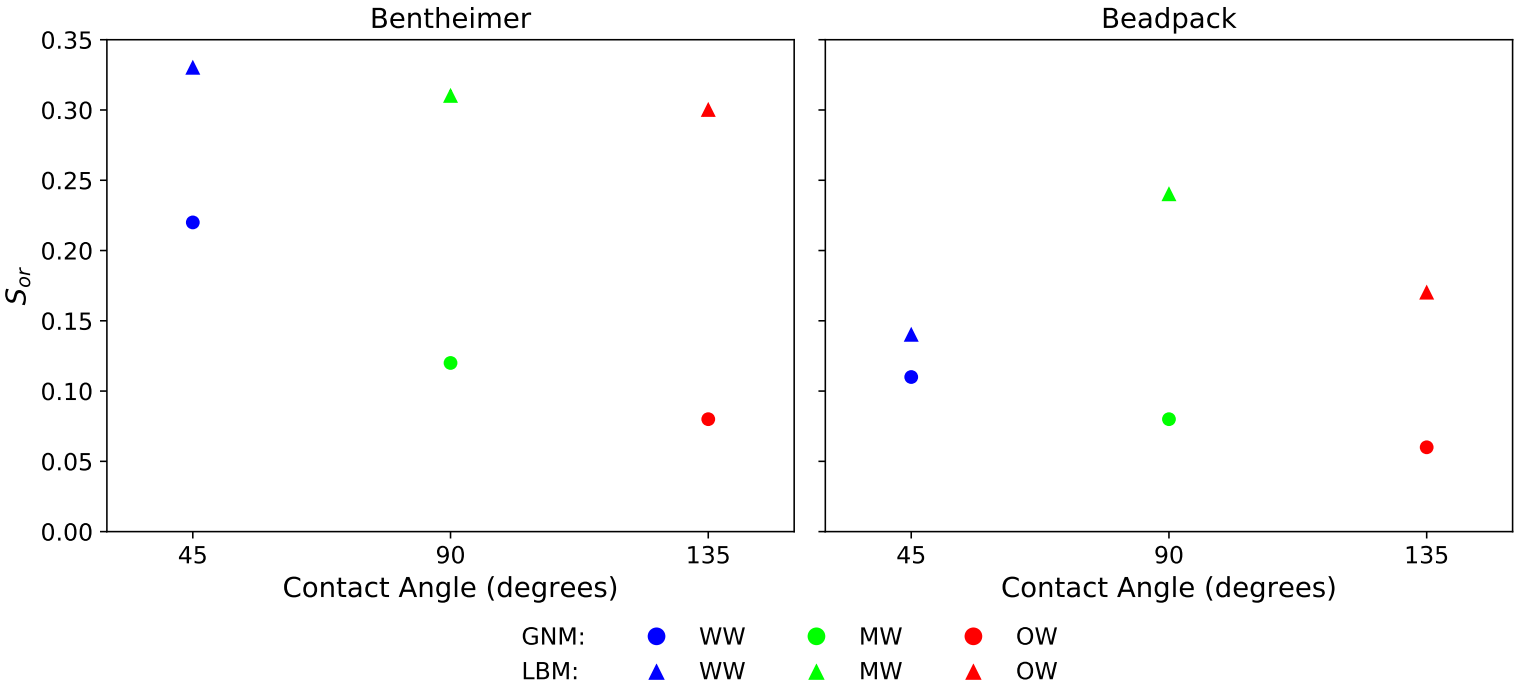

Figure 4.7: Residual oil saturations (S_{or}) after waterflooding predicted by the GNM (circles) and LBM (triangles) for the simulated water-wet, mixed-wet and oil-wet wettabilities (WW, MW and OW, respectively).

The inclusion of layer-flow has a clear impact on the nature of pore-scale displacement and the model predictions thus far, but at a macroscopic level it is useful to determine whether the models observe similar displacement sequences — that is, do the models predict the same fluid movement in the pore space. Despite the shortcomings of LBM, it is mathematically closer to a first-principles approach than network modelling and hence it is important to ensure the semi-analytic approximations present in the GNM reproduce the upscaled-behaviour of direct

methods. Figure 4.8 compares the Pearson correlation coefficients of radius with occupancy and oil saturation for both models, with the dotted blue line corresponding to an exact agreement. Both models indicate strong, positive correlation of occupancy and saturation with radius during drainage and water-wet waterflooding, as observed experimentally (*Roof*, 1970; *Scanziani et al.*, 2018; *Gao et al.*, 2020). Likewise, both models agree in the mixed-wet case where only a slight positive correlation in occupancy and saturation with inscribed radius is present, again as confirmed experimentally (*Scanziani et al.*, 2020; *Gao et al.*, 2020). Little correlation is expected as the volume-averaged contact angle is $90°$, with a range of contact angles above and below as shown in Fig. 4.3, and hence both imbibition and drainage are occurring simultaneously. Although small, the observation of positive coefficients in the mixed-wet cases can be explained as follows: during drainage, oil will occupy the largest regions of the pore space first. This will result in a positive correlation of saturation with radius at the end of primary drainage, as shown in Fig. 4.8. The degree of wettability alteration in both models is akin to that seen in experiments: pores highly saturated with oil experience stronger wettability alteration. Thus, at the beginning of waterflooding, large pores are occupied with oil and are more oil-wet than small pores, which retain more water and experience less alteration. It is almost always easier for water to invade the smaller, water-wet regions rather than the larger, oil-wet regions (Fig. 4.6) resulting in a positive correlation of oil-occupancy and saturation with radius. This behaviour has also been noted experimentally (*Rücker et al.*, 2020). In the oil-wet case, if the oil-wet state is considered analogous to drainage with the invading and receding phases swapped, a negative correlation of occupancy and saturation with radius is again self-explanatory and has been observed experimentally (*Alhosani et al.*, 2020b). In summary, Fig. 4.8 indicates that the GNM exhibits the same upscaled behaviour as the LBM and experiments.

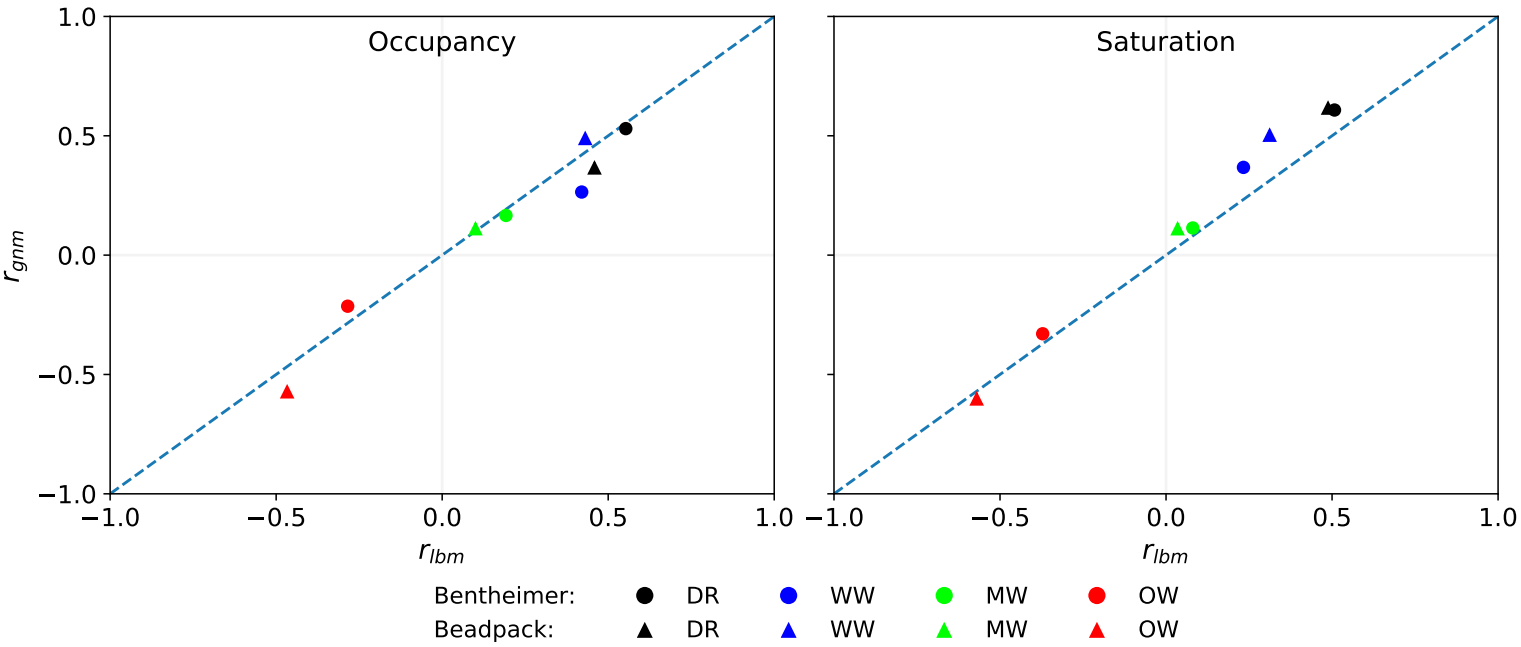

Figure 4.8: The Pearson correlation coefficients, r (Eq. 4.1), of occupancy and oil-saturation with radius as predicted by the GNM and LBM models after primary drainage and water-wet, mixed-wet and oil-wet waterflooding (DR, WW, MW and OW, respectively). Triangles and circles represent predictions for the beadpack and Bentheimer, respectively, and the colour of the data points corresponds to their wettability.

4.2.2 Pore-by-Pore Comparison

The pore-scale configuration and connectivity of fluids ultimately controls the upscaled macroscopic properties of interest to field-scale simulations. The exact pore-scale configuration of fluids is not even completely reproducible between repeat experiments on the same sample (*Raeini et al.*, 2019) — the mean and mean absolute difference for simple sandstones and carbonates can be as large as 8% and 17%, respectively. These pore-by-pore discrepancies therefore represent the closest agreement between model and experiment possible with the use of experimental constraints on input parameters. However, repeat experiments closely agree in upscaled properties and thus it is assumed that if the mean and mean absolute differences between model and experiment — or indeed two models — are similar to the discrepancy between repeat experiments, the upscaled properties should also be similar. For instance, the GNM showed moderate pore-by-pore agreement with water-wet experiments in both Bentheimer sandstone (*Andrew et al.*, 2014b; *Gao et al.*, 2017) and Ketton limestone (*Andrew et al.*, 2014b; *Singh et al.*, 2017), with a mean difference of $\sim 10\%$ and a mean

absolute difference of $\sim 30\%$ (*Raeini et al.*, 2019), while upscaled predictions agreed well with experimental measurements in water-wet Bentheimer (*Raeini et al.*, 2018; *Giudici et al.*, 2023b).

Figure 4.9 shows the mean difference in pore occupancy between the GNM and LBM as a function of wettability, while Fig. 4.10 shows the absolute difference in pore occupancy and saturation as a function of wettability, for both the Bentheimer and beadpack samples. The mean difference in saturation (not shown) is zero, as outlined in Fig. 4.4. To quantitatively assess the absolute differences between modelling approaches, a reference is needed. The expected absolute difference in oil saturation between two networks randomly saturated with a fraction, S_o, is given by (*Foroughi et al.*, 2020):

$$E\left(\left|\bar{\Delta}\right| S_o\right) = 2S_o(1 - S_o). \tag{4.4}$$

Equation 4.4 is used to normalise the absolute values of saturation obtained using Eq. 4.3. However, two identical media with the same mean saturation (Fig. 4.4) do not necessarily have the same occupied fraction, p. Thus, for two identical media A and B, the expected absolute difference in occupancy assuming random filling is given by:

$$E\left(\left|\bar{\Delta}\right| \alpha\right) = p_A(1 - p_B) + p_B(1 - p_A), \tag{4.5}$$

where p_A and p_B represent the fraction of occupied elements in A and B, respectively. The absolute differences in occupancy presented in Fig. 4.10 are normalised by Eq. 4.5.

The mean difference in pore occupancy shown by Fig. 4.9 is small and consistent with experimental comparisons. Physically, this means that the GNM predicts the average, upscaled occupancy to within 11% of both a higher fidelity LBM and experimental observations — all three approaches agree. It is evident that the mean differences are positive, which indicates that more of the pore space is occupied with oil in the GNM for any given water saturation. This is a direct manifestation of the nature of displacement in the two models: in the GNM, a change in saturation can arise from a change in volume of the wetting layers, leaving the occupancy unaltered. In the LBM, however, the absence of wetting layers results in pore

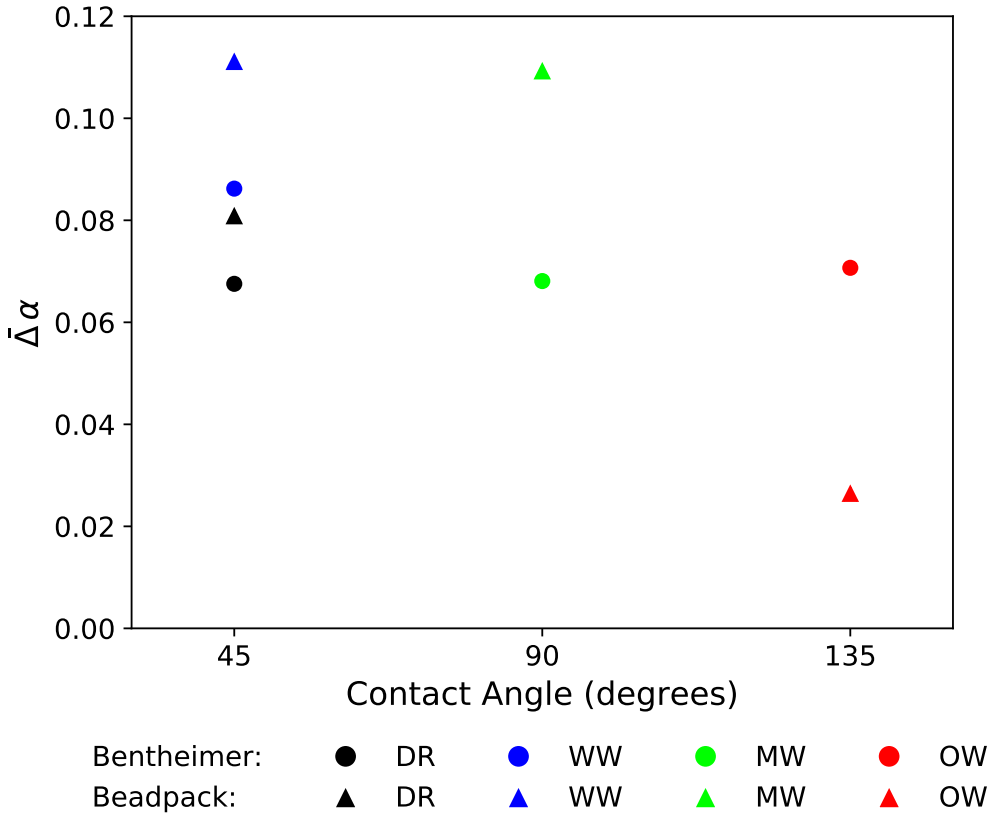

Figure 4.9: The mean difference (Eq. 4.2) in occupancy $\left(\bar{\Delta}\alpha\right)$ between the GNM and LBM for all simulations performed. The colours indicate wettability, while circles and triangles represent the Bentheimer and beadpack respectively.

occupancy accommodating saturation changes. This discrepancy in model behaviour is also shown in the mean absolute differences (Fig. 4.10), where there are a number of observations to note.

Firstly, the normalised mismatch in predictions decreases with increasing contact angle in both samples. This observation is due to the relative prevalence of ordinary percolation in combination with the order of filling, and is closely linked to the findings shown in Figs. 4.6 and 4.9: invasion is limited to invasion percolation in the LBM, and saturation changes cannot be attributed to wetting layers. In water-wet regimes, filling proceeds in order of increasing size in an ordinary percolation-like manner, while wetting layers are rarely pinned and can easily swell to allow an increase in wetting saturation before a change in occupancy occurs. The GNM can reproduce this behaviour, while the LBM is limited to piston-like displacement and cooperative pore-filling of regions that are directly connected to the inlet, and all saturation changes occur due to the complete filling of regions in the pore space. In

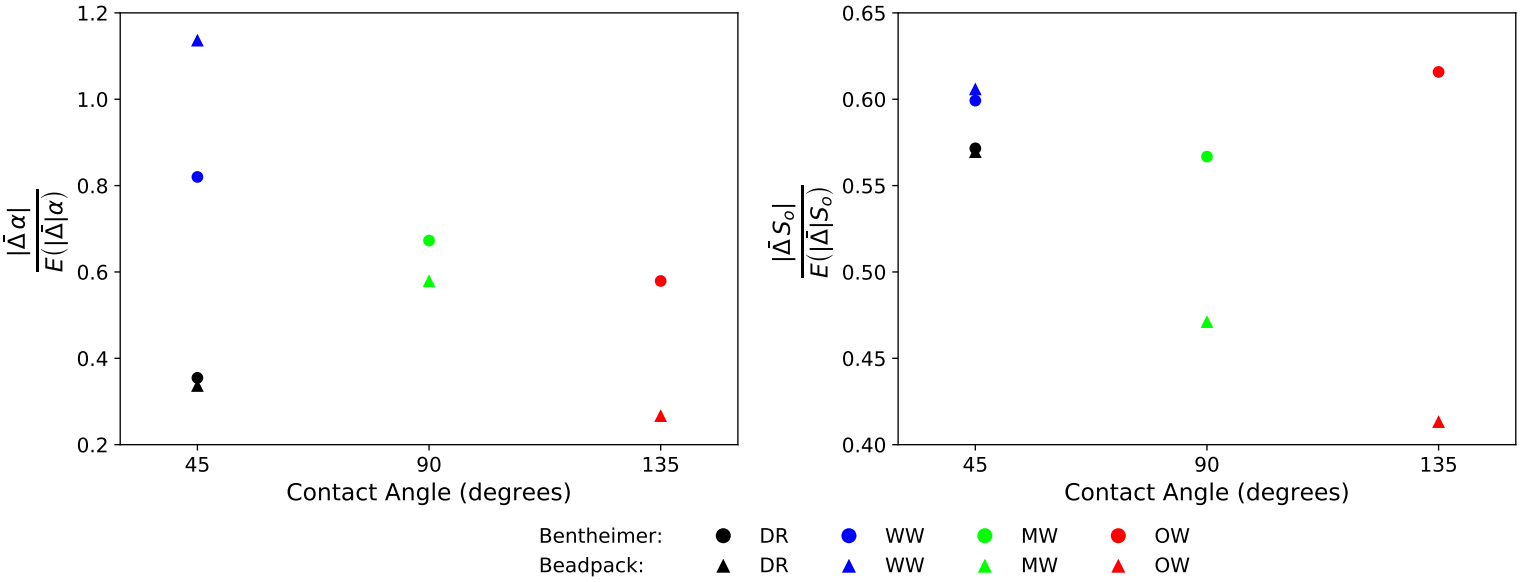

Figure 4.10: A comparison of the absolute differences (Eq. 4.3) in pore occupancy $\left(\left|\bar{\Delta}\right|\alpha\right)$ and pore oil-saturation$\left(\left|\bar{\Delta}\right|S_o\right)$ between models, normalised by the expected absolute differences (Eqs. 4.4 and 4.5), after primary drainage and water-wet, mixed-wet and oil-wet waterflooding (DR, WW, MW and OW, respectively). The circles and triangles represent the Bentheimer and beadpack samples, respectively.

addition, oil is preferentially retained in the largest regions of the pore space (Fig. 4.8), where discrepancies have the most significant contribution to volume-weighted absolute differences, further exacerbating the mismatch.

In the mixed-wet case, ordinary percolation still occurs in the water-wet regions, but is overall less prevalent than in the water-wet case; displacement in the oil-wet regions is controlled by simpler, invasion percolation-like behaviour. Furthermore, in the oil-wet regions of the GNM, wetting layers become pinned and cannot accommodate wetting-phase saturation increases as easily as in water-wet regions: changes in saturation are more likely due to a change in occupancy, as in the LBM, contributing to lower mismatch than in the water-wet cases. As the pore-by-pore contact angle is assigned based on the oil saturation after primary drainage, and oil saturation is positively correlated with radius (Fig. 4.8), it follows that the more predictable oil-wet regions account for the largest pores in the system and thus reduce the volume-weighted discrepancies shown in Fig. 4.10 further. This is explored in more depth in Fig. 4.11, discussed later.

In the oil-wet scenario, invasion percolation dominates, with filling purely in decreasing

order of size, and the two models exhibit lower mismatch because of this simpler behaviour, particularly in occupancy where the smallest pores are likely to remain occupied but have less contribution to volume-weighted differences. The exception to the observation of decreasing mismatch with wettability is the relative saturation mismatch for the oil-wet Bentheimer, which shows larger discrepancy due to the presence of oil-layers remaining stable in the angular pore space, whereas the less angular pore space of the beadpack is not conducive to their formation.

Secondly, the relative absolute discrepancies in predictions for the Bentheimer sample are generally larger than for the beadpack. This is an interesting finding: *Raeini et al.*'s (2019) comparisons of the GNM to experiments, and indeed uncertainty quantification between repeat experiments, showed higher mismatch in a Ketton sample (comparable in resolvable pore morphology to a beadpack) over a Bentheimer sandstone. Possible explanations for the greater disagreement in Bentheimer shown here could be that: i) there is a larger difference in S_{wi} between the GNM and LBM for Bentheimer; ii) the effective resolution is greater in the beadpack and iii) Bentheimer has a more angular pore space.

Initial water saturation has been shown to be a sensitive parameter in pore-by-pore predictions (*Raeini et al.*, 2019) and so it is expected that a larger difference in initial condition could result in larger differences toward the end of waterflooding, however the effect of this is mitigated to a certain extent through normalising by Eqs. 4.4 and 4.5 — Fig. 4.10 shows similar discrepancy for both samples at the end of drainage but large differences in discrepancy after waterflooding. Fig. 4.1, however, shows that the pores present in the beadpack are larger than in Bentheimer, and hence are better resolved for both the GNM and LBM, potentially reducing the disagreement for the beadpack. The one exception to this is the water-wet case, discussed previously, where the larger pores of the beadpack cause mismatches in the occupancy of the largest pores to yield greater volume-weighted absolute differences. Lastly, the narrower and more angular pore space of Bentheimer is also more conducive to the formation and preservation of layer flow, which as discussed earlier is not a feature present in LBM at this resolution. Although small, layers can lead to large pore-by-pore differences — one can envisage the effect of a critical throat, for example, which experiences snap-off and blocks a

flow path. Even without considering trapping phenomena, the presence of layers changes the saturation and entry pressures for any given element. The lower capillary pressures exhibited by the LBM in the water-wet cases of Fig. 4.5 are partly attributable to this. The above factors all impact the predictions of the displacement sequence throughout the waterflooding, and the relative importance of each cause requires future investigation.

Returning to the discussion of occupancy in mixed-wet states, previous studies have demonstrated that displacement is not purely governed by size in mixed-wet media — wettability is also a determining factor (*Lin et al.*, 2019; *Scanziani et al.*, 2020). The details of this, however, have not been fully explored. Figure 4.11 compares the Pearson correlation coefficient (Eq. 4.1) of pore occupancy with radius and contact angle for the mixed-wet state, when the mean difference in pore-saturation is zero (Fig. 4.4), for both samples. It is clear that contact angle, rather than radius, is the main control over whether a pore has remained occupied, as has been experimentally observed (*Scanziani et al.*, 2020; *Gao et al.*, 2020). The GNM predicts a larger correlation with contact angle in both samples, explained by Fig. 4.6 — ordinary percolation in the GNM can select water-wet regions, whereas the LBM cannot. Interestingly, the GNM predicts a stronger correlation of occupancy with contact angle in the beadpack over Bentheimer. This could be a feature of the topology of the two systems — with a higher coordination number, an invaded element in the beadpack could have more liberty to select surrounding water-wet pores to invade compared to Bentheimer. The extent to which topology controls the degree of occupancy correlation with local contact angle will be pursued in future studies.

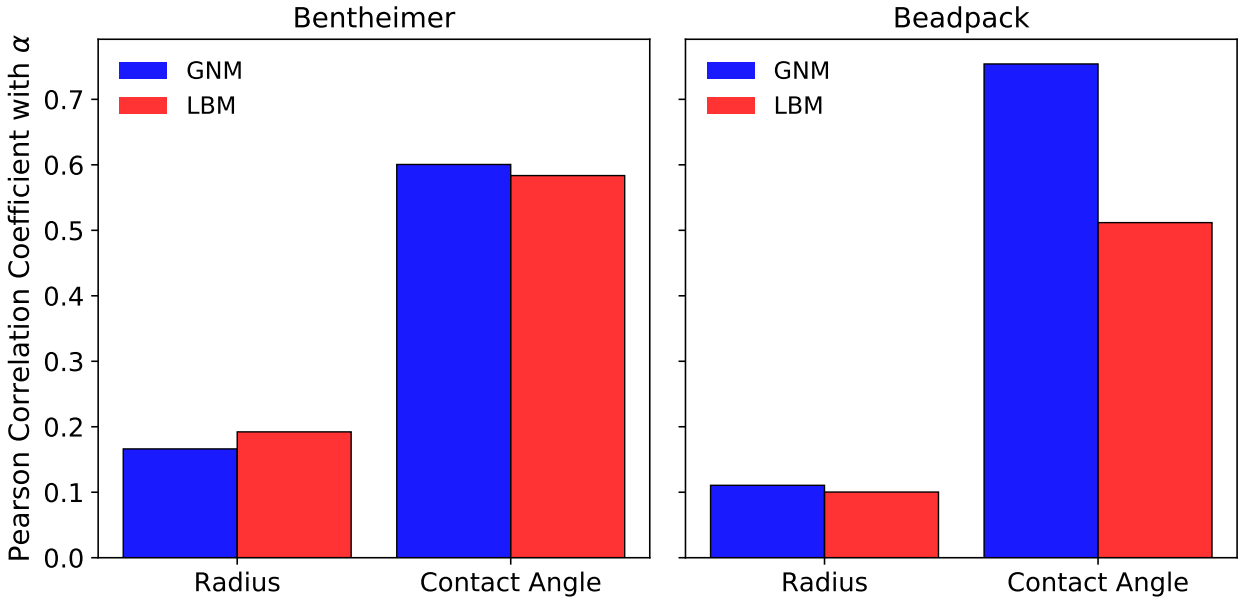

Figure 4.11: A comparison of the Pearson correlation (Eq. 4.1) of pore occupancy (α) with radius and contact angle, for both samples, for the mixed-wet simulations. GNM predictions are shown in blue while LBM predictions are in red.

Finally, it is noted that, for Bentheimer sandstone, the pore-by-pore mismatch between models is greater than the mismatch between repeat experiments (*Raeini et al.*, 2019). At first, this is an unexpected finding as the uncertainty in pore-by-pore wettability is removed from this study but is not reflected in the difference between models. However, semi-analytic approximations to flow and geometric approximations within the GNM are still present, and the initial water saturation at the end of drainage is also different between studies. Further, while wettability has been accounted for, discretisation limitations within the LBM prohibit the implementation of layer flow using commonly deployed hardware. Whether wetting layers or oil layers, these features are routinely incorporated into network modelling and their impact has been experimentally proven. It is likely that their absence in this work accounts for a significant portion of the difference shown here.

4.3 Conclusions

In this chapter, a workflow to compare pore-scale models of two-phase flow at both macroscopic and local scales is developed, implementing a spatial match in wettability. The method allows detailed insights into the pore-scale displacement and can be used to identify strengths

and shortcomings in predictive capability. The method was applied to analyse predictions obtained with a colour-gradient lattice-Boltzmann model and the generalized network model for two-phase flow in two samples, a synthetic beadpack and a micro-CT imaged Bentheimer sandstone, for four displacements: primary drainage and waterflooding under water-wet, mixed-wet and oil-wet conditions.

The comparison of macroscopic capillary pressure revealed good agreement between the two models, and experiments, at intermediate saturations but showed large discrepancies at the end-points. With a resolution of 10 grid blocks per average throat, LBM is unable to reach low initial water saturations due to the absence of layers, which manifests as further differences during waterflooding in altered-wetting states. Critically, at the resolutions typically implemented in research settings, the LBM does not capture displacement by ordinary percolation in a mixed-wet state. The absence of layers further impacts the residual oil-saturations, with the LBM predicting higher values than expected.

In contrast, the GNM was able to capture the effect of layer flow and its impacts since, while the geometry of the pore space is simplified, layer flow can be described with infinite resolution. The GNM exhibits spontaneous imbibition in mixed-wet displacement, and lower residuals in altered wetting states. The GNM predictions also agree more closely with experimental waterflood measurements. At a pore-by-pore level, absolute differences larger than between repeat experiments are observed, further emphasising that care must be taken when selecting pore-scale models. Overall, the comparison shows that network modelling is an attractive option for cost and time-effective prediction of two-phase flow.

However, it is clear from the macroscopic capillary pressure analysis that, while the GNM better matched mixed-wet experimental capillary pressure measurements, neither model replicated the substantial low-pressure displacement convincingly. In the network model, the reason for this inaccuracy is that the physical mechanism causing such displacement is unknown, and thus approximations of it cannot be made. In the next chapter, the union of wettability and geometry is applied to mixed-wet media to provide a physical explanation for low capillary pressure displacement.

CHAPTER 5

INTERFACE STABILITY AND DISPLACEMENT IN MIXED-WET MEDIA

5.1 Overview

In Chapter 3, the geometry of the pore space was seen to have a large impact on pore-scale displacement. Characterised by the angle β, the expansion and contraction of the solid walls significantly impacted the threshold capillary pressure for piston-like displacement. Together with wettability, β determined whether local displacement was a drainage or an imbibition process. Chapter 3 also revealed that the sagittal curvature of wetting layers plays an important role in relative permeability and residual trapping predictions, and the wetting layers themselves were shown to have a large impact on flow predictions in Chapter 4. Ultimately, the presence, nature and sagittal curvature of layers also depends on both the wettability and the geometry of the solid walls. In Chapter 4, the GNM predictions displayed moderate agreement with experimentally observed capillary pressures in mixed-wet media, but did not accurately capture low capillary-pressure displacement.

In this chapter, the interplay between the geometry and the wettability of the pore space is shown to be key in understanding displacement in mixed-wet media. A fundamental approach is taken: first, the pore-scale forces necessary to form the experimentally observed minimal surfaces are discussed. To recap, minimal surfaces have a zero total curvature (Fig. 1.10) and, consequently, zero capillary pressure. It is important to emphasise that a consideration of three-dimensional geometry means that minimal surfaces are not necessarily associated with a contact angle of 90° degrees, as implied by Eq. 3.1. As shown later, converging/diverging geometry and variable contact angles provide the conditions necessary for minimal surfaces to form.

Next, to test the theoretical predictions, a finite element method is used to produce stable minimal surfaces for a variety of wettabilities and synthetic geometries. Finally, stable interfaces are perturbed by increasing the pressure difference across the interface until displacement occurs, and an empirical relation between this threshold displacement pressure, the local wettability and the local geometry is obtained.

The outcome of this chapter is a greater understanding of the role that geometry plays in pore-scale phenomena, and a physically-based description for the low capillary pressure displacement observed in pore-scale experiments.

5.2 Pore-scale Forces

Before numerically simulating minimal surfaces, it is useful to lay a theoretical foundation. As discussed in Section 1.3.3, minimal surfaces are defined as having zero total curvature everywhere:

$$P_c = \sigma\kappa = \sigma\left(\frac{1}{r_1} + \frac{1}{r_2}\right) = 0. \tag{5.1}$$

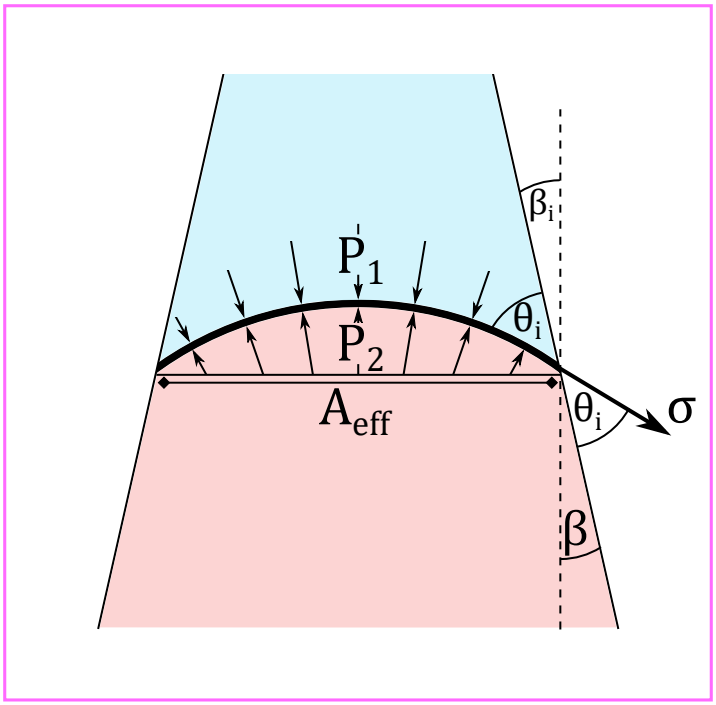

Figure 5.1: The coronal plane of the square capillary from Fig. 2.3. P_1 and P_2 are the receding and invading phase fluid pressures, respectively, and β_i and θ_i are the expansion and contact angle at the ith point on the three-phase contact loop, respectively. σ is the interfacial tension, while A_{eff} is the effective area of the fluid-fluid interface after it is projected onto the axial plane.

Consider the coronal plane of the capillary from Fig. 2.3B, re-presented above in Fig. 5.1. Following the same approach used to derive the equation for piston-like entry pressure in the GNM (Eq. 2.2), a vertical force balance on the interface yields the condition necessary for a minimal surface to form. For a contact loop experiencing n contact or expansion angles (whichever is greatest in number), a vertical force balance gives:

$$P_2 A_{eff} = P_1 A_{eff} + \sigma \sum_{i=1}^{n} L_i \cos(\theta_i + \beta_i), \tag{5.2}$$

where L_i is the contact length with the ith contact or expansion angle. Therefore, the condition for a minimal surface to form is:

$$\begin{aligned} P_2 - P_1 = P_c = \frac{\sigma}{A_{eff}} \sum_{i=1}^{n} L_i \cos(\theta_i + \beta_i) = 0, \\ \kappa = \frac{1}{A_{eff}} \sum_{i=1}^{n} L_i \cos(\theta_i + \beta_i) = 0, \\ \Rightarrow \sum_{i=1}^{n} L_i \cos(\theta_i + \beta_i) = 0. \end{aligned} \tag{5.3}$$

While a discrete form is more useful for pore-scale modelling, Eq. 5.3 is easily extended to continuous form, where $\mathbf{T}$ and $\hat{\mathbf{v}}$ represent the fluid-fluid interfacial tension and the unit vector in the vertical, respectively, and C is the closed contact loop:

$$\begin{aligned} \kappa = \frac{\oint_C \mathbf{T} \cdot \hat{\mathbf{v}}\, dl}{\int dA} = 0, \\ \Rightarrow \oint_C \mathbf{T} \cdot \hat{\mathbf{v}}\, dl = 0. \end{aligned} \tag{5.4}$$

From Eqs. 5.3 and 5.4, it is clear that an infinite set of contact lengths, contact angles and expansion angles can form a minimal surface. At present, obtaining even a single value of contact angle from a three-dimensional image is difficult (e.g, *AlRatrout et al.*, 2017; *Blunt et al.*, 2019; *Sun et al.*, 2020) – it is unlikely that image resolutions will increase sufficiently to identify multiple contact angles and their associated contact lengths along a contact loop. However, with some assumptions, progress can be made in understanding the fundamental behaviour of displacement in mixed-wet media.

In the remainder of this chapter, it is assumed that, locally, a maximum of two contact angles exist. Indeed, it is common in both modelling and experiments to assign or image clusters of the pore space which have different wettabilities (e.g, *Regaieg et al.*, 2023). Here, it is assumed that the pores and throats at the boundaries between these clusters will have two contact angles.

In three dimensions, these assumptions recast Eq. 5.3 to:

$$\sum_{i=1}^{n_1} L_i cos\left(\theta_1 + \beta_i\right) + \sum_{j=1}^{n_2} L_j cos\left(\theta_2 + \beta_j\right) = 0, \tag{5.5}$$

where n_1 and n_2 are the number of discrete expansion angles along the contact length of wetting regions 1 and 2, respectively.

In two dimensional systems, such as opposite plates, if the contact lengths with each contact angle are assumed equal, Eq. 5.5 can be simplified to:

$$\begin{aligned} Lcos\left(\theta_1+\beta_1\right)+Lcos\left(\theta_2+\beta_2\right)&=0,\\ \Rightarrow \cos\left(\frac{\theta_1+\beta_1+\theta_2+\beta_2}{2}\right)\cos\left(\frac{\theta_1+\beta_1-\theta_2-\beta_2}{2}\right)&=0,\\ \Rightarrow \theta_1+\theta_2&=\pi-\beta_1-\beta_2, \end{aligned} \tag{5.6}$$

where each contact line is further assumed to have a single expansion angle. Equation 5.6 leads to simple expressions predicting the onset of spontaneous imbibition in opposing plates: if $\theta_1+\theta_2<\pi-\beta_1-\beta_2$, the interface will spontaneously imbibe between the plates. Note that the expansion angles, while assumed constant over the contact lines, may change in space, i.e the opposing plates are not necessarily flat. This will become clear during the explanation of the numerical method and associated synthetic geometries in the following section.

In summary, this section has demonstrated that the sum of the interfacial forces acting on the three-phase contact loop must be zero for a minimal surface to form. The key insight, which will serve as a foundation for the remainder of this chapter, is that mathematically, the contact and expansion angles have equal precedence in all the above equations. This implies that predicting the stability and displacement of interfaces in mixed-wet media requires a consideration of both wettability and geometry, as shown in Chapter 3 concerning water-wet media.

In the next section, the numerical method used to simulate and displace minimal surfaces will be explained. The simulations will be performed on a variety of two and three dimensional synthetic geometries, deliberately chosen to follow on from the two- and three-dimensional theory presented above.

5.3 Surface Evolver and Synthetic Geometries

5.3.1 Surface Evolver

While many numerical methods exist for simulating pore-scale flow, few are specifically intended to find positions of equilibria. Surface Evolver (*Brakke*, 1992) is an open-source finite element model used to study fluid menisci shaped by interfacial tension. The user mathematically defines a geometry, a fluid interface and various associated constraints (e.g, pressure, volume and contact angle). Surface Evolver then tessellates the interface with triangular elements and evolves its shape according to the principle of least action. The result is a stable interface in its lowest energy configuration.

Key to the accuracy of Surface Evolver's predictions is correctly implementing the contact angle constraint. While contact angle can be explained through the concept of tensions acting on a three-phase contact loop (Fig.1.3), the physical origin of interfacial tension is the energy per unit area required to establish an interface between two phases. Thus, the total surface energy of a phase to be minimised is given by integrating the interfacial tension over the entire surface of that phase:

$$E_{tot} = \int \sigma \hat{\mathbf{n}} \cdot d\mathbf{S}. \tag{5.7}$$

It is possible for Surface Evolver to evaluate Eq. 5.7 over each solid-fluid interface in addition to the fluid-fluid interface, however this leads to numerical errors if the distance between the vertices of the tessellation becomes too small. Instead, the three-phase contact loop can be assigned an energy integrand that provides the same contact angle as if the solid-fluid interfaces were explicitly considered (*Brakke*, 1994). Stokes' theorem relates a surface integral to a line integral, which in the context of surface energy becomes:

$$\iint_S (\nabla \times \mathbf{F}) \cdot d\mathbf{S} = \oint_C \mathbf{F} \cdot d\mathbf{l}, \tag{5.8}$$

where $\mathbf{F}$ is a vector field to be determined and represents the component of fluid-fluid interfacial tension in the plane of the solid wall at an arbitrary vertex on the contact loop.

Mathematically, $\mathbf{F}$ can either by obtained by evaluating $\nabla \times \mathbf{F} = \sigma \cos(\theta) \cdot \hat{\mathbf{n}}$ directly – if $\hat{\mathbf{n}}$ is divergence free – or simply through inspection by finding a vector field that integrates to give the correct surface area of the desired geometry.

Once determined, $\mathbf{F}$ can be integrated around the contact loop at each simulation step, correctly accounting for the change in fluid-solid interfacial energy with displacements and giving the desired contact angle. In the following, the five geometries used to study the stability and displacement of mixed-wet interfaces are presented.

5.3.2 Synthetic Geometries and Assigned Wettabilities

Similar to the force balances presented in section 5.2 of this chapter, the geometries are deliberately chosen to increase in complexity. The reason for this is to build a foundational understanding, which can be difficult if three-dimensions are considered immediately.

This section first presents three two-dimensional geometries, followed by a quasi two-dimensional micromodel replicating the work of *Irannezhad et al.* (2023). Finally, a truly three-dimensional geometry is created. Each geometry will first be used to study the conditions for minimal surface stability, while the final, three-dimensional geometry will also be used to provide a physical explanation for low capillary pressure displacement in mixed-wet media.

The geometries are shown in Fig. 5.2. For each geometry, constant curvature interfaces subject to a variety of wettabilities are simulated (Table 5.1), illustrating the interplay between geometry and wettability. The energy integrand required to elicit wettability is listed for each geometry, while the derivation for each integrand is in Appendix C.

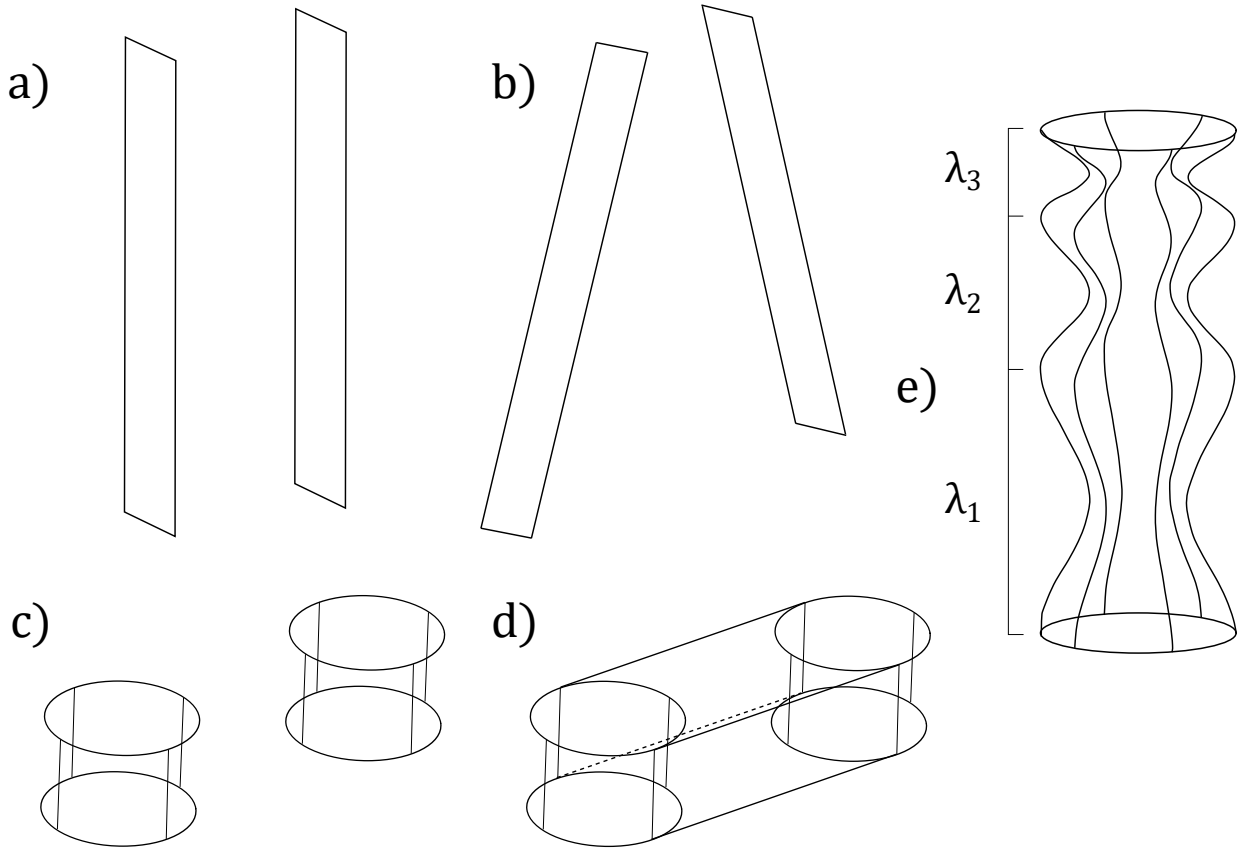

Figure 5.2: The five synthetic geometries used to study the stability and displacement of fluid interfaces. The parallel (a), inclined (b) and circular (c) plates are all two-dimensional systems eliciting a single principal curvature in the simulated fluid interfaces. The micromodel (d) is a quasi two-dimensional system: the left and right circular posts are bounded by flat upper and lower plates (*Irannezhad et al.*, 2023). Finally, a three-dimensional system is studied (e), which is constructed to have three different wavelengths along its height.

Table 5.1: A table to show the contact angle combinations assigned to each geometry. For each combination, Surface Evolver is used to produce a least-energy constant curvature interface.

	Two Dimensional						Quasi-Two Dimensional						Three Dimensional	
	Parallel Plates		Inclined Plates		Circular Plates		Micromodel						Sinusoidal Surface of Revolution	
	Left	Right	Left	Right	Left	Right	Left	Right	Upper	Lower	Left-half	Right-half	Left-half	Right-half
Contact Angle (°)	90	90	90	90	90	90	70	70	70	70	-	-	65	65
	140	40	110	110	45	45	70	70	110	110	-	-	45	45
	135	135	140	80	135	135	110	110	70	70	-	-	30	30
	135	90	140	140	60	120	-	-	-	-	80	100	110	70

Two-dimensional Geometries: Parallel, Inclined and Circular Plates

The first, and most simple, geometry to analyse is two parallel plates (Fig. 5.2a). Surprisingly, little work has investigated parallel plates with different wettabilities (e.g, *Bullard and Garboczi*, 2009). The first column of Table 5.1 shows the wettabilities assigned to each plate in this study.

The energy integrand **F** is given by:

$$\mathbf{F} = (1,0,0)\cdot z. \tag{5.9}$$

Next, inclined plates introduce a constant expansion angle, set to β=-20° here, into the analysis (Fig. 5.2b). The second column of Table 5.1 contains the wettabilities assigned to the inclined plates.

The energy integrand applicable to the inclined plates is:

$$\mathbf{F} = (1,0,0)\cdot \frac{z}{\cos(\beta)}, \tag{5.10}$$

where β is the inclination of the plates.

The final fully two-dimensional geometry considered is circular plates (Fig. 5.2c). Circular plates build upon the introduction of expansion angle with the inclined plates: on a circle, the expansion angle varies continuously between $[-\frac{\pi}{2}, \frac{\pi}{2}]$. The physical significance of this is that Surface Evolver will have a continuous range of β angles available to produce a stable minimal surface, rather than a single fixed value. Table 5.1, column three shows the assigned wettabilities.

The appropriate energy integrand for this geometry is:

$$\begin{gathered}\mathbf{F} = (1,0,0)\cdot g(z),\\ g(z) = \int_0^z \sqrt{1+\left(\frac{dy}{dz}\right)^2}\,dz = r_{plates}\left[\sin^{-1}\left(\frac{z-r_{plates}}{r_{plates}}\right)+\frac{\pi}{2}\right]\end{gathered} \tag{5.11}$$

where r_{plates} is the radius of the circular plates.

Quasi Two-dimensional Geometry: Micro-model

Here, the work of *Irannezhad et al.* (2023) is replicated. The geometry is quasi two-dimensional, with circular posts placed between flat upper and lower plates (Fig. 5.2d). The upper and lower plates introduce an additional, sagittal component to curvature which is absent in the truly two-dimensional geometries above. Each of the four walls has an assignable contact angle. Additionally, to replicate *Irannezhad et al.*'s (2023) experiments and simulations, the pore space is also divided into left and right halves, each with a single contact angle. The fourth column of Table 5.1 shows the combinations of contact angle used for this micromodel geometry.

For this geometry, two energy integrands are required – one for the circular posts, which is identical to Eq. 5.11, and another for the flat upper and lower plates:

$$\mathbf{F}_{flat} = (0, 1, 0) \cdot z. \tag{5.12}$$

Three-dimensional Geometry: Sinusoidal Capillary

The critical contribution of this analysis is that a truly three-dimensional geometry is studied. With the theoretical insight from Eq. 5.3 that pore-space expansion is equally important to wettability, it is useful to study a system that has variable ranges of β along its length.

To this end, a sinusoidal surface of revolution is constructed which has a length-dependent wavelength. The surface is defined by

$$x^2 + y^2 = R(z)^2, \tag{5.13}$$

where R is given as:

$$R(z) = \frac{R_p - R_t}{2} \cos\left(\frac{2\pi}{\lambda(z)} z\right) + \frac{R_p + R_t}{2}, \tag{5.14}$$

and the wavelength in micrometres, $\lambda(z)$, is a piecewise function of z:

$$\lambda(z) = \begin{cases} \frac{60\pi}{\sqrt{3}} & z \leq \frac{60\pi}{\sqrt{3}} \\ 20\pi & \frac{60\pi}{\sqrt{3}} < z \leq \frac{60\pi+20\pi\sqrt{3}}{\sqrt{3}} \\ \frac{20\pi}{\sqrt{3}} & z > \frac{60\pi+20\pi\sqrt{3}}{\sqrt{3}} \end{cases}. \tag{5.15}$$

The resulting geometry is displayed in Fig. 5.2c. The feature of interest in this geometry is the smoothly varying expansion angle. Considering only the y-z axis,

$$\frac{\partial y}{\partial z} = \tan(\beta(z)) = -\frac{\pi(R_p - R_t)}{\lambda(z)} \sin\left(\frac{2\pi}{\lambda(z)} z\right). \tag{5.16}$$

The pore and throat radii are initially set to 40 and 20 micrometres, respectively. These values, together with the wavelengths defined in Eq. 5.15, give the following ranges of expansion angles:

$$\beta(z) = \begin{cases} [-30°, 30°] & z \leq \frac{60\pi}{\sqrt{3}} \\ [-45°, 45°] & \frac{60\pi}{\sqrt{3}} < z \leq \frac{60\pi+20\pi\sqrt{3}}{\sqrt{3}} \\ [-60°, 60°] & z > \frac{60\pi+20\pi\sqrt{3}}{\sqrt{3}} \end{cases} \tag{5.17}$$

The sinusoidal geometry is divided into two by the plane $x = 0$, with the left and right halves assigned various combinations of contact angle shown in the final column of Table 5.1.

The energy integrand required for this geometry is given by determining an infinitesimal strip of a surface of revolution, equivalent to the height of the meniscus at a single vertex, and integrating around the contact loop:

$$\begin{aligned} \mathbf{F} &= \frac{1}{2\pi r^2}(-y, x, 0) \cdot g(z) \\ g(z) &= \int_0^z 2\pi R\sqrt{1 + (R')^2}\, dz. \end{aligned} \tag{5.18}$$

A full derivation of Eq. 5.18 is presented in Appendix C.

5.4 Results and Discussion

In section 5.4.1, each synthetic geometry and associated set of wettability combinations presented in Table. 5.1 is initialised with a fluid interface. The interface is then evolved to its equilibrium shape, which corresponds to the absolute minimum constant curvature interface possible, and qualitatively compared to theoretical predictions. Subsequently, in section 5.4.2, the three-dimensional sinusoid from section 5.3.2 is used to determine why displacement occurs at low capillary pressure in mixed-wet media. Finally, in section 5.4.3, the three-phase contact loop is studied to obtain an empirical relation between the geometry, wettability and threshold displacement capillary pressure.

5.4.1 Stability of Interfaces

Two-dimensional Geometries

In two dimensions, the only minimal surface possible is a flat plane. The first analysis is performed on parallel plates (Fig. 5.2a). From Eq. 5.6, the condition for forming a minimal surface between parallel plates is $\theta_1 + \theta_2 = \pi$. Mathematically, this is akin to showing that the shortest path between two points is a straight line: the sum of same-side angles on a straight line traversing two parallel lines is always π. Note that, while seemingly trivial, this immediately challenges a common misconception that flat interfaces only arise with 90° contact angles. Figures 5.3a and b show simulations for the first two contact angle pairs in Table 5.1. As predicted, the simulations show the least-energy configuration is indeed a flat meniscus. For any other contact combination (e.g, Figures 5.3c and d), the interface adopts a constant curvature as an arc of a circle.

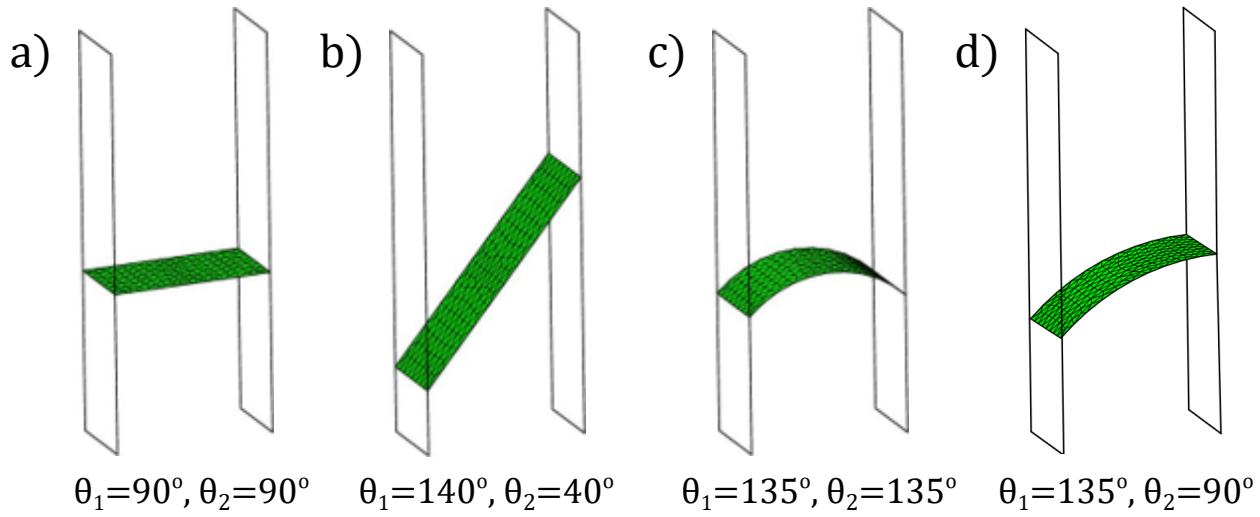

Figure 5.3: The least-energy constant curvature interfaces for four different combinations of contact angle in parallel plates. The left and right plates correspond to the contact angles θ_1 and θ_2, respectively.

Inclined plates (Fig. 5.2b) bring the expansion and contracting of the pore space into the analysis. From Eq. 5.6, the updated condition for forming a minimal surface between plates inclined at $\beta = -20°$ is given by $\theta_1 + \theta_2 = \pi + \frac{2\pi}{9}$. In degrees, the sum of the contact angles must equal $220°$. As shown in Fig. 5.4a, $90°$ contact angles are no longer conducive to the formation of a minimal surface – a constant curvature circular arc is instead the least-energy configuration. Figures 5.4b and c, however, do have assigned contact angles which sum to $220°$, and both form minimal surfaces. In Fig. 5.4d, the contact angles are once again unsatisfactory, and a constant curvature interface is produced. The essential observation, which will become even more apparent in the next example, is that the contact angles required to form a stable minimal surface depend on the pore-space geometry.

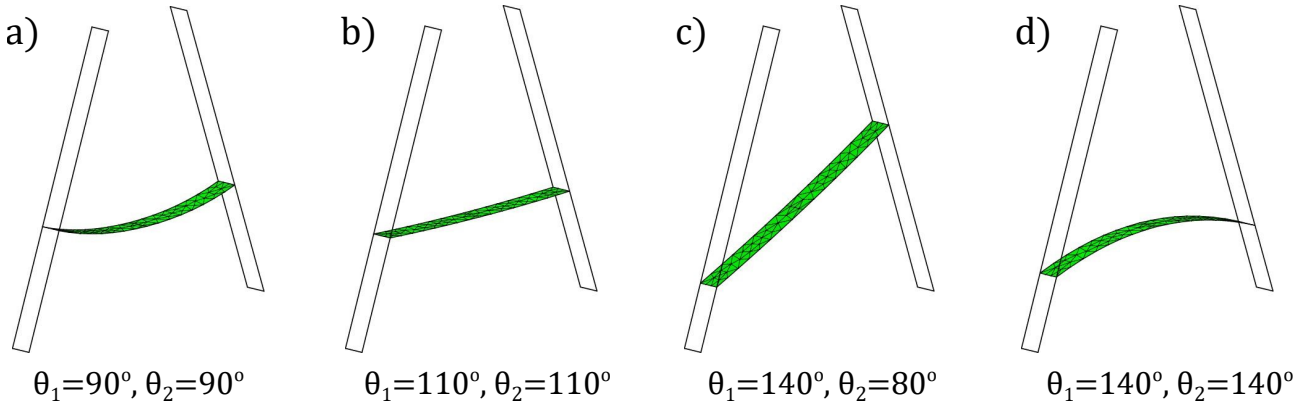

Figure 5.4: The least-energy interfaces for four different combinations of contact angle in inclined plates. Each plate is inclined from the vertical at an angle β=-20°. The left and right plates correspond to the contact angles θ_1 and θ_2, respectively.

Finally, the two-dimensional analysis concludes with circular plates (Fig. 5.2c). As explained previously, circular plates have a continuous range of $\beta = [-\frac{\pi}{2}, \frac{\pi}{2}]$. From Eq. 5.6, this suggests that any combination of contact angles can form a minimal surface, and indeed this is what Surface Evolver predicts. Figure 5.5 a,b,c and d show various different contact angle combinations, and yet each results in a stable minimal surface. This is because, in the fluid meniscus's efforts to minimise its surface area, the contact lines are free to move along the solid walls under the influence of the resultant interfacial forces. With a continuous range of β, there is always a position on the solid at which the resultant force balance will give a minimal surface. Circular plates thus exemplify the importance that geometry has: in the extreme, wettability does not matter at all to the formation of a minimal surface.

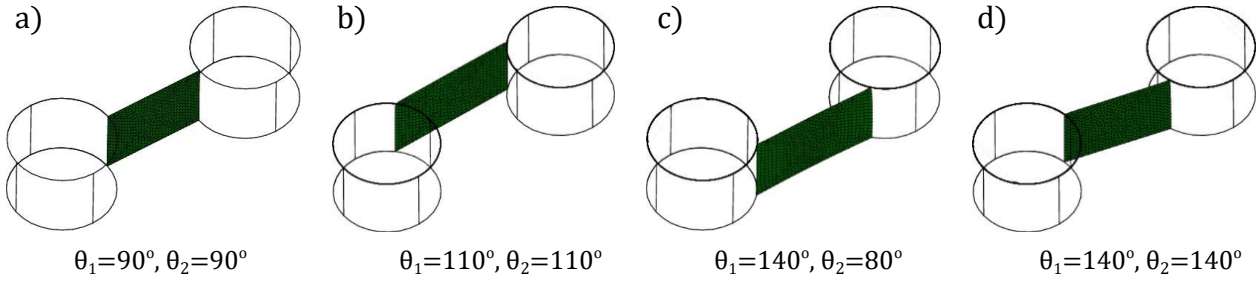

Figure 5.5: Stable minimal interfaces for four different combinations of contact angle in circular plates. The system is two-dimensional – the upper and lower edges of the interface are not in contact with a solid. The left and right plates correspond to the contact angles θ_1 and θ_2, respectively. As there is a continuous range of expansion angles, a minimal surface is always possible in circular plates.

Quasi Two-Dimensional Micromodel

With improved intuition from a two-dimensional analysis, the complexity of the system is increased by introducing three-dimensional effects. Physically, this corresponds to introducing the second principal component of curvature. Here, the micromodel (Fig. 5.2d) is termed quasi two-dimensional as the upper and lower plates are completely flat – their impact on the second principal curvature is constant, but not negligible.

The addition of the second principal curvature component leads to substantially more complex interfaces. As long as the total curvature across the surface is constant, the principal components can be different. An example often used for pedagogic purposes is the saddle minimal surface, which was shown in Fig. 1.10. The first three contact angle combinations for the micromodel in Table 5.1 are deliberately chosen to induce such an interface.

The first, and surprising, finding is shown in the weakly-water wet system in Fig. 5.6a. Despite each solid surface being assigned the same weakly-water wet contact angle, a saddle-shaped minimal surface is the least-energy configuration. This was first simulated in *Irannezhad et al.* (2023); here, explicit commentary on the phenomenon is provided.

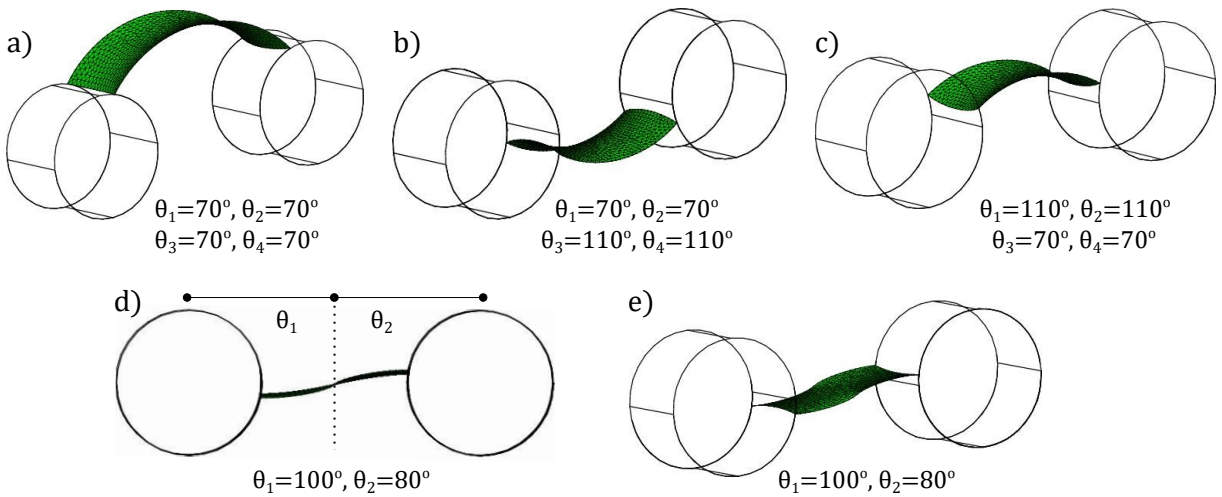

Figure 5.6: Stable miminal interfaces for four different combinations of contact angle in a synthetic micromodel. The left and right circular plates correspond to the contact angles θ_1 and θ_2, respectively. The upper and lower edges of the interface are in contact with a solid corresponding to the contact angles θ_3 and θ_4, respectively. In parts (d) and (e), the micromodel is divided in half, with θ_1 and θ_2 representing the wettability of the left and right halves, respectively. This latter configuration is a replication of *Irannezhad et al.* (2023).

Initially, opposing principal curvatures may seem counterintuitive in a uniformly-wet system – a uniform contact angle is commonly imagined as yielding interfaces with principal curvatures in the same direction. However, as in the two-dimensional analysis, the explanation centres on a force balance along the contact loop. On the upper and lower plates, the vertical component of interfacial tension results in a constant upwards pull, which cannot be mitigated by the geometry as the upper and lower plates are flat. This tends to move the interface upwards and is responsible for the positive curvature between the two flat plates. On the circular posts, however, there is a smooth change in β, as discussed previously for the two-dimensional circular plates. If a β exists such that the component of interfacial tension (multiplied by the contact length) on the circular posts can become sufficiently non-wetting, i.e $\theta + \beta > \frac{\pi}{2}$, then this can contribute the downwards pull on the contact loop needed to counterbalance the upward force from the upper and lower plates.

As Fig. 5.6a shows, this is indeed possible for weakly-wet media, and will likely be observed if fluid menisci in weakly water-wet micromodels are imaged in three-dimensions. Note that, from Eq. 5.5, the contact lengths are important for obtaining a force balance – this implies that the height and separation of the posts, which are geometric properties, also play a role in interface stability. A further remark is that minimal surfaces have negative Gaussian curvature. Experiments on water-wet geologic media have shown substantial numbers of interfaces with negative Gaussian curvature (e.g, *Lin et al.*, 2019; *Gao et al.*, 2020), whose origin has hitherto been suggested as wetting layers (*Gao et al.*, 2020). Based on the analysis here, it is plausible that some of these curvatures may originate from saddle-shaped terminal menisci.

Figures 5.6b and c further illustrate that numerous combinations of contact angles can induce a stable minimal surface if the geometry is compliant: Fig. 5.6b shows a situation where the flat upper and lower plates are non-wetting, which must be balanced by increasing the force contribution of the wetting contact lines by moving them toward more negative β. The opposite is shown in Fig. 5.6c where, to produce a minimal surface, the non-wetting components of tension must be enhanced by seeking positive β on the circular posts to counter-balance the wetting components on the flat plates.

Finally, the main finding of *Irannezhad et al.* (2023) is replicated in Figures 5.6d and e. Here,

the geometry is divided into left and right halves, with each having a separate wettability. This wettability assignment will be further explored in Section 5.4.2 for a three-dimensional geometry. The division produces 'S' shaped minimal surfaces when viewed from above. The two principal components of curvature vary significantly over the surface but always sum to zero. As seen in the previous geometries, the shape is explained by considering the contribution of the geometry to the balance of forces around the contact loop: the upward pull of the left, wetting side is reduced by moving the contact loop toward positive β on the left circular post, while the downward pull of the non-wetting side is reduced by seeking negative β on the right post.

Three-dimensional Sinusoid

The analysis of conditions necessary for forming stable minimal surfaces is concluded with the three-dimensional geometry in Fig. 5.2e. The aim here is to further consolidate understanding of the impact that pore-space geometry has, and to bridge the gap between stability and displacement, which will be discussed in the next section.

First, the least-energy configurations of three uniform allocations of wetting contact angle are simulated: $65°$, $45°$ and $35°$. These realisations are analogous to performing an imbibition simulation. From Eq. 5.3, the expansion angles necessary to form a stable minimal surface with these contact angles are $25°$, $45°$ and $55°$, respectively. As the geometry's wavelength is a function of its height, different regions hold the necessary β values needed, shown in Fig. 5.7. The equilibrium positions predicted by Surface Evolver exactly align with the theoretical expectations – in each case, the interface comes to rest at a position on the solid where the β value satisfies $\theta + \beta = \frac{\pi}{2}$.

Finally, the geometry is divided in half, and each half is assigned a different contact angle. The geometry is made mixed-wet, and the interface is evolved to a stable position. Figures 5.8a and b show the resultant minimal surface. As in section 5.4.1, the interface is 'S' shaped when viewed from the side (Fig. 5.8a), and has variable principal curvature component directions over its surface. However, hitherto, the interface and contact loop shape is relatively easy to predict: one simply finds a β value necessary to satisfy Eq. 5.6 for the chosen contact angles

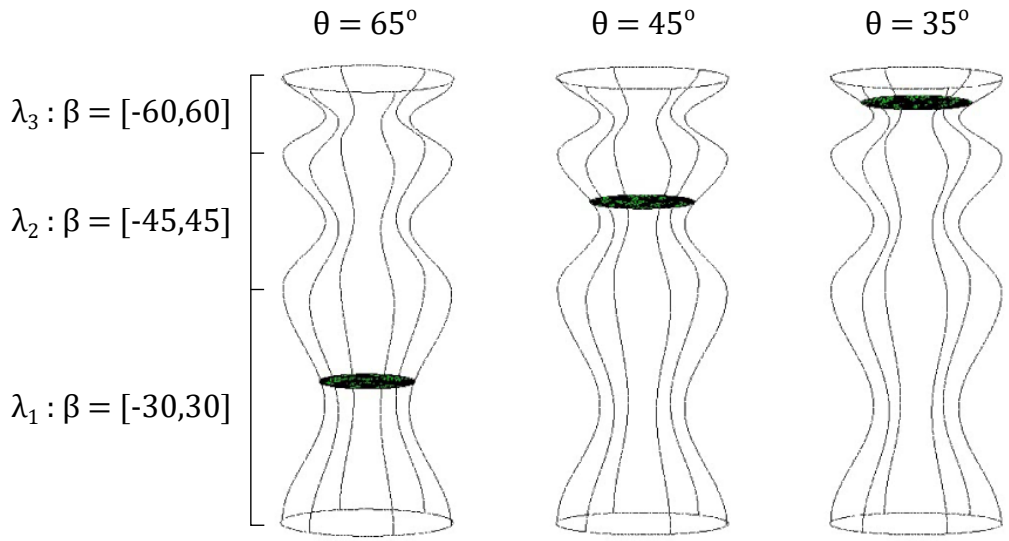

Figure 5.7: Simulations of three minimal surfaces in uniformly-wet systems. In each case, the assigned contact angle is displayed above the geometry. The geometry is deliberately constructed to have a variable wavelength, resulting in regions with different extrema of expansion angles, β, shown on the left. The minimal surfaces seek a position on the solid satisfying $\theta + \beta = \frac{\pi}{2}$.

and finds the position on the solid which has that β. The contact loop in this case is more complex, however, as it spans a continuous range of β values (Fig. 5.8b). This makes it difficult to predict the exact position on the solid that a minimal surface will be stable. To address this issue, the contact loop itself will be quantitatively analysed in the next section.

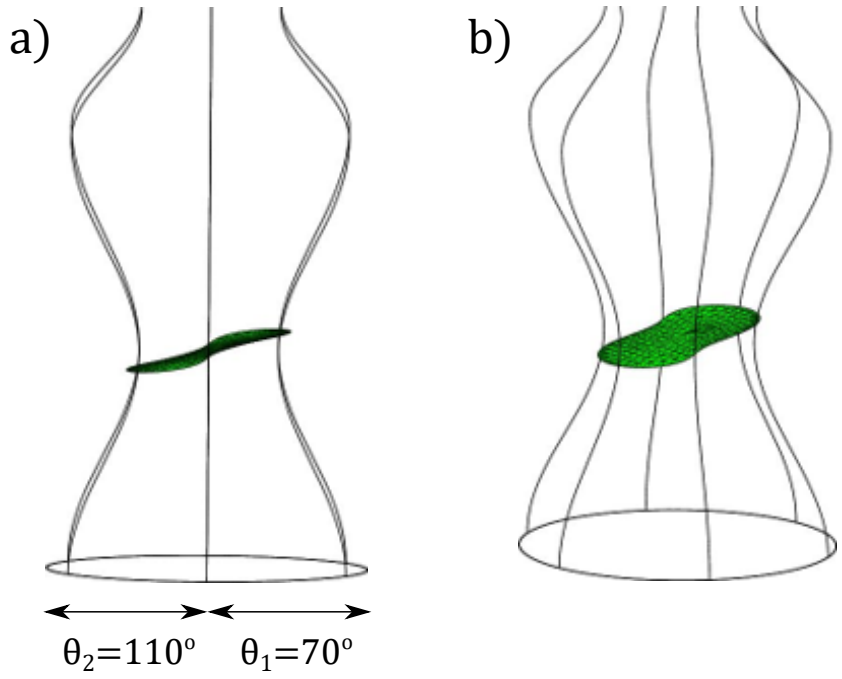

Figure 5.8: A simulated minimal surface in a mixed-wet system. In (a), the allocation of contact angle is shown: the geometry is divided in half, with the right contact angle $\theta_1 = 70°$ and the left $\theta_2 = 110°$. The resulting interface is elongated, has an 'S' shaped contact loop (a) and has a complex arrangement of principal curvatures across its surface (b).

In summary, this section has used increasingly complex geometries to systematically build a conceptual understanding of the interplay between geometry and wettability. The significant inference is that experimentally observed minimal surfaces are not purely wettability dependent. In reality, a combination of geometry and wettability dictate the stability of a minimal surface. Indeed, this conclusion is easily extended to equilibrium at non-zero capillary pressures too: at any pressure, finding a position of equilibrium depends on both geometry and wettability.

The main industrial interest in mixed-wet media, however, is how and why minimal surfaces lead to favourable displacement phenomena. One key aspect to understanding this is to determine why displacement in mixed-wet media occurs at low capillary pressure. The next section uses the intuition built in the analyses of stability above and addresses this question through a quantitative analysis of the contact loop.

5.4.2 Displacement of Interfaces

In the previous section, the stability of interfaces was shown to strongly depend on the geometry. In two and quasi two-dimensional geometries, where each post has the same wettability, the position required for stability was easily found from Eq. 5.6. However, dividing the geometry in half and assigning a different wettability to each half led to more complex interfaces in both the micromodel (Figures 5.6d and e) and the sinusoid (Figures 5.8a and b). In these cases, the interfaces are 'S' shaped, and there is no obvious single value of β. This phenomenon is important to understand as, in real mixed-wet systems, the pores and throats between wetting and non-wetting regions likely have a similar allocation of contact angle.

To understand mixed-wet interfaces further, the contact loop itself must be analysed. To do this, the first wavelength of the sinusoidal geometry in Fig. 5.2e is taken and an interface is initialised at $\frac{1}{4}th$ of the wavelength. Then, a minimal surface is evolved. The analysis begins with two simple cases: assigning a uniform wettability of $\theta = 90^{\circ}$ and another of $\theta = 70^{\circ}$. The interfaces in their least energy configurations are shown in Figures 5.9a and b.

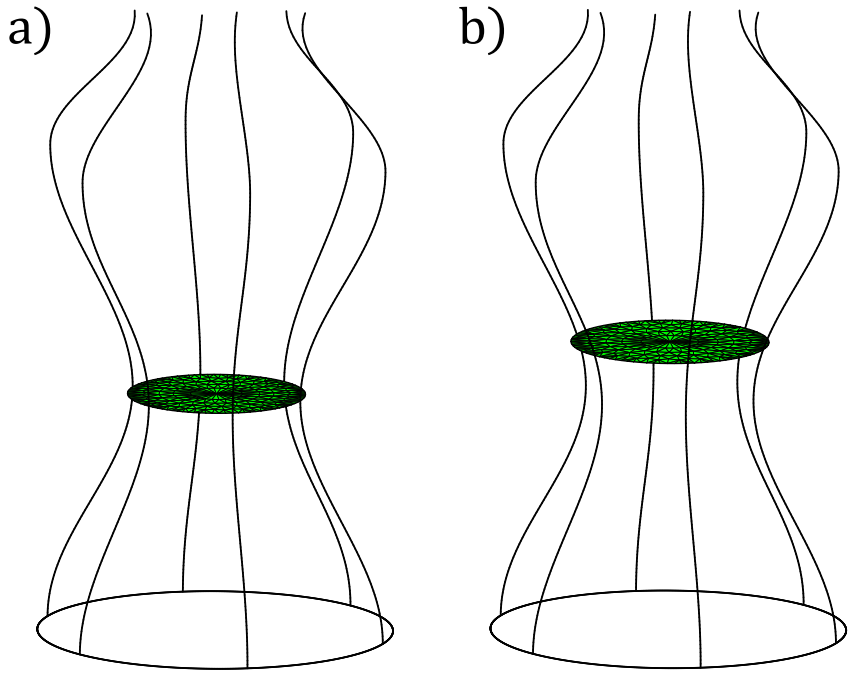

Figure 5.9: Simulated minimal surfaces in two uniformly-wet systems. In (a), the contact angle is 90°, while in (b) it is 70°. The 90° case clearly reached its equilibrium state a lower position in the sinusoid.

From Eq. 5.6, the β values required to produce a minimal surface for these contact angles are $0°$ and $20°$, respectively. Spatially, these β values correspond to the throat centre and slightly above the throat centre. As expected, Surface Evolver predicts this (Figures 5.9a and b). It is more useful, however, to describe the position of the contact line quantitatively. The interface can be projected onto the x-y plane, and each position on the contact loop can be assigned a unique angle α. This is possible as there cannot be two points on a contact loop with the same α – physically, this would be a discontinuity in the loop and is not consistent with a constant curvature interface. Additionally, as the geometry is symmetric, only the points on the contact loop between $\alpha = [\frac{-\pi}{2}, \frac{\pi}{2}]$ need be considered. After each point on the contact loop is assigned a location, α, the value of β at each point on the contact loop is also measured. Plotting α vs β for the two interfaces in Figures 5.9a and b, Figures 5.10a and b are obtained, respectively: Figure 5.10 provides quantitative confirmation of Eq. 5.6. The shape of the contact line in both cases is flat – every location around the contact line has the same value of β, and the $\theta = 70°$ geometry requires a larger value of β than the $\theta = 90°$ case. In this portion of the sinusoid, the maximum expansion angle of the solid is $\beta = 30°$, meaning that a uniform contact angle

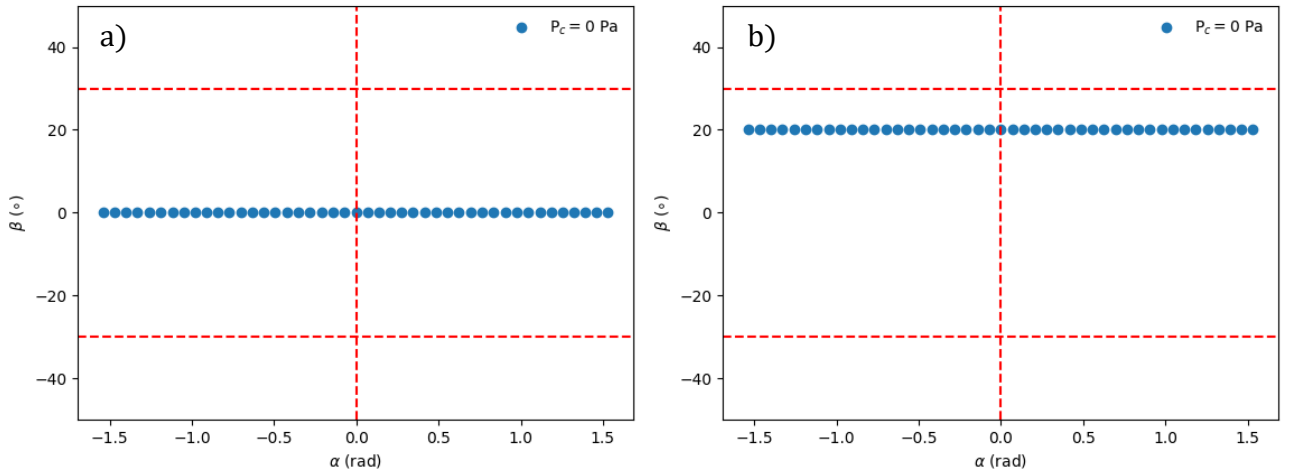

Figure 5.10: α-β plots showing the contact loops of two uniformly-wet systems at zero capillary pressure. In (a), the contact angle is 90°, while in (b) it is 70°. In both cases, the contact loop is flat. However, the 70° case requires a larger expansion angle, β, to form a stable minimal surface.

below $60°$ will not form a minimal surface.

The capillary pressure of the interfaces is now incrementally increased and the interfaces are evolved to their new position of equilibrium. For each new pressure, the contact line is projected and an α-β analysis performed, shown in Figures 5.11a and b. At each pressure increment in both geometries, the contact line remains flat but rises evenly to a new, larger expansion angle. The physical explanation is that, to counteract the increased upwards force exerted on the interfaces by the increased fluid pressure, the upwards vertical component of interfacial tension around the contact loop must be reduced by seeking a larger value of β. The maximum and minimum expansion angles possible are $\pm 30°$, shown by the horizontal red lines in Fig. 5.11; beyond this position, no stable configuration is possible and the interface displaces through the pore centre. Figure 5.11 shows that, in the $70°$ case, a smaller capillary pressure increase is needed to reach this critical position on the geometry and displace through the pore centre than in the $90°$ case. Intuitively, this makes sense; displacement in wetting regimes requires lower invading fluid pressure than in non-wetting regimes.

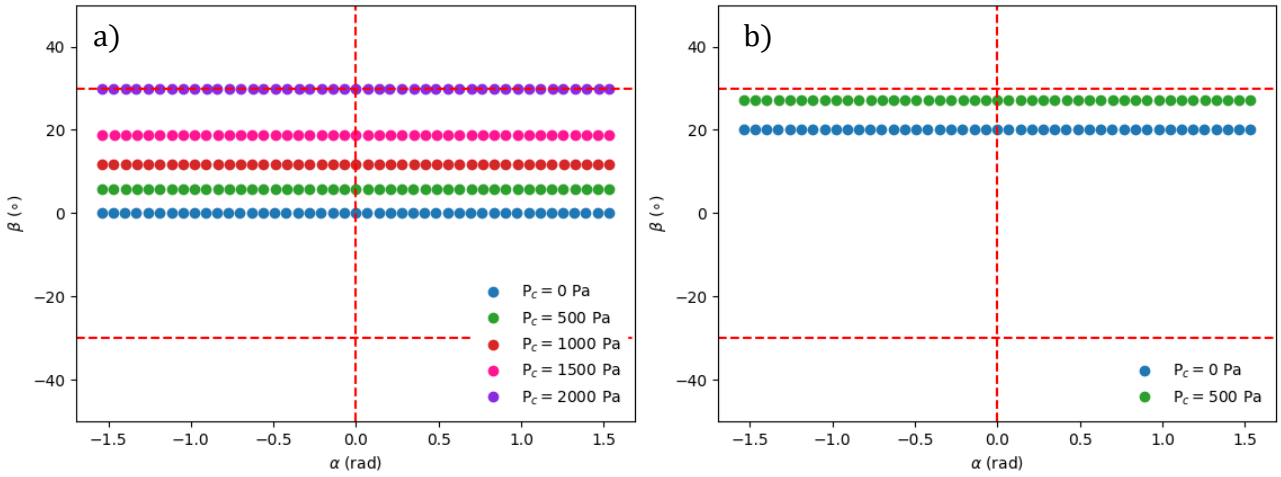

Figure 5.11: α-β plots showing the contact loops of two uniformly-wet systems at different capillary pressures. In (a), the contact angle is 90°, while in (b) it is 70°. In both cases, the contact loop is flat and rises uniformly with increasing capillary pressure. However, the 70° case requires a much smaller pressure increase to reach the critical displacement loop on the geometry, shown by the horizontal red lines.

Next, the α - β analysis above is repeated for a mixed-wet interface. The geometry is divided into left and right halves defined by y=0 – the left is weakly non-wetting at θ_2 = 110°, while the right is weakly wetting at θ_1 = 70°, resulting in a stable minimal surface shown in Fig. 5.8. Figure 5.12 shows the α-β plot for the stable mixed-wet minimal surface formed, along with the base case of a uniform contact angle θ = 90° for comparison. The visually observed 'S' shape of the interfaces in Fig. 5.8 is reflected in the α - β plots, but here a deeper analysis is possible.

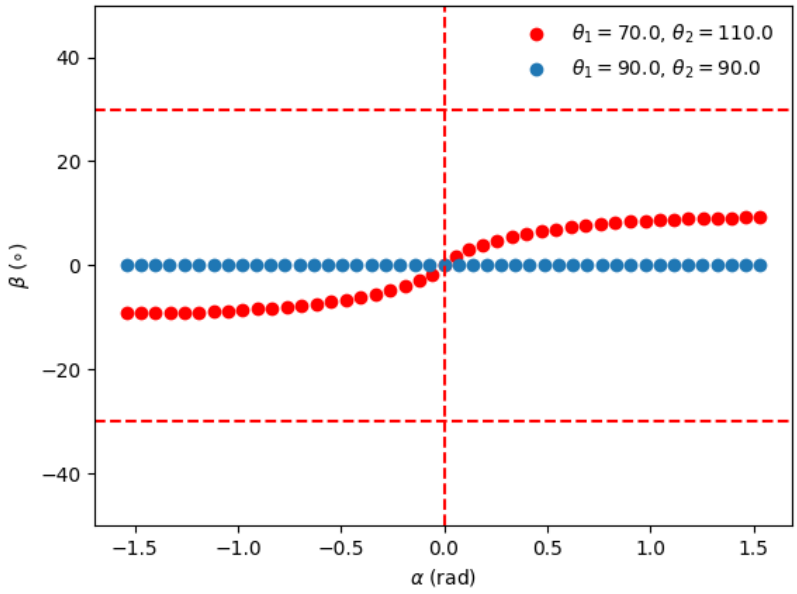

Figure 5.12: An α-β plot describing the difference between the contact loops of a mixed-wet system and a uniformly-wet system. The contact loop of the uniformly-wet system is flat, while the mixed-wet system is elongated, displaying a characteristic 'S' shape and reaching higher β values.

The first observation is that, in each half of the geometry, the contact loop does not reside at a single expansion angle satisfying $\theta = \frac{\pi}{2} - \beta$ for that half. This would result in a sharp discontinuity at the centre transition, inconsistent with capillary equilibrium. Instead, the contact loop varies smoothly between its highest and lowest points on the solid.

The second observation is that the maximum and minimum β values reached by the contact loop do not satisfy $\theta_1 + \theta_2 = \pi - \beta_1 - \beta_2$. The observed extremums of $\beta =\sim \pm 10°$ are half what is expected for the assigned contact angles. Physically, this is a result of the surface minimising its area: β increases with the radius of the pore space, meaning that, if the interface were to stretch between $\beta = \pm 20°$, the area of the interface would be larger than observed in Fig. 5.8. Instead, a force balance (Eq. 5.4) can be achieved with smaller perturbations to the contact loop resulting in a smaller fluid-fluid interface and an overall lower free energy (Eq. 1.4).

The final observation is that, despite the average contact angle for each case in Fig. 5.12 being 90°, the extremes of the contact loop around the mixed-wet interface are significantly closer to the critical loop on the geometry at which an interface becomes unstable. It was shown earlier in Fig. 5.11 that a change in capillary pressure corresponds to a vertical translation of the

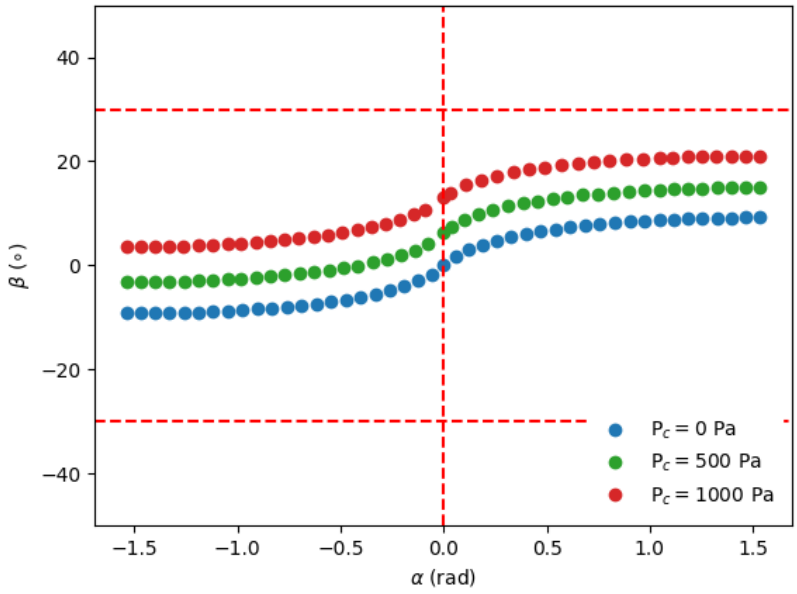

Figure 5.13: An α-β plot describing the contact loop of the mixed-wet system from Fig. 5.8. The capillary pressure is incrementally increased by 500 Pa until a stable interface is no longer possible.

contact loop on the α - β plots. The closer the initial position of the interface's contact loop to the critical displacement loop, the lower the capillary pressure necessary to displace through the pore centre. Figure 5.12 therefore explains why displacement occurs at a low capillary pressure in mixed-wet media: the contact loops are not flat, but instead elongated and require a much lower capillary pressure for the wetting side to reach the critical displacement loop. This is confirmed in Fig. 5.13, where the capillary pressure of the mixed-wet interface is increased until a stable interface is no longer possible. The displacement capillary pressure is approximately 50% lower than that of the uniform contact angle $\theta = 90°$. Increasing the difference between assigned contact angles in the mixed-wet system leads to a greater difference between maximum and minimum β values on the contact loop (Fig. 5.14a). This makes it even easier for the interface to move; the displacement capillary pressure decreases as the difference in contact angle increases. The average contact angle controls the position of the inflexion point - the inflexion point always satisfies Eq. 5.6 at a capillary pressure of zero (Fig. 5.14b).

In the next section, the analysis of mixed-wet contact loops with different combinations of contact angles shown in Fig. 5.14 is translated into an empirical expression which predicts

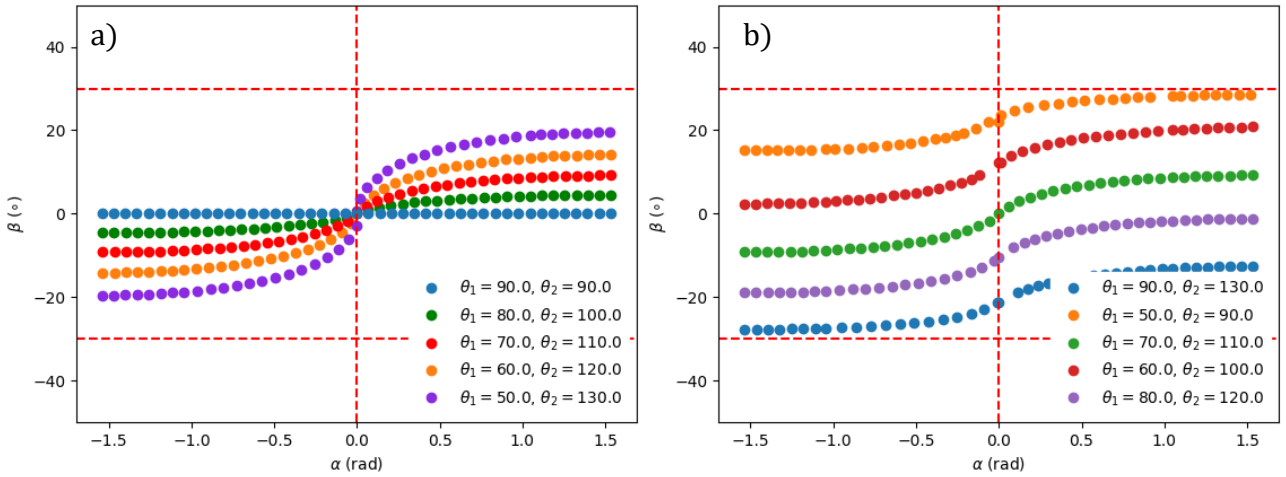

Figure 5.14: α-β plots showing the impact of changing the difference between contact angles (a) and the mean contact angle (b) on the contact loop of a minimal surface. Increasing the difference in contact angle elongates the interface, stretching it to higher expansion angles, while changing the mean value of contact angle controls the position of the interface's inflexion point.

their displacement capillary pressures.

5.4.3 Empirical Prediction

In this section, the insights gained from the preceding qualitative analysis are translated into an empirical relationship between capillary pressure and the maximum β value on the contact loop. In doing so, a method of predicting the threshold displacement pressure for a mixed-wet interface is provided. Consistent with the previous section, it is assumed that two contact angles exist, θ_1 and θ_2, each occupying half the pore cross-section.

From Figures 5.11, 5.14a and 5.14b, three deductions can be made: first, the difference in contact angle controls the amplitude, A, of the α-β plots, defined as the difference in β between the maximum/minimum values and the inflexion point; second, the average value of contact angle controls the β value of the inflexion point itself, according to Eq. 5.3; finally, changes in capillary pressure correspond to vertical translations of the contact loops in α-β plots. We propose that the value of β at any position α on the three-phase contact loop can be found empirically using a logistic-type function:

$$\beta = 2A\frac{1}{1+e^{-B\alpha}} + \frac{\pi-(\theta_1+\theta_2)}{2} - A + \delta\beta(\kappa). \tag{5.19}$$

The parameter B controls the gradient of the curve and is set to 1 in this work. The amplitude above the inflexion point is A and $\delta\beta(\kappa)$ is the vertical translation caused by capillary pressure. While optimising Eq. 5.19 to exactly match the shape of interfaces in α-β plots could provide an avenue for future research, it is not necessary for predicting the threshold displacement pressure. All that is needed is to obtain an expression for A and $\delta\beta$, which fully describe the maximum expansion angle, β_{max}, on the contact loop given by the logistic function:

$$\beta_{max} = A + \delta\beta(\kappa). \tag{5.20}$$

The form of the amplitude, A, was found to be a function of the wavelength, the difference in contact angles and pore radii, through a sensitivity analysis shown in Appendix D. Each property was systematically varied and the impact on A assessed, resulting in the empirical relation:

$$A\left(\Delta\theta, R_p, \lambda\right) = |\Delta\theta|^{e_1}\left(1 - \left(e_2\lambda\right)^{e_3}\right)\left(e_4 R_p\right)^{e_5}. \tag{5.21}$$

Throat radius was found to not significantly impact the amplitude. The coefficients e in Eq. 5.21 were determined numerically by simulating 1000 stable interfaces at zero capillary pressure, in sinusoidal geometries with random combinations of λ, R_p and $\Delta\theta = \theta_1 - \theta_2$, and numerically fitting a curve to the simulated amplitudes. The R^2 of the curve fit was 0.995, while the mean absolute relative error between predicted and observed amplitudes was 8% (Fig. 5.15).

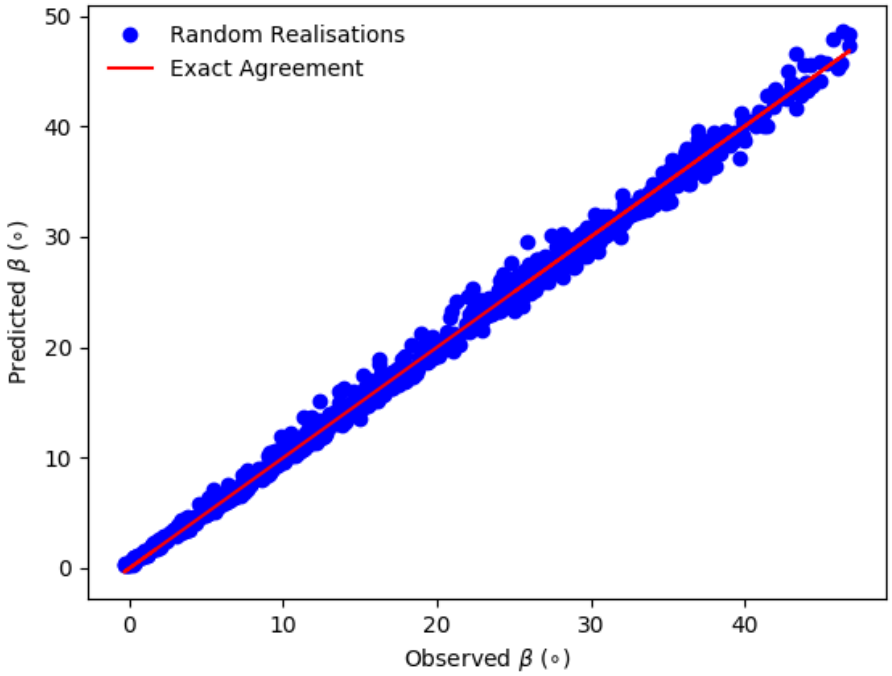

Figure 5.15: The agreement between empirically predicted and observed maximum expansion angles around the contact loop of 1000 minimal interfaces. The interfaces were generated in geometries with random pore radii, wavelength and mixed-wet contact angles with a mean of 90°.

The same approach used to determine the form of the amplitude was repeated for the perturbation, $\delta\beta$, shown in Appendix D:

$$\delta\beta(\kappa, R_p, \lambda, \Delta\theta) = m_1\kappa + m_2 R_p + m_3\lambda + m_4\Delta\theta \tag{5.22}$$

The coefficients m in Eq. 5.22 were obtained similarly: 1000 constant curvature interfaces were simulated with random capillary pressures, R_p, λ and $\Delta\theta$. Then, including the calibrated amplitude function $A(\Delta\theta, R_p, \lambda)$ found previously, the coefficients in $\delta\beta(\kappa, R_p, \lambda, \Delta\theta)$ were determined by optimising the predicted expansion angles from Eq. 5.20 against the simulated angles. The end result is shown in Fig. 5.16, which shows that Eq. 5.20 predicts the maximum β value required to form a stable interface in a sinusoidal geometry at an arbitrary capillary pressure with a mean relative error of 5% and an R^2 value of 0.976.

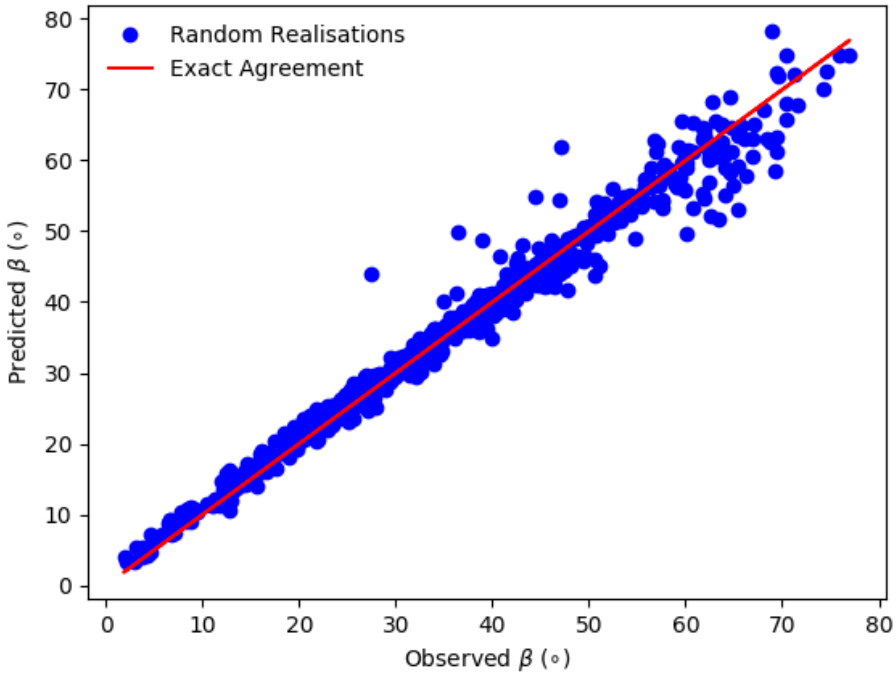

Figure 5.16: A comparison between empirically predicted and observed maximum expansion angles (β) around the contact loop of 1000 constant curvature interfaces. The interfaces were generated at random capillary pressures, pore radii, wavelength and mixed-wet contact angles.

Currently, a pore-network model capable of predicting mixed-wet low capillary pressure displacement through realistic three-dimensional media does not exist. Figure 5.16 shows that Eq. 5.20 predicts the maximum β value needed to produce a stable interface, at any capillary pressure, in the sinusoidal geometry. If the predicted β value is greater than what is available in the local geometry, the interface will displace through the region. Thus, Eq. 5.20 can be rearranged to provide the threshold displacement curvature at which an interface will displace through a pore:

$$\kappa = \frac{1}{m_1}\left(\beta_{max} - \left(A\left(\Delta\theta, R_p, \lambda\right) + m_2 R_p + m_3\lambda + m_4\Delta\theta\right)\right), \tag{5.23}$$

where β_{max} now represents the largest value of β present in a throat and A is defined previously (Eq. 5.21). The optimised coefficients e and m in Eqs. 5.21 and 5.22 are shown in Appendix D, Tables D.1 and D.2, respectively.

In summary, Eq. 5.23 can be included in a network model to more accurately predict threshold

displacement pressures in mixed-wet regions of the pore space. The principal new inputs required are the expansion angle β and the effective wavelength λ, which can be associated with the distance from pore to throat centres.

5.5 Conclusions

In this chapter, the pore-scale forces necessary to form experimentally observed minimal surfaces were presented. Then, a finite element model which finds the least-energy configuration of a fluid-fluid interface was used to explore the conditions in which stable minimal surfaces form in both uniformly-wet and mixed-wet media. A comprehensive set of simulations were performed in two-dimensional, quasi two-dimensional, and three-dimensional geometries to analyse the impact of pore-space geometry and wettability on interface stability. Finally, the displacement of interfaces was simulated in a three-dimensional geometry, and the analysis was extended through quantitative considerations of the three-phase contact-loop.

Hitherto, discussion of minimal surfaces in porous media has been restricted to the impact of wettability on their formation. However, fundamental considerations in this chapter have shown that, to form stable minimal surfaces, the only requirement is that the sum of interfacial forces acting on the contact loop of an interface must be zero. Importantly, this was shown to not only depend on the wettability of the solid, but also the morphology of the solid geometry. Simple expressions were derived which link the sum of contact and solid-wall expansion angles to the stability of a minimal surface. The key insight was that geometry and wettability take equal precedence mathematically, and thus predictions of stability and displacement of minimal – and indeed all – interfaces require a consideration of both parameters.

Finite element simulations confirmed the interplay between geometry and wettability in two-dimensional, quasi two-dimensional and three-dimensional geometries. In two dimensions, the only possible minimal interface is a flat plane, and the necessary wettability to produce such an interface is easy to predict: the sum of contact and expansion angles must equal π. In three dimensions, minimal interfaces were shown to take more complex forms resembling saddles or 'S' shapes, with varying principal curvatures over their surface. The contact length in each wetting region and the spatial arrangement of contact angles becomes important to

the overall shape of the interface. Interestingly, simulations on the quasi two-dimensional geometries revealed that characteristic saddle-shaped minimal surfaces are possible even in weakly-wetting conditions. Overall, minimal surfaces were shown to form in a much wider variety of wettabilities and geometries than previously expected.

Subsequently, the displacement of interfaces in three-dimensions was studied through a detailed analysis of the contact loop. It was shown that displacement occurs when the three-phase contact loop reaches a critical loop on the geometry. At this threshold, a force balance between the capillary pressure and the interfacial tensions acting around the contact loop is no longer possible. Due to the complex shape of the interfaces, the three-phase contact loop reaches this critical position on the geometry at lower pressure in mixed-wet media compared to uniformly-wet media. The interface moved further through the pore space along the more wetting surface, allowing the critical displacement loop to be reached with only a relatively small increment in capillary pressure. The shape of the three-phase contact loop was exploited to empirically relate the position on the solid wall to a logistic function, which accurately predicted the displacement capillary pressure in a sinusoidal mixed-wet capillary and can be included in pore-network models.

In summary, the main contribution of this chapter is a physical explanation for the sustained low capillary pressure displacement observed in mixed-wet experiments performed on both micromodels (e.g, *Irannezhad et al.*, 2023) and geologic media (e.g, *Lin et al.*, 2019). Achieving the balance of forces necessary to stabilise an interface in a mixed-wet region has been shown to depend on a delicate interplay between the contact angles present and the local geometry, leading to displacement at an absolute capillary pressure far smaller than expected from media with a significant fraction of oil-wet pore space, and smaller than a medium assigned a single average value of contact angle around 90°. This contribution can be incorporated and built upon in future modelling efforts to better capture experimentally observed displacement.

CHAPTER 6

SYNTHESIS AND FUTURE WORK

6.1 Synthesis

This thesis investigated the impact of wettability and pore-space geometry on capillary-dominated displacement. In particular, the focus has been on recognising porous media as a three-dimensional entity, and the analysis has considered the effect of this in the context of different wettabilities.

In Chapter 3, quasi two-dimensional approximations of threshold displacement pressures, which are standard in current network models, were extended to three dimensions. The new approximations are physically based, and were extensively calibrated using high-resolution direct simulations. The resulting improvements in predictions were substantial. For piston-like displacement, three-dimensional approximations can capture the apparent wettability of the system caused by the expansion and contraction of the pore space, while the former two-dimensional approaches cannot. Quantitatively, this can reduce the error in threshold displacement pressure predictions from over 20% to less than 5% when compared to direct methods.

For layer flow, the extended approximations accurately captured the suppression of snap-off caused by the expansion of the pore space at a throat. This decreased residual non-wetting saturations in water-wet systems by around 10%, in agreement with experiments, and significantly improved predictions of relative permeability. It also provides the missing physical consideration that had, until now, prevented network models from matching observations when using experimentally constrained input contact angles. Similarly, the sagittal curvature of layers significantly improved predictions of relative permeability.

In Chapter 4, the extended network model was compared to lattice-Boltzmann simulations for a wide range of wettabilities. Historically, little research has focused on comparing the two

approaches, and direct methods are often axiomatically assumed to more accurately capture the physics of multiphase flow. However, this thesis showed that direct methods struggle to capture the intricacies of displacement in complex wetting states at the REV scale. Wettability gives rise various displacement processes, many of which are intimately linked to fluid layers and their ability to maintain connectivity throughout the pore space. The resolutions required to capture this directly are prohibitive; network modelling, on the other hand, easily handles fluid layers. Additionally, Chapter 4 revealed that, while the generalized network model provided more physically accurate predictions than the lattice-Boltzmann method, it did not exactly reproduce the low-capillary pressure displacement observed in mixed-wet experiments. The principal reason for this was the lack of a physical explanation for such a phenomena.

Chapter 5 used the insight that pore-space geometry is crucial for correctly predicting displacement pressures, which was derived from Chapter 3, and applied it to mixed-wet media. First, a theoretical foundation was laid, providing an intuition on which geometries and wettabilities combine to facilitate stable minimal surfaces. Finite element modelling in two, quasi-two, and three dimensional geometries was then used to test the theoretical foundation, and to solidify the understanding of how geometry and wettability interact. It was shown that minimal surfaces are likely ubiquitous in any system at zero capillary pressure as, in three-dimensional systems, the expansion and contraction of the pore space can allow stable minimal interfaces in a wide range of wettabilities.

Chapter 5 then presented a quantitative analysis of the three-phase contact loop and its position on the geometry, both in uniform and mixed wettability scenarios. Through this analysis, a physical explanation for low capillary pressure displacement was discovered: locally, a critical loop exists on the solid, marking the final position where a stable interface is possible. Changes in capillary pressure correspond to the three-phase contact line moving along the geometry. If any point on the three-phase contact loop reaches this critical displacement loop, the interface becomes unstable and displaces. In mixed-wet media, the interfaces are elongated, and on the wetting side, the three-phase contact loop resides at higher expansion angles on the geometry compared to media uniformly wet with the average contact angle value of the mixed-wet system. Consequently, a smaller capillary pressure is required to reach

the critical displacement loop in mixed-wet media.

Finally, in Chapter 5, the analysis of the three-phase contact loop was used to establish an empirical relationship for predicting displacement capillary pressure in a synthetic sinusoidal geometry. This empirical equation, along with the newfound physical insight, can be integrated into network modelling to enhance predictions in mixed-wet systems.

6.2 Future Work

The following studies could be conducted to extend the research presented in this thesis:

- Chapter 3 showed the importance of considering pore-space expansion in pore-network modelling. A natural progression is to extract the pore-space expansion angles directly from a micro-CT image. This would remove the need for an empirical expression in Eq. 3.2 and improve the accuracy of predictions.

- While this thesis has primarily focused on capillary pressure, the impact of three-dimensional geometry on relative permeability should also be studied. Figure 3.11 in Chapter 3 showed appreciable wetting relative-permeability discrepancy with experiments at low saturations. Most of this is due to experimental uncertainty, as previously discussed, however conductivity correlations commonly used in network modelling have remained largely unchanged in nearly two decades. An important study is to perform direct simulations on a large number of small, three-dimensional subvolumes extracted from real images. Then, a data-driven method could be used to update the current two-dimensional conductivity correlations to three dimensions.

- Chapter 4 highlighted the strengths of network modelling for two-phase flow predictions. It is reasonable to suggest that future work should focus on using direct methods to calibrate network models, as in Chapter 3, rather than seeking ever-increasing computational power to reach accurate predictions in complex media and wetting states.

- Chapter 5 provided fundamental insights into the formation of minimal surfaces in porous media. An excellent project would be to perform experiments on a simple system,

such as a micromodel or a beadpack, where the geometry can be described analytically. The system should be made mixed-wet in a controllable fashion, and the resulting fluid-fluid interfaces should be compared to the analysis presented in this thesis.

- Chapter 5 also saw the introduction of an empirical equation to predict displacement capillary pressure in mixed-wet media. While the equation provided satisfactory predictions in a simple sinusoid, future work should seek to extend this analysis to more complex geometries with corners. A possibility is to perform the analysis on subvolumes of real media, however the analytic nature of Surface Evolver could make this difficult. Simple geometries, such as squares and triangles, could be more feasible. The empirical equation should also be included into a network model, and its impact on predictions assessed.

- In the analysis of mixed-wet interfaces, Chapter 5 saw the use of a force balance around the contact line to predict which conditions would form a minimal surface. However, the exact shape of this minimal surface remains unknown – the total curvature must be constant, however the principal components of curvature at each point on the surface have no known constraints. A fascinating avenue would be to approach this topic from a differential geometer's perspective and attempt to derive a partial differential equation describing the surface.

BIBLIOGRAPHY

Akai, T., B. Bijeljic, and M. J. Blunt (2018), Wetting boundary condition for the color-gradient lattice Boltzmann method: Validation with analytical and experimental data, *Advances in Water Resources*, *116*(April), 56–66, doi:https://doi.org/10.1016/j.advwatres.2018.03.014.

Akai, T., M. J. Blunt, and B. Bijeljic (2020a), Pore-scale numerical simulation of low salinity water flooding using the lattice Boltzmann method, *Journal of Colloid and Interface Science*, *566*, 444–453.

Akai, T., Q. Lin, B. Bijeljic, and M. J. Blunt (2020b), Using energy balance to determine pore-scale wettability, *Journal of Colloid and Interface Science*, *576*, 486–495, doi:https://doi.org/10.1016/j.jcis.2020.03.074.

Alhammadi, A. M., A. AlRatrout, K. Singh, B. Bijeljic, and M. J. Blunt (2017), In situ characterization of mixed-wettability in a reservoir rock at subsurface conditions, *Scientific Reports*, *7*(1), 1–9.

Alhosani, A., A. Scanziani, Q. Lin, A. Q. Raeini, B. Bijeljic, and M. J. Blunt (2020a), Pore-scale mechanisms of CO2 storage in oilfields, *Scientific Reports*, *10*(1), 1–9, doi:https://doi.org/10.1038/s41598-020-65416-z.

Alhosani, A., A. Scanziani, Q. Lin, S. Foroughi, A. M. Alhammadi, M. J. Blunt, and B. Bijeljic (2020b), Dynamics of water injection in an oil-wet reservoir rock at subsurface conditions: Invasion patterns and pore-filling events, *Physical Review E*, *102*(2), 23,110, doi:https://doi.org/10.1103/PhysRevE.102.023110.

AlRatrout, A., A. Q. Raeini, B. Bijeljic, and M. J. Blunt (2017), Automatic measurement of contact angle in pore-space images, *Advances in Water Resources*, *109*, 158–169, doi:https://doi.org/10.1016/j.advwatres.2017.07.018.

Alyafei, N., and M. J. Blunt (2016), The effect of wettability on capillary trapping in carbonates, *Advances in Water Resources*, *90*, 36–50, doi:https://doi.org/10.1016/j.advwatres.2016.02.001.

An, S., H. Yu, and J. Yao (2017), GPU-accelerated volumetric lattice Boltzmann method for porous media flow, *Journal of Petroleum Science and Engineering*, *156*(May), 546–552, doi:https://doi.org/10.1016/j.petrol.2017.06.031.

Andrew, M., B. Bijeljic, and M. J. Blunt (2014a), Pore-by-pore capillary pressure measurements using X-ray microtomography at reservoir conditions: Curvature, snap-off, and remobilization of residual CO 2, *Water Resources Research*, *50*(11), 8760–8774.

Andrew, M., B. Bijeljic, and M. J. Blunt (2014b), Pore-scale contact angle measurements at reservoir conditions using X-ray microtomography, *Advances in Water Resources*, *68*, 24–31, doi:https://doi.org/10.1016/j.advwatres.2014.02.014.

Andrew, M., H. Menke, M. J. Blunt, and B. Bijeljic (2015), The Imaging of Dynamic Multiphase Fluid Flow Using Synchrotron-Based X-ray Microtomography at Reservoir Conditions, *Transport in Porous Media*, *110*(1), 1–24, doi:https://doi.org/10.1007/s11242-015-0553-2.

Armstrong, R. T., J. E. McClure, V. Robins, Z. Liu, C. H. Arns, S. Schlüter, and S. Berg (2019), Porous media characterization using minkowski functionals: Theories, applications and future directions, *Transport in Porous Media*, *130*, 305–335.

Bakke, S., and P.-E. Øren (1997), 3-D pore-scale modelling of sandstones and flow simulations in the pore networks, *SPE Journal*, *2*(2), 136–149, doi:https://doi.org/10.2118/35479-PA.

Benziger, J., J. Nehlsen, D. Blackwell, T. Brennan, and J. Itescu (2005), Water flow in the gas diffusion layer of pem fuel cells, *Journal of Membrane Science*, *261*(1-2), 98–106.

Berg, S., H. Ott, S. A. Klapp, A. Schwing, R. Neiteler, N. Brussee, A. Makurat, L. Leu, F. Enzmann, J. O. Schwarz, M. Kersten, S. Irvine, and M. Stampanoni (2013), Real-time 3D imaging of Haines jumps in porous media flow, *Proceedings of the National Academy of Sciences of the United States of America*, *110*(10), 3755–3759, doi:https://doi.org/10.1073/pnas.1221373110.

Blunt, M., and P. King (1990), Macroscopic parameters from simulations of pore scale flow, *Physical Review A*, *42*(8), 4780.

Blunt, M. J. (1997), Pore level modeling of the effects of wettability, *SPE Journal*, *2*(4), 494–508, doi:https://doi.org/10.2118/38435-PA.

Blunt, M. J. (2017), *Multiphase Flow in Permeable Media: A Pore-Scale Perspective*, Cambridge University Press.

Blunt, M. J., B. Bijeljic, H. Dong, O. Gharbi, S. Iglauer, P. Mostaghimi, A. Paluszny, and C. Pentland (2013), Pore-scale imaging and modelling, *Advances in Water Resources*, doi:https://doi.org/10.1016/j.advwatres.2012.03.003.

Blunt, M. J., Q. Lin, T. Akai, and B. Bijeljic (2019), A thermodynamically consistent characterization of wettability in porous media using high-resolution imaging, *Journal of Colloid and Interface Science*, *552*, 59–65, doi:https://doi.org/10.1016/j.jcis.2019.05.026.

Boek, E. S., I. Zacharoudiou, F. Gray, S. M. Shah, J. P. Crawshaw, and J. Yang (2017), Multiphase-flow and reactive-transport validation studies at the pore scale by use of lattice Boltzmann computer simulations, *SPE journal*, *22*(03), 940–949.

Bondino, I., G. Hamon, W. Kallel, and D. Kac (2013), Relative Permeabilities From Simulation in 3D Rock Models and Equivalent Pore Networks: Critical Review and Way Forward, *Petrophysics*, *54*(06), 538–546.

Boot-Handford, M. E., J. C. Abanades, E. J. Anthony, M. J. Blunt, S. Brandani, N. Mac Dowell, J. R. Fernández, M. C. Ferrari, R. Gross, J. P. Hallett, R. S. Haszeldine, P. Heptonstall, A. Lyngfelt, Z. Makuch, E. Mangano, R. T. Porter, M. Pourkashanian, G. T. Rochelle, N. Shah, J. G. Yao, and P. S. Fennell (2014), Carbon capture and storage update, *Energy and Environmental Science*, *7*(1), 130–189, doi:https://doi.org/10.1039/C3EE42350F.

Brakke, K. A. (1992), The surface evolver, *Experimental mathematics*, *1*(2), 141–165.

Brakke, K. A. (1994), Surface evolver manual, *Mathematics Department, Susquehanna Univerisity, Selinsgrove, PA*, *17870*(2.24), 20.

Bryant, S., and M. Blunt (1992), Prediction of relative permeability in simple porous media, *Physical review A*, *46*(4), 2004.

Bryant, S. L., P. R. King, and D. W. Mellor (1993a), Network model evaluation of permeability and spatial correlation in a real random sphere packing, *Transport in porous media*, *11*(1), 53–70.

Bryant, S. L., D. W. Mellor, and C. A. Cade (1993b), Physically representative network models of transport in porous media, *AIChE Journal*, *39*(3), 387–396.

Bullard, J. W., and E. J. Garboczi (2009), Capillary rise between planar surfaces, *Physical Review E*, *79*(1), 011,604.

Chang, H.-M., C.-W. Lin, M.-H. Chang, H.-R. Shiu, W.-C. Chang, and F.-H. Tsau (2011), Optimization of polytetrafluoroethylene content in cathode gas diffusion layer by the evaluation of compression effect on the performance of a proton exchange membrane fuel cell, *Journal of Power Sources*, *196*(8), 3773–3780.

Chatzis, I., and F. A. L. Dullien (1977), Modelling pore structure by 2-d and 3-d networks with application to sandstones, *Journal of Canadian Petroleum Technology*, *16*, doi:https://doi.org/10.2118/77-01-09.

Crane, K., F. d. Goes, M. Desbrun, and P. Schröder (2013), Digital geometry processing with discrete exterior calculus, in *ACM SIGGRAPH 2013 courses*, SIGGRAPH '13, ACM, New York, NY, USA.

Datta, S. S., T. S. Ramakrishnan, and D. A. Weitz (2014), Mobilization of a trapped non-wetting fluid from a three-dimensional porous medium, *Physics of Fluids*, *26*(2), 22,002.

de Gennes, P.-G., F. Brochard-Wyart, D. Quéré, et al. (2004), *Capillarity and wetting phenomena: drops, bubbles, pearls, waves*, Springer.

Deng, W., M. B. Cardenas, and P. C. Bennett (2014), Extended Roof snap-off for a continuous nonwetting fluid and an example case for supercritical CO2, *Advances in Water Resources*, *64*, 34–46, doi:https://doi.org/10.1016/j.advwatres.2013.12.001.

Diaz, C. E., I. Chatzis, and F. A. Dullien (1987), Simulation of capillary pressure curves using bond correlated site percolation on a simple cubic network, *Transport in Porous Media*, *2*(3), 215–240, doi:https://doi.org/10.1007/BF00165783.

Dixit, A. B., S. R. McDougall, K. S. Sorbie, and J. Buckley (1999), Pore-scale modeling of wettability effects and their influence on oil recovery, *SPE Reservoir Evaluation & Engineering*, *2*(01), 25–36.

Dong, H., and M. J. Blunt (2009), Pore-network extraction from micro-computerized-tomography images, *Physical review E*, *80*(3), 36,307.

Dullien, F. A., C. Zarcone, I. F. Macdonald, A. Collins, and R. D. Bochard (1989), The effects of surface roughness on the capillary pressure curves and the heights of capillary rise in glass bead packs, *Journal of Colloid And Interface Science*, *127*(2), 362–372, doi:https://doi.org/10.1016/0021-9797(89)90042-8.

Fatt, I. (1956), The Network Model of Porous Media, *Trans AIME*, *207*(1), 144–181, doi:https://doi.org/10.2118/574-G.

Foroughi, S., B. Bijeljic, Q. Lin, A. Q. Raeini, and M. J. Blunt (2020), Pore-by-pore modeling, analysis, and prediction of two-phase flow in mixed-wet rocks, *Phys. Rev. E*, *102*(2), 23,302, doi:https://doi.org/10.1103/PhysRevE.102.023302.

Gao, Y., Q. Lin, B. Bijeljic, and M. J. Blunt (2017), X-ray Microtomography of Intermittency in Multiphase Flow at Steady State Using a Differential Imaging Method, *Water Resources Research*, *53*(12), 10,274–10,292, doi:https://doi.org/10.1002/2017WR021736.

Gao, Y., A. Q. Raeini, A. M. Selem, I. Bondino, M. J. Blunt, and B. Bijeljic (2020), Pore-scale imaging with measurement of relative permeability and capillary pressure on the same reservoir sandstone sample under water-wet and mixed-wet conditions, *Advances in Water Resources*, *146*, doi:https://doi.org/10.1016/j.advwatres.2020.103786.

Giudici, L. M., A. Qaseminejad Raeini, M. J. Blunt, and B. Bijeljic (2023a), Representation of fully three-dimensional interfacial curvature in pore-network models, *Water Resources Research*, *59*(4), e2022WR033,983.

Giudici, L. M., A. Q. Raeini, T. Akai, M. J. Blunt, and B. Bijeljic (2023b), Pore-scale modeling of two-phase flow: A comparison of the generalized network model to direct numerical simulation, *Physical Review E*, *107*(3), 035,107.

Gostick, J. T., M. A. Ioannidis, M. W. Fowler, and M. D. Pritzker (2009), Wettability and capillary behavior of fibrous gas diffusion media for polymer electrolyte membrane fuel cells, *Journal of Power Sources*, *194*(1), 433–444.

Haines, W. B. (1930), Studies in the physical properties of soil. v. the hysteresis effect in capillary properties, and the modes of moisture distribution associated therewith, *The Journal of Agricultural Science*, *20*(1), 97–116.

Hassanizadeh, S. M., and W. G. Gray (1993), Thermodynamic basis of capillary pressure in porous media, *Water Resources Research*, *29*(10), 3389–3405, doi:https://doi.org/10.1029/93WR01495.

Herring, A. L., A. Sheppard, L. Andersson, and D. Wildenschild (2016), Impact of wettability alteration on 3D nonwetting phase trapping and transport, *International Journal of Greenhouse Gas Control*, *46*, 175–186, doi:https://doi.org/10.1016/j.ijggc.2015.12.026.

Huang, H., P. Meakin, and M. Liu (2005), Computer simulation of two-phase immiscible fluid motion in unsaturated complex fractures using a volume of fluid method, *Water Resources Research*, *41*(12), doi:https://doi.org/10.1029/2005WR004204.

Inc., W. R. (), Mathematica, Version 13.3, champaign, IL, 2023.

Irannezhad, A., B. K. Primkulov, R. Juanes, and B. Zhao (2023), Fluid-fluid displacement in mixed-wet porous media, *Physical Review Fluids*, *8*(1), L012,301.

Jasak, H., A. Jemcov, Z. Tukovic, and others (2007), OpenFOAM: A C++ library for complex physics simulations, in *International workshop on coupled methods in numerical dynamics*, vol. 1000, pp. 1–20, IUC Dubrovnik Croatia.

Jerauld, G., and S. Salter (1990), The effect of pore-structure on hysteresis in relative permeability and capillary pressure: pore-level modeling, *Transport in porous media*, *5*, 103–151.

Jordan, L. R., A. Shukla, T. Behrsing, N. Avery, B. C. Muddle, and M. Forsyth (2000), Diffusion layer parameters influencing optimal fuel cell performance, *Journal of Power sources*, *86*(1-2), 250–254.

Keelan, D. K. (1972), A critical review of core analysis techniques, *Journal of Canadian Petroleum Technology*, *11*(02).

Kohanpur, A. H., M. Rahromostaqim, A. J. Valocchi, and M. Sahimi (2020), *Two-phase flow of CO2-brine in a heterogeneous sandstone: Characterization of the rock and comparison of the lattice-Boltzmann, pore-network, and direct numerical simulation methods*, vol. 135, doi:https://doi.org/10.1016/j.advwatres.2019.103469.

Koplik, J. (1982), Creeping flow in two-dimensional networks, *Journal of Fluid Mechanics*, *119*, 219–247, doi:https://doi.org/10.1017/S0022112082001323.

Kovscek, A. R., H. Wong, and C. J. Radke (1993), A pore-level scenario for the development of mixed wettability in oil reservoirs, *AIChE Journal*, *39*(6), 1072–1085, doi:https://doi.org/10.1002/aic.690390616.

Krevor, S., M. J. Blunt, S. M. Benson, C. H. Pentland, C. Reynolds, A. Al-Menhali, and B. Niu (2015), Capillary trapping for geologic carbon dioxide storage - From pore scale physics to field scale implications, *International Journal of Greenhouse Gas Control*, *40*, 221–237, doi:https://doi.org/10.1016/j.ijggc.2015.04.006.

Laplace, P. S. (1805), Traite de Mecanique Celeste (Gauther-Villars, Paris, 1839), suppl. au livre X, *Oeuvres compl*, *4*.

Leclaire, S., A. Parmigiani, O. Malaspinas, B. Chopard, and J. Latt (2017), Generalized three-dimensional lattice Boltzmann color-gradient method for immiscible two-phase pore-scale imbibition and drainage in porous media, *Physical Review E*, *95*(3), 33,306.

Lenormand, R., and S. Bories (1980), Description of a bond percolation mechanism used for the simulation of drainage with trapping in porous-media, *Comptes Rendus Hebdomadaires Des Seances De L Academie Des Sciences Serie B*, *291*(12), 279–282.

Lenormand, R., C. Zarcone, and A. Sarr (1983), Mechanisms of the displacement of one fluid by another in a network of capillary ducts, *Journal of Fluid Mechanics*, *135*, 337–353, doi:https://doi.org/10.1017/S0022112083003110.

Lenormand, R., E. Touboul, and C. Zarcone (1988), Numerical models and experiments on immiscible displacements in porous media, *Journal of fluid mechanics*, *189*, 165–187.

Lerdahl, T. R., P.-E. Oren, and S. Bakke (2000), A Predictive Network Model for Three-Phase Flow in Porous Media, *SPE 5931 - Proceedings of the SPEDOE Improved Oil Recovery Symposium, Tulsa, OK,*, *April*, 2–5, doi:https://doi.org/10.2118/59311-ms.

Li, K., and R. N. Horne (2008), Numerical simulation without using experimental data of relative permeability, *Journal of Petroleum Science and Engineering*, *61*(2-4), 67–74.

Lim, C., and C. Wang (2004), Effects of hydrophobic polymer content in gdl on power performance of a pem fuel cell, *Electrochimica Acta*, *49*(24), 4149–4156.

Lin, Q., B. Bijeljic, R. Pini, M. J. Blunt, and S. Krevor (2018), Imaging and Measurement of Pore-Scale Interfacial Curvature to Determine Capillary Pressure Simultaneously With Relative Permeability, *Water Resources Research*, *54*(9), 7046–7060, doi:https://doi.org/10.1029/2018WR023214.

Lin, Q., B. Bijeljic, S. Berg, R. Pini, M. J. Blunt, and S. Krevor (2019), Minimal surfaces in porous media: Pore-scale imaging of multiphase flow in an altered-wettability Bentheimer sandstone, *Physical Review E*, *99*(6), 1–13, doi:https://doi.org/10.1103/PhysRevE.99.063105.

Maes, J., and H. P. Menke (2021), GeoChemFoam: Direct Modelling of Multiphase Reactive Transport in Real Pore Geometries with Equilibrium Reactions, *Transport in Porous Media*, *139*(2), 271–299, doi:https://doi.org/10.1007/s11242-021-01661-8.

Mason, G., and N. R. Morrow (1991), Capillary behavior of a perfectly wetting liquid in irregular triangular tubes, *Journal of Colloid and Interface Science*, *141*(1), 262–274, doi:https://doi.org/10.1016/0021-9797(91)90321-X.

McClure, J. E., Z. Li, M. Berrill, and T. Ramstad (2021), The LBPM software package for simulating multiphase flow on digital images of porous rocks, *Computational Geosciences*, *25*(3), 871–895, doi:https://doi.org/10.1007/s10596-020-10028-9.

Mittal, R., R. Ni, and J. H. Seo (2020), The flow physics of COVID-19, *Journal of Fluid Mechanics*, *894*, 1–14, doi:https://doi.org/10.1017/jfm.2020.330.

Morrow, N. R. (1970a), Physics and thermodynamics of capillary action in porous media, *Industrial & Engineering Chemistry*, *62*(6), 32–56, doi:https://doi.org/10.1021/ie50726a006.

Morrow, N. R. (1970b), Irreducible wetting-phase saturations in porous media, *Chemical Engineering Science*, *25*(11), 1799–1815, doi:https://doi.org/10.1016/0009-2509(70)80070-7.

Morrow, N. R. (1975), Effects of Surface Roughness on Contact Angle With Special Reference To Petroleum Recovery., *Journal of Canadian Petroleum Technology*, *14*(4), 42–53, doi:https://doi.org/10.2118/75-04-04.

Mostaghimi, P., M. J. Blunt, and B. Bijeljic (2013), Computations of Absolute Permeability on Micro-CT Images, *Mathematical Geosciences*, *45*(1), 103–125, doi:https://doi.org/10.1007/s11004-012-9431-4.

Mukherjee, P. P., Q. Kang, and C. Y. Wang (2011), Pore-scale modeling of two-phase transport in polymer electrolyte fuel cells - Progress and perspective, *Energy and Environmental Science*, *4*(2), 346–369, doi:https://doi.org/10.1039/b926077c.

Muskat, M., and M. W. Meres (1936), The flow of heterogeneous fluids through porous media, *Physics*, *7*(9), 346–363.

Okonkwo, P. C., and C. Otor (2021), A review of gas diffusion layer properties and water management in proton exchange membrane fuel cell system, *International Journal of Energy Research*, *45*(3), 3780–3800, doi:https://doi.org/10.1002/er.6227.

Oren, P., J. Billiotte, and W. Pinczewski (1992), Mobilization of waterflood residual oil by gas injection for water-wet conditions, *SPE formation Evaluation*, *7*(01), 70–78.

Øren, P.-E., S. Bakke, and O. J. Arntzen (1998), Extending predictive capabilities to network models, *SPE Journal*, *3*(4), 324–336, doi:https://doi.org/10.2118/52052-PA.

Pan, C., M. Hilpert, and C. T. Miller (2004), Lattice-Boltzmann simulation of two-phase flow in porous media, *Water Resources Research*, *40*(1), W01,501, doi:https://doi.org/10.1029/2003WR002120.

Park, S., J.-W. Lee, and B. N. Popov (2008), Effect of ptfe content in microporous layer on water management in pem fuel cells, *Journal of Power Sources*, *177*(2), 457–463.

Pavuluri, S., J. Maes, J. Yang, M. Regaieg, A. Moncorgé, and F. Doster (2020), Towards pore network modelling of spontaneous imbibition: contact angle dependent invasion patterns and the occurrence of dynamic capillary barriers, *Computational Geosciences*, *24*, 951–969, doi:https://doi.org/10.1007/s10596-019-09842-7.

Pentland, C. H., Y. Tanino, S. Iglauer, and M. J. Blunt (2010), Capillary trapping in water-wet sandstones: Coreflooding experiments and pore-network modeling, *SPE 13379 - Proceedings of the SPE Annual Technical Conference and Exhibition*, *2*, 1245–1253, doi:https://doi.org/10.2118/133798-ms.

Pickell, J., B. Swanson, and W. Hickman (1966), Application of air-mercury and oil-air capillary pressure data in the study of pore structure and fluid distribution, *Society of Petroleum Engineers Journal*, *6*(01), 55–61.

Porter, M. L., M. G. Schaap, and D. Wildenschild (2009), Lattice-Boltzmann simulations of the capillary pressure–saturation–interfacial area relationship for porous media, *Advances in Water Resources*, *32*(11), 1632–1640.

Rabbani, H. S., B. Zhao, R. Juanes, and N. Shokri (2018), Pore geometry control of apparent wetting in porous media, *Scientific Reports*, *8*(1), 1–8, doi:https://doi.org/10.1038/s41598-018-34146-8.

Raeesi, B., N. R. Morrow, and G. Mason (2014), Capillary Pressure Hysteresis Behavior of Three Sandstones Measured with a Multistep Outflow-Inflow Apparatus, *Vadose Zone Journal*, *13*(3), vzj2013.06.0097, doi:https://doi.org/10.2136/vzj2013.06.0097.

Raeini, A. Q., M. J. Blunt, and B. Bijeljic (2012), Modelling two-phase flow in porous media at the pore scale using the volume-of-fluid method, *Journal of Computational Physics*, *231*(17), 5653–5668, doi:https://doi.org/10.1016/j.jcp.2012.04.011.

Raeini, A. Q., M. J. Blunt, and B. Bijeljic (2014), Direct simulations of two-phase flow on micro-CT images of porous media and upscaling of pore-scale forces, *Advances in Water Resources*, *74*, 116–126, doi:https://doi.org/10.1016/j.advwatres.2014.08.012.

Raeini, A. Q., B. Bijeljic, and M. J. Blunt (2015), Modelling capillary trapping using finite-volume simulation of two-phase flow directly on micro-CT images, *Advances in Water Resources*, *83*, 102–110, doi:https://doi.org/10.1016/j.advwatres.2015.05.008.

Raeini, A. Q., B. Bijeljic, and M. J. Blunt (2017), Generalized network modeling: Network extraction as a coarse-scale discretization of the void space of porous media, *Physical Review E*, *96*(1), 01,331, doi:https://doi.org/10.1103/PhysRevE.96.013312.

Raeini, A. Q., B. Bijeljic, and M. J. Blunt (2018), Generalized network modeling of capillary-dominated two-phase flow, *Physical Review E*, *97*(2), 023,308, doi:https://doi.org/10.1103/PhysRevE.97.023308.

Raeini, A. Q., J. Yang, I. Bondino, T. Bultreys, M. J. Blunt, and B. Bijeljic (2019), Validating the Generalized Pore Network Model Using Micro-CT Images of Two-Phase Flow, *Transport in Porous Media*, *130*(2), 405–424, doi:https://doi.org/10.1007/s11242-019-01317-8.

Ramstad, T., P. E. Øren, and S. Bakke (2010), Simulation of two-phase flow in Reservoir rocks using a lattice Boltzmann method, *SPE Journal*, *15*(4), 923–933, doi:https://doi.org/10.2118/124617-pa.

Regaieg, M., F. Nono, T. F. Faisal, and R. Rivenq (2023), Large-pore network simulations coupled with innovative wettability anchoring experiment to predict relative permeability of a mixed-wet rock, *Transport in Porous Media*, *147*(2), 495–517.

Roof, J. (1970), Snap-off of Oil Droplets in Water-Wet Pores, *Society of Petroleum Engineers Journal*, *10*(01), 85–90.

Rücker, M., W. B. Bartels, T. Bultreys, M. Boone, K. Singh, G. Garfi, A. Scanziani, C. Spurin, S. Yesufu-Rufai, S. Krevor, M. J. Blunt, O. Wilson, H. Mahani, V. Cnudde, P. F. Luckham, A. Georgiadis, and S. Berg (2020), Workflow for upscaling wettability from the nanoscale to core scale, *Petrophysics*, *61*(2), 189–205, doi:https://doi.org/10.30632/pjv61n2-2020a5.

Ruspini, L. C., R. Farokhpoor, and P. E. Øren (2017), Pore-scale modeling of capillary trapping in water-wet porous media: A new cooperative pore-body filling model, *Advances in Water Resources*, *108*, 1–14, doi:https://doi.org/10.1016/j.advwatres.2017.07.008.

Salathiel, R. A. (1973), Oil recovery by surface film drainage in mixed-wettability rocks, *Journal of Petroleum Technology*, *25*(10), 1–216.

Scanziani, A., K. Singh, T. Bultreys, B. Bijeljic, and M. J. Blunt (2018), In situ characterization of immiscible three-phase flow at the pore scale for a water-wet carbonate rock, *Advances in Water Resources*, *121*(June), 446–455, doi:https://doi.org/10.1016/j.advwatres.2018.09.010.

Scanziani, A., Q. Lin, A. Alhosani, M. J. Blunt, and B. Bijeljic (2020), Dynamics of fluid displacement in mixed-wet porous media, *Proceedings of the Royal Society A*, *476*(2240), 20200,040, doi:https://doi.org/10.1098/rspa.2020.0040.

Shams, M., A. Q. Raeini, M. J. Blunt, and B. Bijeljic (2018), A study to investigate viscous coupling effects on the hydraulic conductance of fluid layers in two-phase flow at the pore level, *Journal of Colloid and Interface Science*, *522*, 299–310, doi:https://doi.org/10.1016/j.jcis.2018.03.028.

Sheppard, A., R. Sok, and H. Averdunk (2005), Improved pore network extraction methods, in *International Symposium of the Society of Core Analysts*, vol. 2125, pp. 1–11.

Shojaei, M. J., B. Bijeljic, Y. Zhang, and M. J. Blunt (2022), Minimal Surfaces in Porous Materials: X-Ray Image-Based Measurement of the Contact Angle and Curvature in Gas Diffusion Layers to Design Optimal Performance of Fuel Cells, *ACS Applied Energy Materials*, *5*(4), 4613–4621, doi:https://doi.org/10.1021/acsaem.2c00023.

Singh, K., B. Bijeljic, and M. J. Blunt (2016), Imaging of oil layers, curvature and contact angle in a mixed-wet and a water-wet carbonate rock, *Water Resources Research*, *52*(3), 1716–1728, doi:https://doi.org/10.1002/2015WR018072.

Singh, K., H. Menke, M. Andrew, Q. Lin, C. Rau, M. J. Blunt, and B. Bijeljic (2017), Dynamics of snap-off and pore-filling events during two-phase fluid flow in permeable media, *Scientific Reports*, *7*(1), 1–13, doi:https://doi.org/10.1038/s41598-017-05204-4.

Sun, C., J. E. McClure, P. Mostaghimi, A. L. Herring, M. Shabaninejad, S. Berg, and R. T. Armstrong (2020), Linking continuum-scale state of wetting to pore-scale contact angles in porous media, *Journal of Colloid and Interface Science*, *561*, 173–180, doi:https://doi.org/10.1016/j.jcis.2019.11.105.

Tanino, Y., and M. Blunt (2013), Laboratory investigation of capillary trapping under mixed-wet conditions, *Water Resources Research*, *49*(7), 4311–4319.

Tartakovsky, A. M., and P. Meakin (2006), Pore scale modeling of immiscible and miscible fluid flows using smoothed particle hydrodynamics, *Advances in Water Resources*, *29*(10), 1464–1478.

Valvatne, P. H., and M. J. Blunt (2004), Predictive pore-scale modeling of two-phase flow in mixed wet media, *Water Resources Research*, *40*(7), W07,406, doi:https://doi.org/10.1029/2003WR002627.

Vijay, R., S. Seshadri, and P. Haridoss (2011), Gas diffusion layer with ptfe gradients for effective water management in pem fuel cells, *Transactions of the Indian Institute of Metals*, *64*, 175–179.

Wildenschild, D., and A. P. Sheppard (2013), X-ray imaging and analysis techniques for quantifying pore-scale structure and processes in subsurface porous medium systems, *Advances in Water Resources*, *51*, 217–246, doi:https://doi.org/10.1016/j.advwatres.2012.07.018.

Wilkinson, D., and J. F. Willemsen (1983), Invasion percolation: a new form of percolation theory, *Journal of Physics A: Mathematical and General*, *16*(14), 3365.

Young, T. (1805), III. An essay on the cohesion of fluids, *Philosophical transactions of the royal society of London*, (95), 65–87, doi:https://doi.org/10.1098/rstl.1805.0005.

Zhang, G., Z. Bao, B. Xie, Y. Wang, and K. Jiao (2021), Three-dimensional multi-phase simulation of PEM fuel cell considering the full morphology of metal foam flow field, *International Journal of Hydrogen Energy*, *46*(3), 2978–2989, doi:https://doi.org/10.1016/j.ijhydene.2020.05.263.

Zhang, G., S. Foroughi, A. Q. Raeini, M. J. Blunt, and B. Bijeljic (2023), The impact of bimodal pore size distribution and wettability on relative permeability and capillary pressure in a microporous limestone with uncertainty quantification, *Advances in Water Resources*, *171*, 104,352, doi:https://doi.org/10.1016/j.advwatres.2022.104352.

Zhao, B., C. W. MacMinn, and R. Juanes (2016), Wettability control on multiphase flow in patterned microfluidics, *Proceedings of the National Academy of Sciences*, *113*(37), 10,251–10,256.

Zhao, B., C. W. MacMinn, B. K. Primkulov, Y. Chen, A. J. Valocchi, J. Zhao, Q. Kang, K. Bruning, J. E. McClure, C. T. Miller, A. Fakhari, D. Bolster, T. Hiller, M. Brinkmann, L. Cueto-Felgueroso, D. A. Cogswell, R. Verma, M. Prodanović, J. Maes, S. Geiger, M. Vassvik, A. Hansen, E. Segre, R. Holtzman, Z. Yang, C. Yuan, B. Chareyre, and R. Juanes (2019), Comprehensive comparison of pore-scale models for multiphase flow in porous media, *Proceedings of the National Academy of Sciences of the United States of America*, *116*(28), 13,799–13,806, doi:https://doi.org/10.1073/pnas.1901619116.

Zhao, J., F. Qin, D. Derome, and J. Carmeliet (2020), Simulation of quasi-static drainage displacement in porous media on pore-scale: Coupling lattice Boltzmann method and pore network model, *Journal of Hydrology*, *588*(May), 125,080, doi:https://doi.org/10.1016/j.jhydrol.2020.125080.

CHAPTER A

OPTIMISATION OF COEFFICIENTS

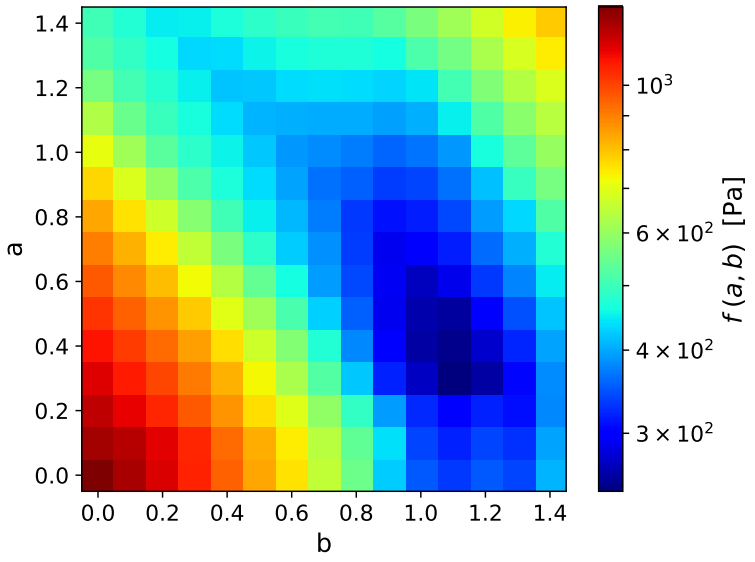

Figure A.1: Optimisations performed on the pore-space expansion coefficients a and b present in Eq. 3.2. The mean absolute difference in threshold capillary pressure, $f(a,b)$, between the volume-of-fluid predictions displayed in Fig. 3.5 and the GNM predictions is determined using Eq. A.1. The combination a=0.3 and b=1.1 corresponds to the global minimum of $f(a,b)$, and these coefficients are maintained for all of the GNM predictions in this work.

Equation 3.2 is used to determine the pore-space expansion at every pore centre, throat centre and half-way point in the network. However, network models are simplified representations of the real pore space: only a coarse resolution is provided by the network extraction process. Physically based approximations of finer details require calibration to mitigate error introduced by spatial simplifications. To optimise the coefficients a and b in Eq. 3.2, the minimum mean absolute difference (Fig. A.1) between the volume-of-fluid predictions displayed in Fig. 3.5 and the GNM predictions for 225 combinations of a and b is determined using:

$$f(a,b) = \frac{1}{N}\sum_{\theta \in S} \left| {}^{VoF}P_c^{\theta} - {}^{GNM}P_c^{\theta}(a,b) \right|, \tag{A.1}$$

where N is the number of contact angles for which predictions exist, ${}^{VoF}P_c^{\theta}$ is the volume-

of-fluid threshold capillary pressure prediction at contact angle θ and ${}^{GNM}P_c^{\theta}$ is the GNM threshold capillary pressure prediction at contact angle θ. The summation is over the set, S, of all simulated contact angles. In this work, $N = 9$ and S spans from $\theta = 30°$ to $\theta = 150°$ in $15°$ increments. Similar to the treatment of pore-space expansion, the methods to determine

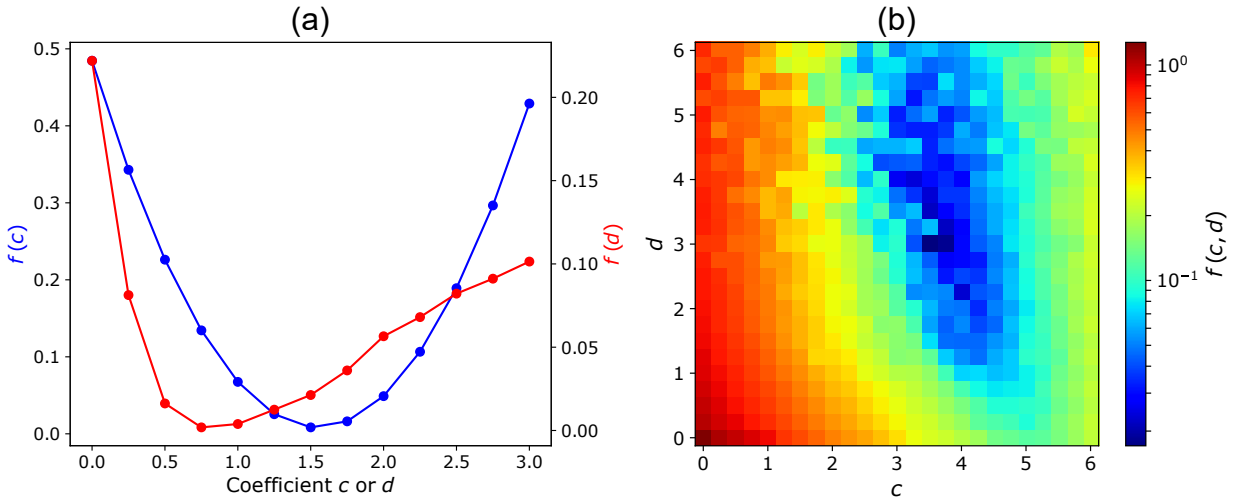

Figure A.2: Optimisations performed on the throat sagittal curvature coefficient c and the pore sagittal curvature coefficient d present in Eq. 3.4 and 3.5, respectively. In (a), the geometry-based throat and pore sagittal curvature are independent of each other and can be optimised by minimising Eq. A.2 and A.3 separately. In (b), the iterative approach to modelling sagittal curvature results in throat and pore sagittal curvature affecting each other, and the collective objective function in Eq. A.4 is minimised.

sagittal curvature presented in this paper use discrete points defined at the pores and throats. In reality, curvature is mathematically defined at an infinitesimal portion of a surface, and so an estimation using discrete points requires calibration. For the geometry-based method in Fig. 3.2 of Section 3.2.2, the coefficients of throat sagittal curvature (c) and pore sagittal curvature (d) are obtained by minimising the objective functions:

$$f(c) = \left(1 - \frac{{}^{10}\kappa^{An} + c\,{}^{10}\kappa_{st}}{{}^{10}\kappa^{VoF}}\right)^2 + \left(1 - \frac{{}^{20}\kappa^{An} + c\,{}^{20}\kappa_{st}}{{}^{20}\kappa^{VoF}}\right)^2, \tag{A.2}$$

$$f(d) = \left(1 - \frac{{}^{10}S_w(d)}{{}^{10}S_w^{VoF}}\right)^2 + \left(1 - \frac{{}^{20}S_w(d)}{{}^{20}S_w^{VoF}}\right)^2, \tag{A.3}$$

where κ^{An} and κ^{VoF} represent two-dimensional analytic solutions and volume-of-fluid predictions of the total curvature at snap-off, respectively, κ_{st} is the throat sagittal curvature obtained from the geometry-based approximation presented in Eq. 3.4, and S_w and S_w^{VoF}

denote the throat saturation at snap-off predicted by the GNM and volume-of-fluid method, respectively. In both Eq. A.2 and Eq. A.3, the prescripts represent the $10°$ or $20°$ geometries in Fig. 3.4. Equations A.2 and A.3 can be optimised independently as pore sagittal curvature does not affect snap-off curvature at the throat with the geometry-based method, and Eq. A.2 can be solved analytically. The optimisation of c and d is shown in Fig. A.2a, giving $c = 1.5$ and $d = 0.75$. These coefficients are used to produce the macroscopic results in Figs. 3.11c and d.

A consequence of the iterative method to determine sagittal curvature (Fig. 3.10) is that the pores and throats are no longer independent. Therefore, the following objective function is minimised to find the optimal values of the coefficients c and d:

$$f(c,d) = \left(1 - \frac{^{10}\kappa(c,d)}{^{10}\kappa^{VoF}}\right)^2 + \left(1 - \frac{^{20}\kappa(c,d)}{^{20}\kappa^{VoF}}\right)^2 + \left(1 - \frac{^{10}S_w(c,d)}{^{10}S_w^{VoF}}\right)^2 + \left(1 - \frac{^{20}S_w(c,d)}{^{20}S_w^{VoF}}\right)^2, \tag{A.4}$$

where κ represents the total curvature at snap-off predicted by the GNM, and the remaining terms retain their definitions from Eq. A.2 and A.2. Figure A.2b shows 625 simulations used to find the global minimum of the objective function in Eq. A.4, which corresponds to $c = 3.5$ and $d = 3$. These coefficients — which are obtained through calibration against high resolution direct simulations — are used to produce the macroscopic results in Figs. 3.11e and f.

CHAPTER B

EXPANSION ANGLE SENSITIVITY

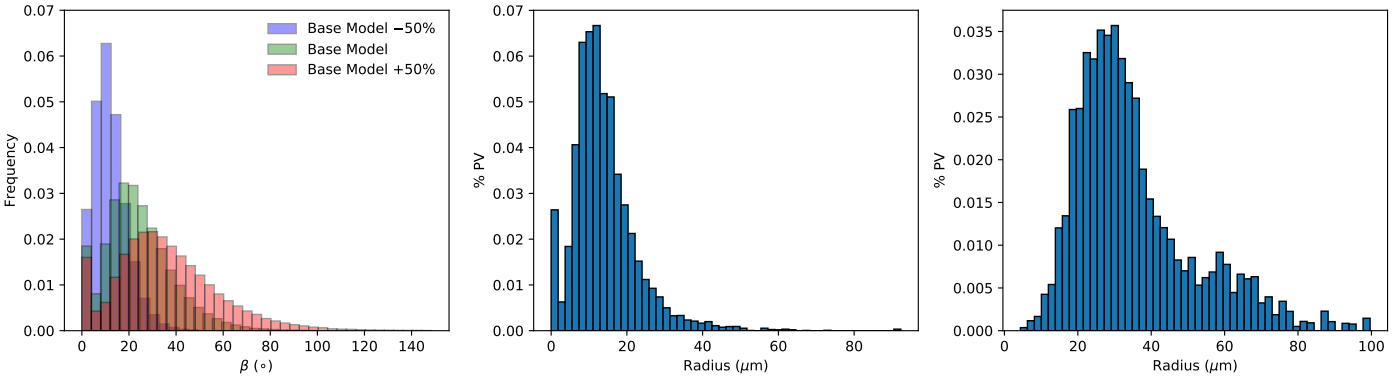

Figure B.1: The distributions of expansion angle (left), throat radius (centre) and pore radius (right) extracted from a 1000^3 voxel image of a Bentheimer sandstone. In the left plot, the different coloured histograms of expansion angle represent the base model (green) with 50% uncertainty added (red) or subtracted (blue), where the base model is obtained directly from Eq. 3.2.

Chapter 3 demonstrates the importance of the expansion angle, β, for accurate predictions of macroscopic capillary pressure. In this thesis, β is empirically estimated in Eq. 3.2 from the extracted network, while in the future, it is likely that the angle will be determined directly from an underlying image. In both instances, the extraction process will result in uncertainty in β.

The generalized network model was specifically created to minimise uncertainty in the extraction process. The geometry of the elements closely resembles the underlying pore geometry, and the network elements are formed from the pore-space corners of the voxel image itself. Therefore, it is reasonable to assume that uncertainty in β due to the GNM is small. However, the voxel images provided to the extraction algorithm must first undergo segmentation between void-space and solid voxels. The segmentation process can introduce significant uncertainty into network modelling, as it profoundly affects the geometry of the pore space.

Directly assessing the impact that segmentation-induced uncertainty in β has on predictions

is relatively challenging. Any change in segmentation will also affect pore and throat areas, which will overshadow the impact of β. However, it is possible to assume an uncertainty in β and apply it to a single image. This approach enables a direct assessment of the impact of uncertainty in β on predictions.

Figure B.2 shows macroscopic predictions with a presumed 50% uncertainty in β. Three generalized network flow simulations were performed on the same 1000^3 voxel image of Bentheimer sandstone analysed in Chapter 3. In each simulation, the corner-by-corner β values were either: maintained; increased by 50%; or decreased by 50% relative to the output of Eq. 3.2. This replicates the impact that segmentation, or extraction-induced, uncertainty in β would have on predictions. the distributions of β in each simulation, along with the distributions of pore and throat radii, are shown in Fig. B.1.

The sensitivity analysis in Fig. B.2 demonstrates that uncertainty in β can result in a 20% variation in macroscopic predictions of capillary pressure and relative permeability.

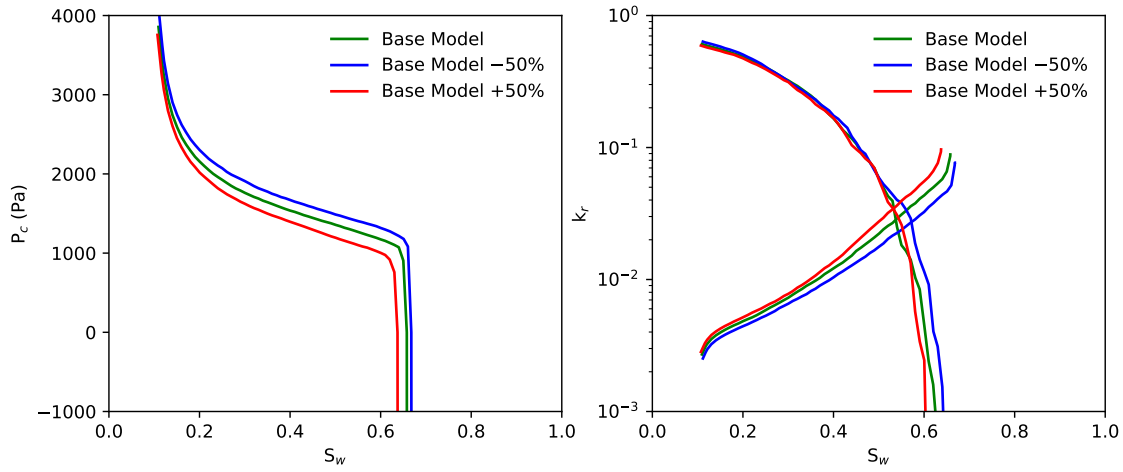

Figure B.2: A sensitivity analysis into the impact of uncertainty in β estimations on capillary pressure (left) and relative permeability (right). Three generalized network flow simulations were performed on the same 1000^3 voxel image of Bentheimer sandstone analysed in Chapter 3. In each simulation, the corner-by-corner β values were either: maintained (green); increased by 50% (red); or decreased by 50% (blue) relative to the output of Eq. 3.2.

CHAPTER C

SURFACE EVOLVER ENERGY INTEGRANDS

This appendix contains the derivations for all energy integrands used in Chapter 5. In all cases, the goal is to find a vector field which describes the contact loop. From Stoke's Theorem, a line integral of this vector field gives the surface area of the part of the solid which is coated with the invading phase.

C.1 Two-Dimensional geometries

C.1.1 Parallel plates

In parallel plates, the integral is clear: the area of a rectangle is its base multiplied by its height. The height of the contact line is given by the z coordinate, while the vector field describing the contact line on each plate is simply the unit vector in the x direction $\mathbf{F} = (1, 0, 0) \cdot z$.

C.1.2 Inclined Plates

The coated area of inclined plates is found in a similar fashion to parallel plates, however here the length of the coated area under the contact line is a function of the meniscus height z and the expansion angle β, $\mathbf{F} = (1, 0, 0) \cdot \frac{z}{\cos(\beta)}$.

C.1.3 Circular Plates

The coated area of a circular plate is found by determining the arc length of the coated region and multiplying by an infinitesimal portion of the contact line. The vector field describing the contact line remains unchanged from the previous examples, however the arc length requires an integral up to the height of the contact line.

The length of an infinitesimal portion of an arc is given by:

$$\begin{aligned} ds^2 &= dy^2 + dz^2 \\ ds &= \sqrt{1 + \left(\frac{dy}{dz}\right)^2}\, dz, \end{aligned} \tag{C.1}$$

and the equation describing the circular plates is:

$$y^2 + (z - r_{plates})^2 = r_{plates}^2. \tag{C.2}$$

Thus, the contact length to a height z on the plates is given by the integral:

$$g(z) = \int_0^z \sqrt{1 + \left(\frac{dy}{dz}\right)^2}\, dz = r_{plates}\left[\sin^{-1}\left(\frac{z - r_{plates}}{r_{plates}}\right) + \frac{\pi}{2}\right]. \tag{C.3}$$

Together with the vector field describing the contact line, this gives $\mathbf{F} = (1, 0, 0) \cdot g(z)$

C.2 Quasi Two-Dimensional Geometry: Micro-model

In the micromodel, the integral on the circular posts remains unchanged from the two-dimensional circular plates described previously. On the upper and lower flat plates, the vector field describing the contact line is given by the unit vector in the y direction, which can be multiplied by the meniscus height, z, to give the contact area in identical fashion to the parallel plates geometry.

However, for the portion of the contact loop residing on the upper and lower plates, an area correction must be added to account for the contact area above and below the circular posts. The correction, δA, is given by:

$$\delta A = \begin{cases} \int_0^{y_1} r_{plates} - \sqrt{r_{plates} - y^2}\, dy & z \le r_{plates} \\ \int_0^{y_1} r_{plates} - \sqrt{r_{plates} - y^2}\, dy - \frac{r_{plates}}{2}\left[\zeta - \sin(\zeta)\right] & z > r_{plates}, \end{cases} \tag{C.4}$$

where $\zeta = \cos^{-1}\left(\frac{2y_1^2}{r_{plates}^2} - 1\right)$.

C.3 Three Dimensional Sinusoid

The sinusoid poses the most complex vector field[1]. In the axial plane, the geometry is circular. Thus, the contact loop is defined by a circular unit-vector field $\mathbf{F} = \frac{1}{R^2}(-y, x, 0)$, where $R(z)$ is defined by Eq. 5.14. An infinitesimal strip of fluid-covered surface area is given integrating over the vector field $\mathbf{F}$ and multiplying by the length, $l(z)$, of the solid wall beneath the meniscus.

The function $l(z)$ can be found from standard calculus. The surface of revolution up to a height z is given by,

$$g(z) = \int_0^z 2\pi R\sqrt{1 + (R')^2}dz. \tag{C.5}$$

Substituting in the expression for $R(z)$ given by Eq. 5.14 and simplifying, one obtains,

$$g(z) = \int_0^z 2\pi \left(A\cos(qz) + b\right)\sqrt{1 + A^2q^2sin^2(qz)}dz, \tag{C.6}$$

where $q = \frac{2\pi}{\lambda}$, $A = \frac{R_p - R_t}{2}$ and $b = \frac{R_p + R_t}{2}$.

Using Mathematica (*Inc.*), the following analytical expression for the surface area can be obtained:

$$g(z) = \frac{1}{2q^2}\left(\sinh^{-1}\left(Aq\sin(qz)\right) + Aq\sin(qz)\sqrt{1 + A^2q^2\sin^2(qz)}\right) + \frac{b}{q}E\left(qz, -A^2q^2\right), \tag{C.7}$$

where $E(\cdot,\cdot)$ is an elliptic integral of the second kind.

Finally, the length $l(z)$ can be expressed as $l(z) = \frac{1}{2\pi}g(z)$, giving the final energy integrand presented in Eq. 5.18. The function g(z) can be evaluated separately for each wavelength region and summed to provide the total fluid-coated length beneath any point on the meniscus

[1]Prof. Kenneth Brakke is thanked for providing insightful guidance.

CHAPTER D

EMPIRICAL EQUATION OPTIMISATION

The sensitivity studies performed to obtain the form of Eqs. 5.21 and 5.22 are displayed in Figures D.1 and D.2, respectively.

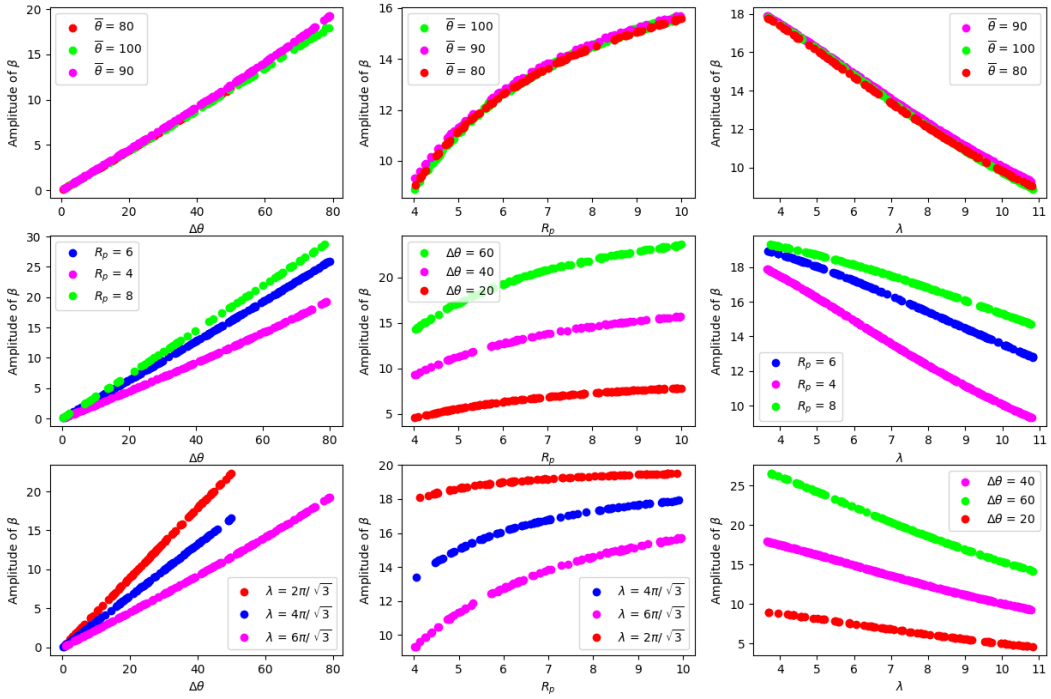

Figure D.1: The sensitivity analysis performed to determine the form of the equation describing the amplitude, A, in Eq. 5.20. In each plot, the amplitude is plotted against the difference in assigned contact angle ($\Delta\theta$), the pore radius R_p or the wavelength (λ). The different colours represent constant values of the given properties in each legend, where $\bar{\theta}$ is the average contact angle.

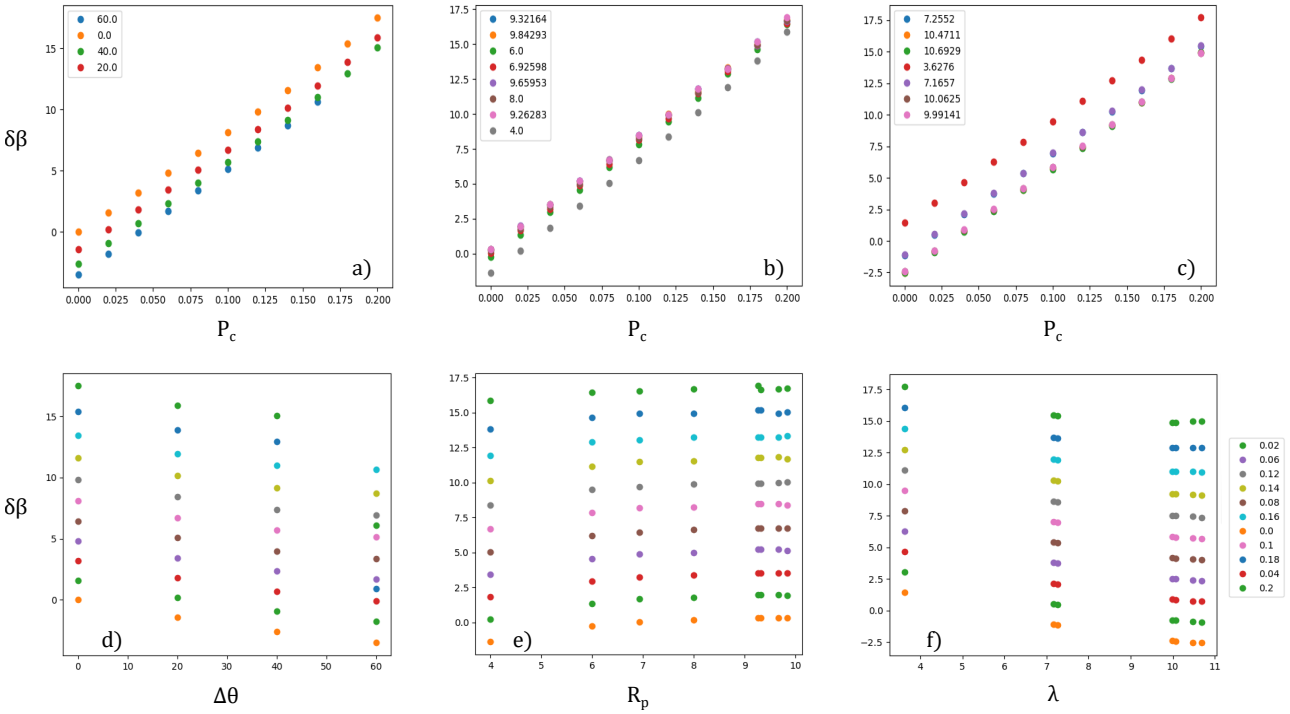

Figure D.2: A figure showing the sensitivity analysis performed to determine the form of $\delta\beta$ in Eq. 5.20. In (a)-(c), the different colours represent constant values of contact angle difference ($\Delta\theta$), pore radius (R_p) and wavelength (λ), respectively. In (d)-(f), the colours represent constant values of capillary pressure.

In Tables D.1 and D.2 below, the optimised coefficients for e and m in Eqs. 5.21 and 5.22, respectively, are displayed.

Table D.1: A table to show the optimised coefficients for e in Eq. 5.21. Their units are displayed within the square brackets.

Coefficient	1 [-]	2 [m^{-1}]	3 [-]	4 [m^{-1}]	5 [-]
e	1.025	4.169×10^{-3}	1.304	7.238×10^{-4}	0.260

Table D.2: A table to show the optimised coefficients for m in Eq. 5.22. Their units are displayed within the square brackets.

Coefficient	1 [m]	2 [m^{-1}]	3 [m^{-1}]	4 [-]
m	6.029×10^{-4}	-3.374×10^{-4}	-2.682×10^{-4}	-1.276×10^{-2}